Bacterial Adhesion and Motility on Silanized Glass Surfaces

A Dissertation

Presented to

the Faculty of the Department of Chemical and Biomolecular Engineering

University of Houston

In Partial Fulfillment

of the Requirements for the Degree

Doctor of Philosophy

in Chemical Engineering

by

Sumedha Sharma

August 2016

Bacterial Adhesion and Motility on Silanized Glass Surfaces

Sumedha Sharma

Approved:

Chair of the Committee
Jacinta C. Conrad, Associate Professor,
Chemical and Biomolecular Engineering

Committee Members:

Richard C. Willson, Professor,
Chemical and Biomolecular Engineering

Megan L. Robertson, Assistant Professor,
Chemical and Biomolecular Engineering

Ashutosh Agrawal, Assistant Professor,
Department of Mechanical Engineering

Yandi Hu, Assistant Professor,
Civil and Environmental Engineering

Dinesh K. Arora, Tech Innovation Lead,
Celanese Corporation

Suresh K. Khator, Associate Dean,
Cullen College of Engineering

Michael P. Harold, Professor and Chair,
Chemical and Biomolecular Engineering

Acknowledgments

I would like to gratefully acknowledge the guidance and support provided by my professor, Dr. Jacinta C. Conrad, during the course of this study. She has immensely contributed to my growth as a researcher and has influenced me strongly me as a professional. She has provided me very helpful guidance in developing both technical writing and presentation skills. I would also like to thank the members of my graduate committee, Dr. Richard Willson and Dr. Megan Robertson, for their suggestions and valuable insights during the various stages of my research. I want to thank Dr. Yandi Hu, Dr. Ashutosh Agrawal, and Dr. Dinesh Arora, for agreeing to be part of my dissertation committee. Technical discussions and valuable suggestions from my collaborator, Dr. Andrea Yuly Jaimes-Lizcano, and my colleagues, Ryan Poling Skutvik and Dr. Jack Jacob, are truly appreciated.

I would like to thank Dr. Richard Willson for access to bacteria culture facilities and Dr. Uli Strych for training. I would also like to thank Dr. Patrick C. Cirino, Chris Frei and Ryan B. McLay for bacteria strains, Dr. Gila Stein, for access to gonimetry and ellipsometry, Dr. Peter Vekilov, for access to atomic force microscopy, Dr. Megan Robertson, for access to DHR rheometer, Dr. Navin Vardarajan, for access to plasma cleaner, Dr. Boris Makarenko, for X-ray spectroscopy, and Dr. Michael Wong (Rice University), for zeta potential measurements. The generous help of Dr. Wendy Thomas and Dr. Evgeni Sokurenko (University of Washington) by providing the PAb49 antibody is gratefully acknowledged. I also want to acknowledge the help of all the members of my research group who have, in various ways, contributed to my research with their support and cooperation.

Finally, I want to thank my grandfather and my parents for instilling in me an early love for learning without which I would not have been able to pursue research. This work would not have been possible without the constant support I received from my family. I want to express my sincere gratitude to the love and support of my parents, Mrs. Satya and Mr. Vinod Bhatra, my in-laws, Mrs. Shakuntala and Mr. Rajendra P. Sharma and my extended family. I wish to thank my brother for always believing in me and supporting me in my decisions. A special acknowledgement to the constant love, support, and mentoring by my husband, Dr. Rahul Maharsia, without which neither the end goal nor this journey would have been possible. I want to especially thank my dear daughter, Khyaati, whose smile has been my refuge as well as my true inspiration during the most stressful of times and my newborn Lakshya for everything.

Bacterial Adhesion and Motility on Silanized Glass Surfaces

An Abstract

of a

Dissertation

Presented to

the Faculty of the Department of Chemical and Biomolecular Engineering

University of Houston

In Partial Fulfillment

of the Requirements for the Degree

Doctor of Philosophy

in Chemical Engineering

by

Sumedha Sharma

August 2016

Abstract

Attachment of bacteria to surfaces is the first step in the formation of biofilms. Medical, industrial, and technological applications require effective control over biofilm formation, and control of initial bacterial attachment is a potential alternate approach to conventional techniques to promote or suppress biofilm formation. Conventional use of antibiotics and bactericidal agents as antifouling techniques has adverse environmental implications[1] and potentially lead to evolution of antibiotic resistant strains of bacteria.[2] Controlling the initial attachment step in biofilm formation circumvents these disadvantages associated with conventional approaches. Rational design of surfaces to control bacterial attachment, however, requires fundamental understanding of bacteria-surface interactions and adhesion mechanisms. In this work, we investigate the adhesion of bacteria on surfaces of controlled physical properties to obtain a mechanistic understanding of adhesion and near surface mobility of bacteria.

First, we study the deposition behavior of *Escherichia coli* from flow on surfaces of controlled charge, wettability, and energy created by self-assembly of organosilanes on glass. We use high throughput bacteria tracking algorithms to analyze the trajectories for hundreds of bacteria. We characterize surface-associated motion of attached cells and find that a motility metric based on extent of motion mediated by flagella is inversely correlated with rate of bacterial deposition, whereas conventional surface characterization metrics are not well correlated. The transition from transient initial attachment to irreversible attachment is also correlated to deposition rate. Our results suggest that the techniques and methods presented here to characterize transient surface motility can

potentially serve as a metric to rapidly determine the efficacy of surfaces to reduce fouling by bacteria.

Next, we characterize the near-surface mobility associated with adhesion in *E. coli* bacteria deposited from flow at varying shear stresses on glass substrates bearing self-assembled alkylsilane and fluoroalkylsilane layers. We find that deposition of bacteria decreases with shear stress and increases with surface roughness. Bacteria also exhibit mobile adhesion on very smooth surfaces resulting in large linear displacements in the direction of flow which is independent of flagellar expression but requires absence of fimbriae on the cell surface. Speed of mobile adhesion decreases and residence time of cells increases as a function of increasing shear stress. Since surface roughness determines the transition from immobile to mobile adhesion, we suggest that strategies to reduce frictional interactions between cells and surfaces, either by engineering nanoscale-smooth surfaces or by suppressing expression of cell surface adhesins such as fimbriae, may help to reduce fouling during initial deposition.

Finally, we investigate the competing effects of surface chemistry, solution ionic strength, and medium viscoelasticity on near-surface attachment and motion of *E. coli*. We vary solution viscoelasticity by adding xanthan gum, a model polysaccharide; solution chemistry by adding a monovalent salt NaCl; and surface chemistry by using a hydrophobic silanized glass and hydrophilic cleaned glass. We sort cells between two types of near-surface behavior: surface-associated non-swimming and near-surface swimming. We characterize the dynamics of each population of cells and find that the swimming cells show near ballistic motion; and the non-swimming cells show near diffusive behavior on short time scales and sub-diffusive behavior on long times. Of the

three variables in the experiment (ionic strength, surface chemistry, and polymer concentration) the last has the most pronounced effect on dynamics and average speed of swimming cells. We show that high polymer concentrations in semi-dilute entangled regime present obstacles to bacteria locomotion and cells exhibit reversals in swimming trajectories without angular reorientation of the cell body axis. Our results suggest that characterizing the rheological properties of ambient environment is important for effective design of surfaces for applications such as medical implants and sensors in oil exploration where bacterial attachment occurs under moderate to highly viscous and Newtonian to highly non-Newtonian environments.

Table of Contents

List of Figures

List of Tables

Chapter 1 Introduction and Background

1.1 Overview

Bacteria are ubiquitous unicellular micro-organisms. They have a simple cell structure enclosed within a cell membrane that contains all genetic information within a single loop of DNA. Although bacteria can thrive in a variety of environments, almost 90% of bacteria in nature are found in sessile surface-associated communities called biofilms.[3] Biofilms are complex well-organized dynamic structures that comprise living and actively multiplying bacteria enclosed within a protective polymer matrix, which imparts resistance to host and environmental stresses.[4] Biofilm formation is responsible for 80% of nosocomial infections and results in 99,000 annual deaths in the United States alone. Beyond loss of human life and health, the annual capital cost of biofilm related in infections is estimated to be $120 billion.[5] In addition, water- and other fluid-based industrial processes such as food processing,[6] water treatment,[7] oil recovery,[8] heat exchange,[9] and marine transport[10] are examples of industrial applications that suffer from severe capital and operational losses due to bacteria-mediated biocorrosion and biofouling. About 34% of corrosion damage in oil recovery, amounting to $1.37 million of annual corrosion related costs, is attributed to bacterial adhesion to surfaces. Finally, in marine transport, severe capital damages due to biofouling are exacerbated by operational fuel cost due to increased drag from biofouling on ship hulls.[10] Conversely, several applications in bioremediation,[11, 12, 13] biodegradation[14] and other such beneficial biological processes may also require promoting growth of biofilms. Thus, myriad applications demand research efforts focused on designing strategies to controllably

prevent or promote the formation of biofilms. This end goal, in turn, requires understanding the mechanisms by which biofilms form on surfaces.

1.2 How biofilms form

The first step in the formation of biofilms is initial attachment of freely swimming planktonic bacteria to a surface (Figure 1.1). This initial step is followed by growth and multiplication of bacteria and secretion of exopolysaccharides that form the biofilm matrix, resulting in maturation and subsequent proliferation of the biofilm. Besides determining the rate at which biofilms foul surfaces, the initial attachment of bacteria to surfaces is also thought to determine the structure and composition of a biofilm.[15] Thus control over biofilm formation (rate, structure, composition) requires understanding the factors that affect initial attachment and hence subsequent biofilm formation.

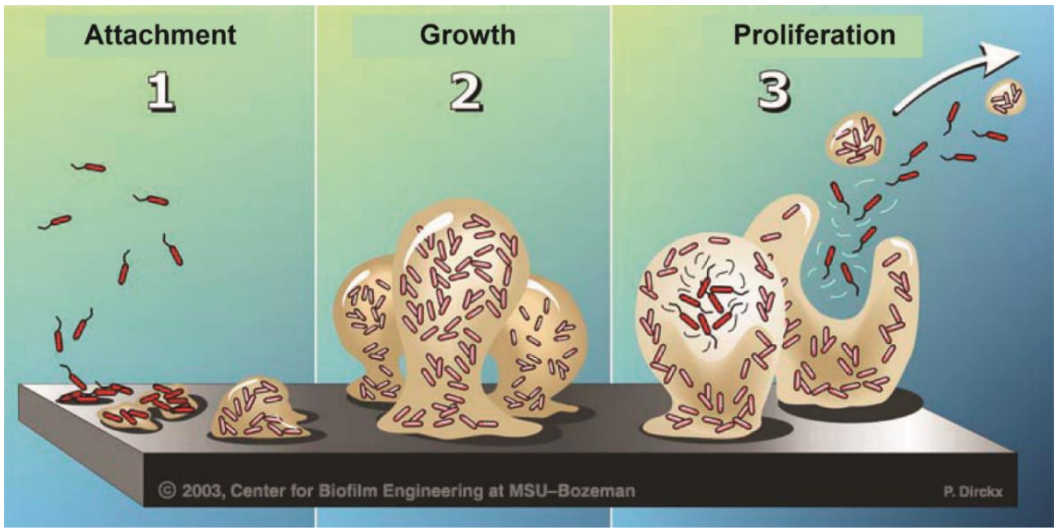

Figure 1.1. Stages in formation of a typical bacterial biofilm [Image credit: CBE, Montana State University]. Initial attachment (1) is followed by growth and multiplication of bacteria and secretion of exopolysaccharides that form the biofilm matrix (2) and finally by maturation and subsequent proliferation of biofilm (3).

1.3 Factors affecting initial attachment of bacteria

Bacteria are considered complex active colloids by their size [1-3 μm],[16] and by their ability to use their energy towards non-equilibrium activities such as reproduction, growth and motility. Because of the similarity in size to colloidal (microscale) particles, thermodynamic approaches and models for understanding attachment of colloids to surfaces have therefore been frequently applied to understand bacterial adhesion. Initial adhesion of bacteria to surfaces has typically been modeled using one of two approaches: (1) using a thermodynamic energy balance between bacteria, medium, and surface[17, 18] or (2) using colloid deposition models such as the Derjaguin-Landau-Verwey-Overbeek (DLVO) theory.[19, 20] In the Derjaguin-Landau-Verwey-Overbeek (DLVO) theory applied to bacteria[19, 20], the free energy is described as a balance between attractive Lifshitz-van der Waals and attractive or repulsive electrostatic forces. Additional forces, such as Lewis acid-base and Brownian forces, are included in the extended DLVO (xDLVO) approach to explain "hydrophobic attractive"[21] and "hydrophilic repulsive"[22] interactions. Besides physicochemical interactions, bacteria also possess surface-borne adhesins (Figure 1.2) such as pili,[23] flagella,[24, 25] fimbriae,[26, 27] lipopolysaccharides,[28] and extracellular polymeric substances.[29, 30, 31] These surface adhesins are known to facilitate attachment to surfaces; in addition, fimbriae and flagella are also thought to mediate irreversible attachment by penetrating the repulsive energy maximum very close to surfaces.[32] Finally, hydrodynamic forces arising from proximity to surfaces, hydrodynamic interactions between bacterial flagellar bundles and surfaces,[33, 34, 35] and solution chemistry[36, 37, 38] can all modify the physicochemical interactions and therefore

affect adhesion. Surface charge,[39, 40] wettability,[41, 42, 43] roughness,[44, 45] and microtopography[46, 47, 48] also affect the kinetics of bacterial deposition on surfaces.

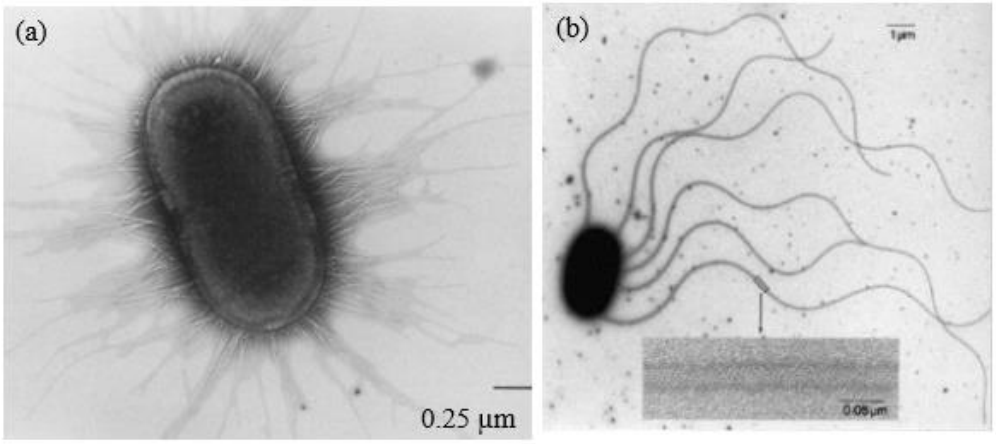

Figure 1.2. (a) Transmission electron micrograph of *E. coli* showing hair-like fimbriae.[49] (b) Transmission electron micrograph of *E. coli* showing peritrichously distributed flagella.[50] Scale bar in (b) is 1 μm.

1.4 Motivation for present work

Conventional anti-biofouling strategies include use of bactericidal agents and biocides in industrial applications and use of antibiotics in healthcare applications. Biocides and antifouling agents, however, have been found to adversely impact ecological balance[1] and result in environmental pollution.[51] For example, tributyltin was extensively used as biocidal agent in antifouling paints, wood preservation, cooling towers and slime controller in the paper industry. However, its use was regulated after studies associated exposure to tributyltin with disruption of the endocrine system in exposed humans and to acute toxicity for aquatic life-systems.[52] Similarly, bacteria are extremely robust to environmental stresses and are capable of mutating and evolving; hence multiple species of bacteria have developed mechanisms to remove or resist

antibiotics as a response to overexposure.[2] Use of antibiotics has thus been thought to cause and aggravate evolution of antibiotic-resistant strains. These and similarly deleterious outcomes indicate that conventional strategies to prevent bacterial fouling exhibit limited efficacy over long time.

The failure and shortcomings of conventional antifouling strategies, which target bacteria after biofilm formation, has inspired significant research interest in alternative strategies. One appealing alternate approach is to mitigate the initial attachment of bacteria to surfaces and hence prevent biofilms from forming. This approach, however, first requires understanding how bacteria attach to surfaces of a variety of physical properties. This scientific gap in knowledge motivates this thesis work.

Bacterial surfaces are heterogeneous spatially and may change over time with excretion of polysaccharides and/ or expression of proteins. Likewise, properties of ambient environment and that of surfaces may exhibit significant spatio-temporal fluctuation. Hence such dynamic heterogeneity requires establishing novel methods to design and evaluate surface properties and/or strategies to control bacterial attachment. This rational design approach requires a fundamental understanding of bacteria-surface interactions and adhesion mechanisms. Most extant bacteria adhesion experiments calculate the deposition rate by counting the number of bacteria attached to the surface as a function of time.[27, 28] These analyses, however, do not characterize the behavior of individual attached bacteria and thus cannot quantify variations arising due to time dependent changes and/ or dynamic adhesion behavior that may generate additional insight into mechanisms of bacterial attachment. A complementary approach is to employ high-throughput bacteria-tracking techniques to analyze the trajectories of hundreds to

thousands of individual bacteria on or near surfaces. These techniques have been used to identify individual and collective motility mechanisms used by bacteria on surfaces.[53, 54, 55, 56] However, they have not been used to explore the role of surface properties, of cell surface characteristics, or of medium properties for bacterial adhesion. It is expected that new metrics to characterize the rate of deposition, surface-associated motion, and near-surface mobility of bacteria at the scale of individual cells will generate improved understanding of the effects of these factors in initial attachment and subsequent biofilm formation.

1.5 Outline of research

Design of effective antifouling strategies to prevent biofilm formation requires fundamental understanding of how bacteria-surface interactions affect adhesion mechanisms. The development of fundamental understanding of adhesion processes related to these interactions is the primary goal of this project.

In the present work we investigate the role of surface properties, cell surface characteristics, and solution properties in mediating attachment and near surface motility using a high-throughput imaging and tracking approach. In the first part of the work (Chapter 2) we study the role of surface chemistry on adhesion of bacteria on surfaces of controlled chemistry, generated using silane deposition, during flow. We identify features of surface-associated motion that provide insight into the operating mechanisms of adhesion and establish metrics that correlate with the observed deposition behavior. In the second part (Chapter 3) of the work we study the role of surface roughness on bacterial adhesion and near surface mobility. We find that sub-nanoscale surface roughness significantly affects deposition rates and mobile adhesion of cells near the

surface. Finally, in the third part (Chapter 4) we study quiescent suspensions of bacteria in media of varying ionic strength and viscosity on both hydrophilic and hydrophobic surfaces. We find that the effect of polymer induced crowding and viscosity dominates the expected effect of solution chemistry and surface wettability on near surface motion and dynamics of bacteria. The overall summary and expected impact of this work as well as recommendations for future work are presented in Chapter 5.

Chapter 2 Initial attachment of *Escherichia coli* on silanized glass surfaces

2.1 Introduction

Bacteria irreversibly adhere to surfaces in the early stages of formation of bacterial biofilms[4], which shelter the enclosed bacteria within a protective extracellular polymeric matrix. Biofilms generate significant problems in human health: for example, biofilm-forming bacteria are a major cause of hospital-acquired infections.[3, 57] Similarly, biofouling of a wide variety of industrial and technological surfaces, including oil and water pipelines,[30] ship hulls,[10] and food processing equipment,[58] generates significant and deleterious costs. The structure and composition of biofilms depend on the interactions between bacteria and surfaces that mediate the initial attachment events.[15] Designing materials and coatings to prevent the formation of biofilms on surfaces thus requires understanding how surface properties affect bacteria-surface interactions.

Physicochemical interactions between bacteria and surfaces are typically described using one of two approaches. In the thermodynamic approach, the change in free energy as bacteria transition from planktonic to surface-attached is described in terms of interfacial tensions between the bacteria, fluid medium, and solid substrate.[17, 18] In the Derjaguin-Landau-Verwey-Overbeek (DLVO) theory applied to bacteria,[19, 20] the free energy is described as a balance between attractive Lifshitz-van der Waals and attractive or repulsive electrostatic forces. Additional forces, such as Lewis acid-base and Brownian forces, are included in the extended DLVO (xDLVO) approach to explain "hydrophobic attractive"[21] and "hydrophilic repulsive"[22] interactions. Beyond these physicochemical interactions, bacteria may also possess adhesins that enable them to

puncture the secondary energy maximum and attach irreversibly;[59] these include pili,[23] flagella,[24, 25] fimbriae,[27, 60] lipopolysaccharides,[28] and extracellular polymeric substances.[29, 30, 31] Adhesins that also serve as motility appendages, such as type IV pili or flagella, directly couple near-surface motility to adhesion.[48, 61, 62] Finally, hydrodynamic forces on the bacterium due to nearby surfaces[33, 34, 35] and the chemistry of the solution[29, 36, 37] modify the physicochemical and/or Brownian interactions and therefore also affect bacterial adhesion.

Surface properties affect the interactions between bacteria and surfaces and thereby modify the extent to which bacteria irreversibly attach to surfaces. For example, surface charge,[39, 40] hydrophobicity/hydrophilicity,[41, 42, 43] and micro-topography[46, 47, 48] affect the rate at which bacteria deposit on surfaces. The deposition rate is typically measured by counting the number of bacteria attached to the surface as a function of time.[27, 28] These analyses, however, do not typically characterize the behavior of individual attached bacteria and thus cannot quantify variations in behavior that may generate additional insight into mechanisms of bacterial attachment. A complementary approach is to employ high-throughput bacteria-tracking techniques to analyze the trajectories of hundreds to thousands of individual bacteria on or near surfaces. In this approach, a microscopy movie is translated into a database of searchable trajectories; subsequently, automated searches of these trajectories are designed to identify motility behaviors that are correlated with properties of interest. These techniques have been employed to identify individual and collective motility mechanisms used by bacteria on surfaces[30, 48, 54, 56] and thereby generate mechanistic understanding of the role of bacterial adhesins during early biofilm formation. By contrast, the role of surface properties in

mediating attachment and motility has not been explored through this high-throughput approach. New metrics to characterize the rate of deposition at the scale of individual bacteria will generate improved understanding of the effects of surface properties on the transition to irreversible attachment.

In this study, we employ automated high-throughput tracking methods to investigate the transition to irreversible attachment for bacteria deposited during flow onto silanized glass substrates. We study the bacterium *Escherichia coli*, a widely-studied model Gram-negative opportunistic pathogen that is usually benign and easy to isolate and culture in chemical media.[63] We track the position and orientation of every *E. coli* bacterium in microscopy movies acquired as cells are deposited onto surfaces bearing different self-assembled silane layers. We find that the deposition rate over short time scales is poorly correlated with two standard metrics used for surface properties, water contact angle and surface energy. Instead, we develop new metrics to characterize the extent of flagella-driven motion for bacteria that are transiently attached to the surface and show that a high degree of motion is inversely correlated with the rate at which bacteria are deposited. This approach allows us to separately track detaching bacteria and the fate of bacteria that initially exhibit a high degree of surface motion; we find that surfaces with a high deposition rate of bacteria typically have few detaching bacteria and a large fraction of moving bacteria that become immobilized. X-ray photoelectron spectroscopy (XPS) characterization of the silanized glass surfaces suggests that the chemistry and arrangement of silane molecules affect both the initial deposition and the transition to irreversible attachment for a given flow rate. The high-throughput approach

described here offers new opportunities to sensitively characterize motility behaviors correlated with this transition across a wide range of surface properties.

2.2 Materials and methods

2.2.1 Bacteria culture

Escherichia coli strain MC1061, which is derived from the K12 strain, was used in this study (strain courtesy of Prof. Patrick Cirino and Christopher Frei, University of Houston). A plasmid (pFG10) for an enhanced green fluorescence protein (GFP) and chloramphenicol resistance was introduced into the cells. The plasmid enabled the cells to constitutively express GFP and allowed cells to be visualized under fluorescence without external labeling.

Bacteria were streaked on Luria Bertani-Agar plates (5 grams yeast extract, 10 grams of Bacto-tryptone, 5 g NaCl, 15 grams agar, all from BD Chemicals) containing 25 µg/ml of chloramphenicol (Spectrum) and incubated overnight at 37ºC (Nuvaire Inc.). Single colonies from the plate were used to inoculate 50 mL sterile Luria Bertani medium, (5 g yeast extract, 5 g NaCl and 10 g tryptone per 1 liter medium, BD Chemicals) containing 25 µg/ml of chloramphenicol and incubated in an orbital incubator shaker (New Brunswick Scientific) at 190 rpm and 37ºC for approximately 17—18 hours. To create a dense pellet, cells were centrifuged at 5000g in a Sorvall ST 16 Centrifuge (Thermo Fisher Scientific) for 20 minutes. After pelleting, the cells were re-suspended in 0.9% NaCl solution (ionic strength 154 mM). Cells were washed twice in NaCl by repeated mixing, centrifuging, and re-suspension to remove the growth medium. Finally, for all imaging experiments the cells were suspended in 154 mM NaCl and diluted volumetrically to an optical density (measured at a wavelength of 600 nm) OD600 of

0.42 (with a background subtraction of 0.03 applied), which was measured using a micro-plate reader (Infinte200 Pro, Tecan). Cells in all experiments were in a stationary stage of growth, based on a growth curve generated by measuring the OD600 of a growing culture at 30-minute intervals for 24 hours. To approximately correlate the optical density (which measures the biomass concentration) to viable cell number density, a plate count assay was performed. For two different cultures, an optical density of 1 was found to correspond to a viable cell number density of approximately 10^8 colony forming units/mL.

2.2.2 Microbial adhesion to hydrocarbons test (MATH) and bacterial electrophoretic mobility

The percentage hydrophobicity of the cells was measured using the MATH test with two solvents, hexadecane and *n*-dodecane,[64] as 8.9 ± 1.3 % for *n*-dodecane and 6.9 ± 3.6 % for hexadecane. The electrophoretic mobility of the cells was measured using a NICOMP 380 ZLS zeta potential analyzer (Particle Sizing Systems) at ionic strengths of 15.4 and 1.54 mM due to working limitations of the instrument. Using the Smoluchowski equation,[65] we calculated the zeta potential from the electrophoretic mobility as -42 ± 2 mV at 15.4 mM ionic strength and -58 ± 2 mV at 1.54 mM ionic strength.

2.2.3 Substrate preparation

Substrates for deposition experiments were prepared by vapor or solution deposition of organosilanes on glass. Prior to deposition, glass coverslips with dimensions 48 × 65 mm^2 (thickness 0.13—0.17, Gold Seal) were first cleaned by

successive sonication in acetone (Macron, AR grade) and double de-ionized (DI) water (resistivity 18.2 MΩ-cm, Millipore water purification system) and then treated with air plasma for two minutes. For deposition of 3-aminopropyltriethoxysilane (APTES) (99% Sigma) and 3-aminopropyltrimethoxysilane (APTMS) (95%, Gelest), a 1% (wt.) solution of silane in ethanol containing 5% DI water was prepared and stirred for 5 minutes. Clean slides were immersed in the solution for five minutes with continuous stirring. Slides were rinsed in ethanol (200 proof, Devcon) and isopropanol (99%, Sigma); APTMS-coated slides were additionally rinsed with DI water. Slides were dried under nitrogen stream and baked at 110°C for 10 minutes. To deposit glycidoxypropyltriethoxysilane (GPTS) (95%, Gelest), clean slides were immersed in a 0.02 M GPTS solution in toluene (98% Sigma) for 210 minutes. After immersion, slides were rinsed twice in each of toluene, methanol (98%, Devcon) and DI water and dried under nitrogen. Octyldimethylchlorosilane (ODMCS) (95% Gelest) was deposited from vapor in a vacuum desiccator held at 30 mm Hg for 30 hours. After deposition of ODMCS, the slides were sonicated in four solutions: a 1:1 (v/v) mixture of deionized water and chloroform for five minutes, in toluene for two minutes, in isopropyl alcohol for one minute and finally in deionized water for one minute and dried under nitrogen. Octadecyltricholorosilane (OTS) (95%, Gelest) was deposited by immersing a clean slide in a freshly prepared 0.5 mM OTS solution in anhydrous toluene (99.8%, Sigma) for 17 hours in an airtight jar. After deposition, the slides were sonicated in chloroform (99.8%, Sigma), acetone (HPLC grade) and DI water sequentially and dried in nitrogen. All silanized substrates were placed in petri dishes, sealed with Parafilm, and stored in a desiccator for no more than two days before use.

2.2.4 Surface characterization

Water contact angles were measured using a Dataphysics OCA 15EC goniometer. Reported data correspond to at least five spot measurements made on three surfaces. Contact angles for two other test liquids, ethylene glycol (99%, Alfa Aesar) and diiodomethane (99%, Alfa Aesar), were measured for each surface and the surface energy was calculated using algorithms built into the instrument's analysis package, which were based on the method of Wu.[66] To characterize the elemental composition of APTES- and APTMS-coated surfaces, photoelectrons produced via a monochromatic Al-kα x-ray source (1486.6 eV) operated at 350 W were collected on a Physical Electronics Model 5700 X-ray photoelectron spectroscopy (XPS) instrument. The analyzed area, collection solid cone, and take-off angle were set at 800 μm, 5°, and 45° respectively. Applied pass energy of 23.52 eV resulted in an energy resolution of better than 0.51 eV. All spectra were acquired after vacuum of 5×10^{-9} torr was attained. The binding energy scales were referenced to 284.6 eV, corresponding to the maximum intensity for a C 1s spectrum. Data processing was carried out using the Multipak™ software package (Ulvac-PHI, Physical Electronics). A Shirley background subtraction routine[67] was applied throughout.

2.2.4.1 Zeta potential measurements

To estimate the surface zeta potential, silica nanoparticles of nominal diameter 170 nm (Bangs Laboratories) were functionalized with silanes. ODMCS was deposited by stirring nanoparticles in a 0.1 % (w) solution of ODMCS in toluene for 17 h followed

by successive washing in toluene, methanol and DI water. Particles were washed by successive vortex mixing and centrifugation at 5000 g for 10 minutes for separation in the respective solvents. For all other silanes, the same deposition protocol used for the glass coverslips was also employed for nanoparticles. The zeta potential for these particles in solutions of ionic strength at an ionic strength of 154 mM was measured using a NanoBrook ZetaPALs (Brookhaven Instruments) analyzer.

2.2.5 Flow experiments and image analysis

In deposition experiments, suspensions of bacteria were flowed through a linear channel[68] (Figure 2.1 (a)) at volumetric flow rates of Q = 0.1, 0.3 or 1 mL/min using a syringe pump (Model 11, Harvard Apparatus). The experimental set-up (Figure 2.1(a)) consisted of a coverglass substrate (silane-functionalized or bare/plasma treated, as a control) onto which a molded polyethylene cell (Biocentrum DTU) was attached with double- sided adhesive tape (Dow Corning Electronics). The width, height, and length of the flow channel were W = 4 mm, $2b$ = 2 mm and h = 40 mm, respectively (Figure 2.1(b)). At flow rates of 0.1, 0.3, and 1 mL/min, the shear rates were $\dot{\gamma} = 6Q/Whb =$ 0.0625, 0.1875, and 0.625 s^{-1}, respectively, and the shear stresses were $\sigma = 6Q\mu/Whb =$ 0.05, 0.15, and 0.5 N/m^2, respectively, where μ was the viscosity of water.

Bacteria deposited on the substrates during flow were imaged using a confocal fluorescence scanner (VT Infinity, Visitech) attached to a Leica DM4000 inverted microscope equipped with a 100x oil immersion lens (HCX PL APO of numerical aperture 1.4) and laser excitation source λ = 488 nm. One image with an exposure time of 0.3 s and a pixel size of 0.125 ± 0.0006 μm was acquired every three seconds using an

ORCA 200 camera (Hammamatsu) that was controlled by Voxcell Scan Software (Visitech).

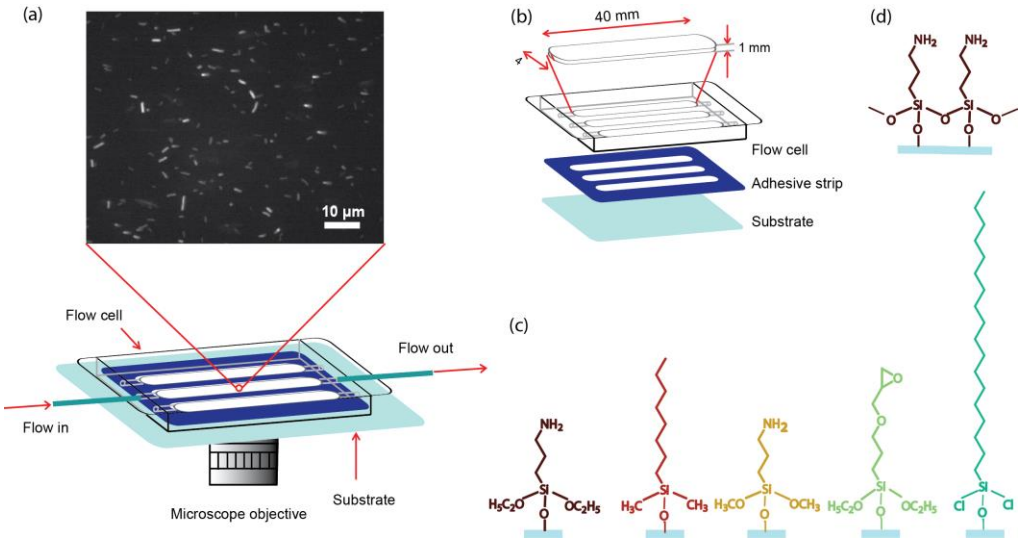

Figure 2.1. (a) Schematic of the experimental set-up used in flow cell experiments. (b) Exploded view of flow cell assembly. (c) Chemical structures of single organosilane molecules as expected to be deposited on glass substrates, left to right: 3-aminopropyltriethoxysilane (APTES), octyldimethylchlorosilane (ODMCS), 3-aminopropyltrimethoxysilane (APTMS), 3glycidoxypropyl-triethoxysilane (GPTS), and octadecyltrichlorosilane (OTS). (d) Structure of an APTES monolayer attached to glass, showing expected cross-linked structure.

In a typical deposition experiment, 200 images with an area of 84 × 64 µm^2 (corresponding to 672 pixels × 512 pixels) were acquired after at least two bacteria were deposited in the field of view. Experiments on each surface were performed in triplicate; at least one experiment in each trio was performed on a different substrate and with a different bacteria culture. Total number of bacteria images analyzed and number of bacteria for each experimental replicate are shown in Table 2.1.

Single bacterium-tracking algorithms, written in IDL (Exelis VIS) and based on algorithms used to track rodlike colloidal particles[69] and modified for elongated

bacteria,[54] were employed to locate and track every bacterium in a time series of microscopy images. Further analysis of the attachment and detachment rates and orientations of bacteria was performed using routines written in Matlab (MathWorks) and in IDL.

Table 2.1. (Left) Total number of bacteria images (corresponding to attached bacteria) and (right) total number of bacteria analyzed for each experimental replicate.

Substrate (flow rate [mL/min])	**Replicate 1**		**Replicate 2**		**Replicate 3**	
APTES (1)	22251	315	22337	345	26987	352
ODMCS (1)	17782	321	20673	405	21182	435
APTMS (1)	18863	244	19344	282	19533	298
Unmodified glass (1)	12228	230	13943	262	14252	270
GPTS (1)	11563	296	13753	309	13995	316
OTS (1)	8399	187	9826	205	10229	218
Plasma-treated glass (1)	3483	90	4358	106	4715	158
APTES (0.1)	4488	101	3060	80	5195	125
APTES (0.3)	18136	281	17511	314	13738	238
ODMCS (0.1)	3458	109	4534	75	4074	75
ODMCS (0.3)	18845	291	19234	380	13023	238
OTS (0.1)	3483	51	4805	107		
OTS (0.3)	9024	140	9222	202		

2.3 Results and discussion

Earlier experiments on *E. coli* showed that self-assembled layers of silanes can inhibit bacterial adhesion and biofilm formation[30, 70] and that the chemical details of the silane layer sensitively affected the force of bacterial adhesion.[71] We therefore deposited silanes on glass surfaces as a model system in which to investigate the transition to irreversible attachment across a range of surface chemistries. We first measured the number of *E. coli* bacteria that attached to each surface over time when exposed to a

constant flow rate of 1 mL/min. The number of cells deposited on the surface over time varied with the surface chemistry, as shown in Figure 2.2. At times greater than two minutes the slope of each curve was nearly linear, allowing the rate at which bacteria were deposited on each surface to be calculated from the long-time slope.

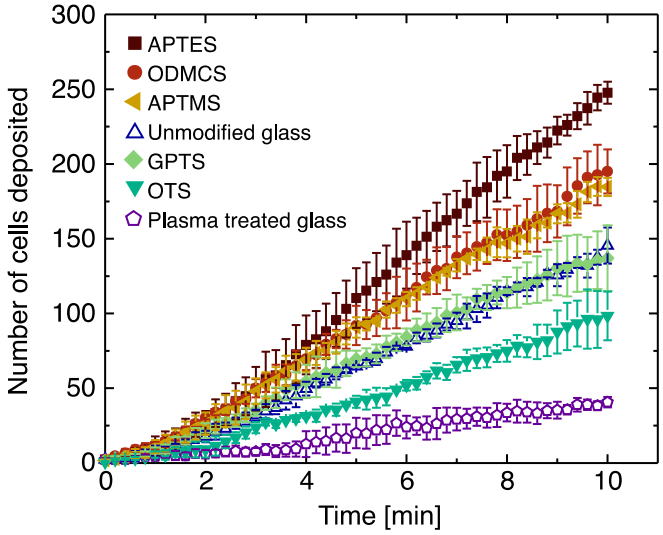

Figure 2.2. Number of *E. coli* bacteria deposited on the surface as a function of time for surfaces bearing silane molecules (closed symbols) and for glass surfaces without silanes (open symbols) at a suspension flow rate of 1 mL/min. The initial time for each experiment (t = 0) was chosen as the time at which two cells were initially deposited on the surface. Error bars indicate standard deviations over three replicates.

The deposition rate of *E. coli* at a flow rate of 1 mL/min was a non-monotonic function of two surface properties frequently used to characterize surfaces, surface hydrophobicity (measured as water contact angle) and surface energy (Figure 2.3). The greatest deposition rates were observed for hydrophilic APTES and APTMS surfaces and hydrophobic ODMCS surfaces, whereas the lowest deposition rates were observed on the extremely hydrophilic plasma-treated glass surface and on the superhydrophobic OTS surface. Moreover, surfaces of similar energy could exhibit strikingly different rates of

bacterial deposition. The cationic APTES and APTMS surfaces and the neutrally charged GPTS surface had similar surface energies. The deposition rate on GPTS, however, was comparable to that on unmodified clean glass, whereas the rate on the two cationic surfaces was a factor of two greater. Measurements of the zeta potential of silane-functionalized nanoparticles of diameter 170 nm showed a greater correlation to deposition rate (Figure 2.4), although surfaces of similar zeta potential (*e.g.*, approximately neutral GPTS, ODMCS, and OTS, or positively-charged APTES and APTMS) still exhibited differences in deposition rate. These results indicated that surface chemistry affected the rate at which cells were initially deposited in a nontrivial fashion, consistent with earlier reports that argued that molecular details sensitively affected the extent of deposition.[71]

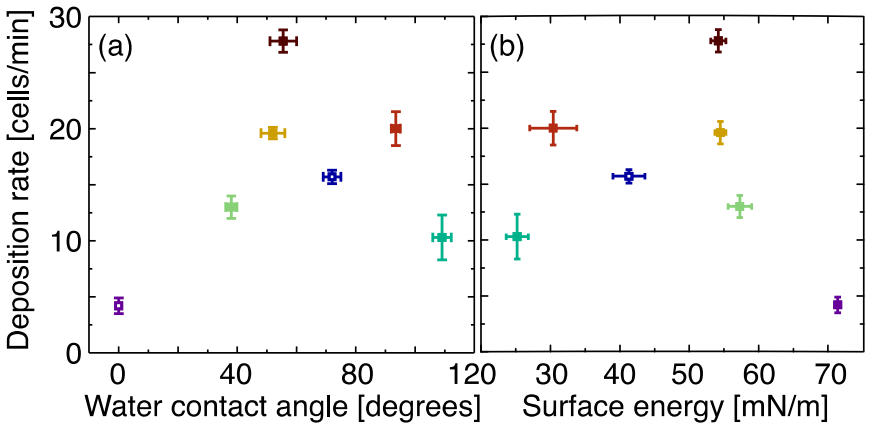

Figure 2.3. Deposition rate (cells/minute) at a suspension flow rate of 1 mL/min as a function of (a) the water contact angle and (b) the surface energy. Error bars indicate standard deviations measured from: triplicate replicates (for deposition rate), at least five spot measurements on at least three substrates (for water contact angle) and at least two surfaces (for surface energy). Colors correspond to those used in Figure 2.2.

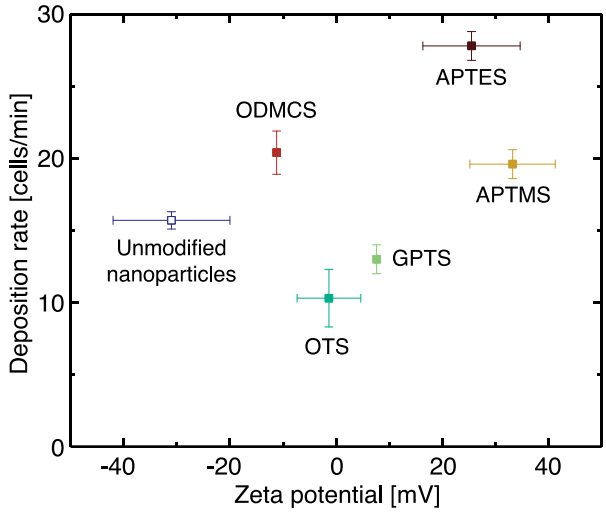

Figure 2.4. Deposition rate of bacteria as a function of zeta potential of silanized silica nanoparticles at a fixed flow rate of 1 mL/min.

To gain insight into the mechanisms that mediated initial attachment of *E. coli*, we examined the trajectories of every bacterium deposited onto these surfaces. Although most bacteria (~90%) remained in the field of view for at least twenty-four seconds and were thus at least transiently attached to the surface, the degree of motion varied significantly between trajectories. Some bacteria were nearly immobile after attaching to the surface (Figure 2.5 (a)), whereas other bacteria flipped back and forth between two positions (Figure 2.5 (b)) or rotated in a circle while tethered (Figure 2.5 (c)). *E. coli* possesses only one type of appendage that generates rotation, the flagellum, and flagellum-tethered *E. coli* can rotate when attached to surfaces.[72, 73, 74] We therefore posit the observed flipping and rotating was generated by flagella. This transient motion, which did not generate net displacement, is different than other transient mechanisms used by *E. coli* to attach to surfaces, such as weak rolling adhesion mediated by fimbriae[75] in which the center-of-mass of the cell translates laterally. From the microscopy movies, we observed that bacteria were more likely to flip and rotate on surfaces with lower

deposition rates (*e.g.*, OTS and plasma-treated glass) than on surfaces to which they rapidly attached (*e.g.*, APTES).

To quantify differences in the extent of transient motion of bacteria on surfaces of varying chemistry, we calculated the displacement of the centroid of each bacterium at each time step. The displacements of the bacteria shown in Figure 2.5 (a)—(c) increased from top to bottom, consistent with an increase in extent of motion that is likely driven by transient flagella-mediated attachment. We therefore calculated a cumulative percentage of displacements that were smaller than a cutoff value *D*, measured in microns.

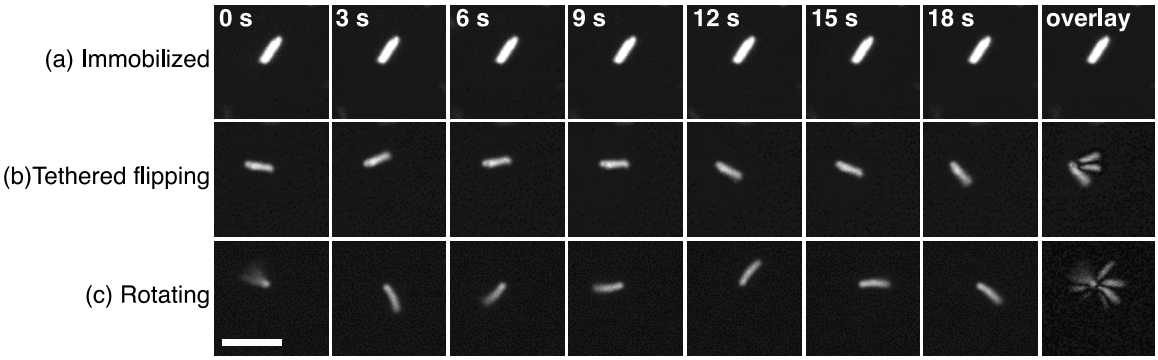

Figure 2.5. Time series of confocal micrographs depicting three characteristic types of bacterial motion: (a) immobilized; (b) tethered flipping, in which the bacterium flips between few positions in the surface plane; (c) rotating while tethered to the surface. The last image in each row is an overlay of all images in the time series. The initial time step (0 s) is different for each series. The scale bar is 5 μm.

At every fixed value of *D*, the APTES-coated and plasma-treated glass surfaces exhibited the highest and lowest cumulative percentages of displacements that were smaller than *D*, respectively (Figure 2.6). Many antimicrobial peptides bear positively-charged moieties, and positively-charged surfaces can exhibit antimicrobial activity.[76] We thus performed a live-dead assay to determine whether the APTES and APTMS surfaces were bactericidal.

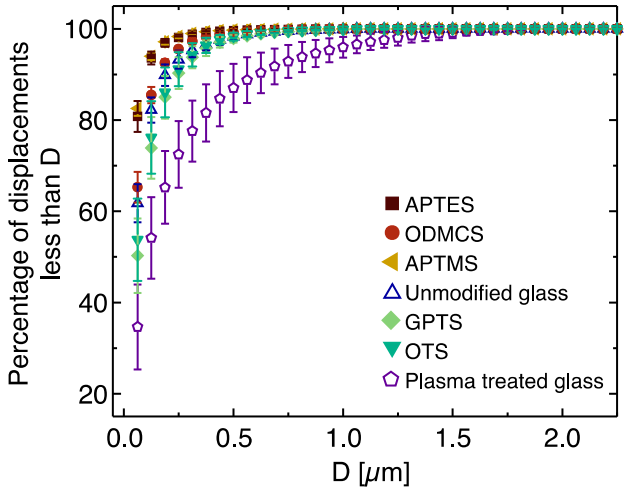

Figure 2.6. Cumulative percentage of bacteria deposited at a suspension flow rate of 1 mL/min that exhibit a displacement of less than *D* microns for surfaces of different chemistries. Error bars indicate standard deviation over three replicates. Symbols and colors correspond to those used in Figure 2.2. The total number of attached cell positions analyzed for each replicate on each substrate was: APTES (N=22251, 22337, 26987), ODMCS (N=17782, 20673, 21182), APTMS (N=18863, 19344, 19533), unmodified glass (N=12228, 13943, 14252), GPTS (N=11563, 13753, 13995), OTS (N=8399, 9826, 10229), and plasma-treated glass (N=3483, 4358, 4715).

2.3.1 Live-dead analysis for bacteria attached to cationic surfaces and statistical significance.

At the end of a typical deposition experiment, the flow was stopped and 300 µL of propidium iodide (PI) stain (0.1% in PBS) (BactLight bacterial viability kit L7012, Life Technologies) was injected into the flow cell. Cells were incubated with dye for ten minutes in the dark and subsequently imaged with brightfield microscopy. Images of live (dead) cells were acquired at 488 (561) nm excitation wavelengths using an Olympus camera (DP21). The number of dead and live cells were counted using ImageJ. At least three sets of images were acquired for each surface. Control measurements for

proportions of dead cells were performed on unmodified glass with the same PI concentration and same bacterial sample suspension both for APTES and APTMS.

To compare the two sample proportions p_1 and p_2, p-values were calculated as $p_i = \frac{x_i}{n_i}$, where x_i is the number of successes in the sample (here, number of dead cells) and n_i is the size of the sample (here, total number of cells). We assumed that the proportions being compared were independent and for both samples there were at least five successes and 5 failures (which was true for all experiments in which we calculated p values). The pooled estimate of p_1 and p_2 is given as $\bar{p} = \frac{x_1 + x_2}{n_1 + n_2}$ and the z-statistic for the two proportions (with H0: $p_1 = p_2$) is calculated as $z = \frac{p_1 - p_2}{\sqrt{\frac{\bar{p}\bar{q}}{n_1} + \frac{\bar{p}\bar{q}}{n_2}}}$, where $\bar{q} = 1 - \bar{p}$.

The area to the left of the test statistic (A) is determined from the z-score tables and p-value calculated as either A or 1-A (for right tailed test). A p-value less than the significance level of $\alpha = 0.05$ indicates that the null hypothesis of $p_1 = p_2$ can be rejected, *i.e.*, the compared proportions are significantly different.

Table 2.2. Percentage of dead cells for cationic surfaces as compared to control surfaces (unmodified glass)

	Percentage of dead cells [Standard deviation]		***p* values**
	Substrate	Control	
APTES	9.5 [1.2]	4.7 [3.8]	0.1056
APTMS	4.1 [1.1]	3.3 [0.1]	0.28

Staining of deposited cells with propidium iodide showed that over 90% of cells deposited onto APTES and APTMS remained viable, and the proportion of dead cells observed on the cationic surfaces (APTES, APTMS) did not significantly differ from that

on unmodified glass substrates (Table 2.2). Finally, at every fixed value of *D* bacteria attached to neutral GPTS surfaces exhibited significantly more motion than those attached to cationic APTES or APTMS surfaces, suggesting that different mechanisms mediate deposition on surfaces of different chemistries yet similar surface energies.

This interpretation of the cumulative percentage displacements in Figure 2.6 suggests that the degree of surface motion may signal the propensity of bacteria to attach to these surfaces. We defined as motility metric the percentage of displacements greater than 0.12 microns, corresponding to the second bin in Figure 2.6. For a suspension flow rate of 1 mL/min, this metric was inversely correlated with the deposition rate (R^2 = 0.84), as shown in Figure 2.7: surfaces with a large (small) fraction of moving bacteria exhibited low (high) deposition rates. Differences between the percentages of displacements greater than 0.12 microns between any two pairs of substrates were significant at the level of $p < 0.01$ (Table 2.3). This inverse correlation is striking when compared to the lack of correlation seen between deposition rate and the traditional surface characterization metrics shown in Figure 2.3 and Figure 2.4 (R^2 = 0.11 for water contact angle, R^2 = 0.039 for surface energy, and R^2 = 0.193 for zeta potential). A similar correlation was obtained for other cutoff values for the cumulative displacement. Because the mechanisms of surface motion (flipping and rotation, as in Figure 2.5) were driven by flagella, these results suggest that attachment mediated by a flagellum is weaker than that mediated by strong and short-ranged electrostatic, van der Waals, and/or hydrophobic interactions between the bacterial body and the surface. Experiments performed at lower flow rates (0.1 and 0.3 mL/min) also exhibited the same trend of increasing deposition rate with decreasing motility within experimental errors (R^2 = 0.67), as shown by the

triangles and stars in Figure 2.7. By contrast, surface energy, water contact angle, and zeta potential could not account for changes in deposition rate as a function of flow rate. Our motility metric may therefore provide information on time-dependent and/or dynamic bacterial adhesion that cannot be obtained *via* other methods to characterize surfaces.

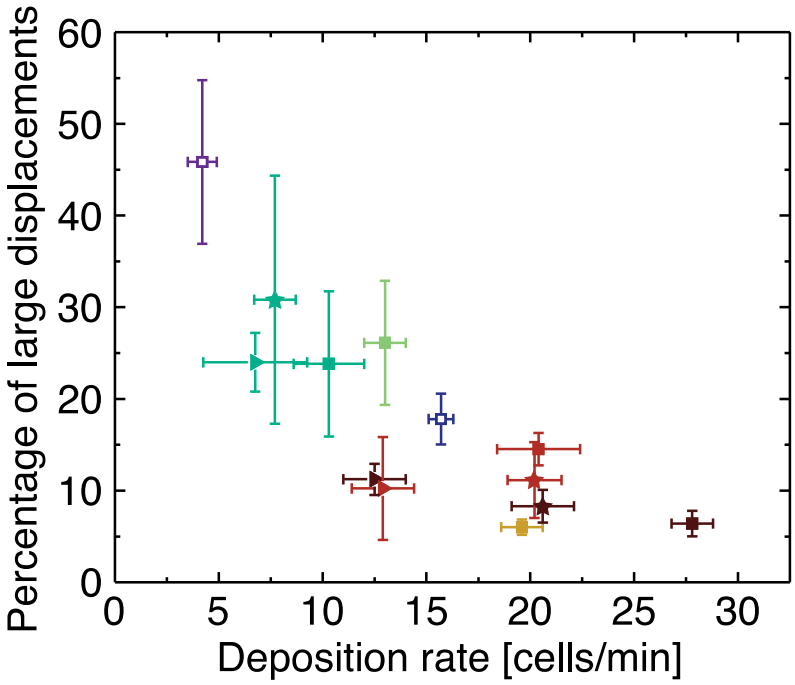

Figure 2.7. Percentage of large displacements (greater than 0.12 μm) as a function of deposition rate (in cells/minute). Error bars indicate standard deviation over three replicates. Colors correspond to those used in Figure 2.2. Shapes correspond to measurements at different suspension flow rates for selected substrates: 0.1 mL/min (triangles), 0.3 mL/min (stars), and 1.0 mL/min (squares). The total number of attached cell positions analyzed for each replicate acquired at 1.0 mL/min on each substrate was: APTES (N=22251, 22337, 26987), ODMCS (N=17782, 20673, 21182), APTMS (N=18863, 19344, 19533), unmodified glass (N=12228, 13943, 14252), GPTS (N=11563, 13753, 13995), OTS (N=8399, 9826, 10229), and plasma-treated glass (N=3483, 4358, 4715).

Table 2.3. *P* values for comparison of the percentage of large displacements between all pairs of surfaces prepared for this study.

Flow rate = 1mL/min						
	APTES	**ODMCS**	**APTMS**	**GLASS**	**GPTS**	**OTS**
PTG	0.0001	0.0001	0.0001	0.0001	0.0001	0.0001
OTS	0.0001	0.0001	0.0001	0.0001	0.0001	
GPTS	0.0001	0.0001	0.0001	0.0001		
GLASS	0.0001	0.0001	0.0001			
APTMS	0.004	0.0001				
ODMCS	0.0001					
	Flow rate = 0.1 mL/min			**Flow rate = 0.3 mL/min**		
	OTS	**ODMCS**		**OTS**	**ODMCS**	
APTES	0.0001	0.07		0.0001	0.0001	
ODMCS	0.0001			0.0001		
APTES						
flow rate	**0.1**	**0.3**				
1	0.0001	0.0001				
0.3	0.0001					
OTS						
flow rate	**0.1**	**0.3**				
1	0.0001	0.0001				
0.3	0.0001					
ODMCS						
flow rate	**0.1**	**0.3**				
1	0.0001	0.0001				
0.3	0.0094					

2.3.2 **Extended-DLVO (xDLVO) calculations**

We further sought to understand bacteria-surface interactions in these systems by using the extended DLVO model applied for colloids to estimate the interaction potential between a bacterium and surface. The interaction of a rigid and spherical bacterium (*b*)

with a planar surface (s) in a medium (m) is calculated in the extended-DLVO (xDLVO) theory as[77]

$$\Delta G^{total} = \Delta G^{LW} + \Delta G^{AB} + \Delta G^{EL}, \quad (2.1)$$

where the superscripts indicate the individual contributions from Lifshitz-van der Waals (LW), acid base (AB) and electrostatic (EL) interactions. These contributions are estimated as

$$\Delta G^{LW} = 2\pi r d_0 \Delta G_{d_0}^{LW} \frac{d_0}{d}, \quad (2.2)$$

$$\Delta G^{AB} = 2\pi r \Delta G_{d_0}^{AB} \lambda \exp\left(\frac{d_0 - d}{\lambda}\right) \text{ , and} \quad (2.3)$$

$$\Delta G^{EL} = \pi \varepsilon \varepsilon_0 r \left[2\varphi_1 \varphi_2 ln\left(\frac{1+\exp(-\kappa d)}{1-\exp(-\kappa d)}\right) + (\varphi_1^2 + \varphi_2^2)\ln(1 - \exp(-2\kappa d))\right], \quad (2.4)$$

where r is the equivalent radius of the bacterium taken as 0.7 μm,[78] d is the separation distance from the substrate, d_0 is the minimum equilibrium distance (~0.158 nm), and λ is the characteristic decay length of acid-base interaction in water (0.6 nm),[79] and

$$\Delta G_{d_0}^{LW} = -2\left(\sqrt{\gamma_b^{LW}} - \sqrt{\gamma_m^{LW}}\right)\left(\sqrt{\gamma_s^{LW}} - \sqrt{\gamma_m^{LW}}\right) \text{ and} \quad (2.5)$$

$$\Delta G_{d_0}^{AB} = 2\left[\begin{array}{c}\left(\sqrt{\gamma_b^+} - \sqrt{\gamma_s^+}\right)\left(\sqrt{\gamma_b^-} - \sqrt{\gamma_s^-}\right) - \left(\sqrt{\gamma_b^+} - \sqrt{\gamma_m^+}\right)\left(\sqrt{\gamma_b^-} - \sqrt{\gamma_m^-}\right) - \\ \left(\sqrt{\gamma_s^+} - \sqrt{\gamma_m^+}\right)\left(\sqrt{\gamma_s^-} - \sqrt{\gamma_m^-}\right)\end{array}\right]. \quad (2.6)$$

Here γ_i^{LW} , γ_i^+, and γ_i^- are the Lifshitz van der Waals, electron-acceptor (acid), and electron donor (base) component of the surface energy, ε is the relative permittivity of medium (taken as 80 for water), and ε_0 is the permittivity of free space (8.85×10^{-12} $s^4A^2m^{-3}kg^{-1}$). φ_1 and φ_2 are the surface potentials for bacteria and substrate, which are related to the respective zeta potentials (ζ_1 and ζ_2) as

$$\varphi_1 = \zeta_1 \left(1 + \frac{z}{r}\right) \exp(\kappa z) \text{ and} \quad (2.7)$$

$$\varphi_2 = \zeta_2. \quad (2.8)$$

Here κ is the inverse Debye length, which for the 1:1 electrolyte NaCl is 3.28×10^9 $I^{1/2}$, where I is the ionic strength of solution (0.154 M); *z* is defined as the slipping distance (~0.3 nm).

Table 2.4. Values for surface energy and zeta potentials used in the XDLVO calculations

	E. coli	**OTS**	**APTES**
γ_i^{LW} **[mJ/m^2]**	36.3*	28.94	41.07
γ_i^+ **[mJ/m^2]**	0.2*	0	0
γ_i^- **[mJ/m^2]**	64.4*	0.5	31.73
ζ_i **[mV]**	-25#	-1.5	25.5

*Values taken from Wang *et al.*[78]

#Values taken from Walker *et al.*[64]

All other values were measured.

Extended DLVO (xDLVO) calculations showed that the silanized surface with the highest and lowest deposition rates at 1 mL/min, APTES and OTS, respectively, both

exhibited a deep primary minimum (Figure 2.8) suggesting that both surfaces would favor strong adhesion. The departure of experimental results from the prediction of DLVO theory suggests that the theory is insufficient in describing bacteria-surface interactions in these experiments.

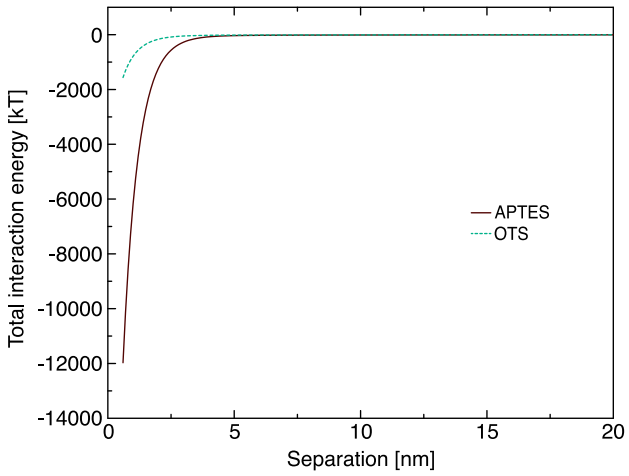

Figure 2.8. Total interaction potential (in units of kT) calculated from xDLVO theory for a sphere-plate interaction as a function of surface-surface separation distance for APTES (solid line) and OTS (dashed line) surfaces in suspensions of ionic strength 154 mM

We further probed the relationship between the degree of surface motion and the deposition rate by classifying the motion and attachment fate of each transiently attached bacterium. Trajectories of bacteria of duration shorter than twenty-four seconds, corresponding to bacteria that attach to the surface for only a short time, are indicated by gray bars in Figure 2.9. The percentage of bacteria that exhibited such short trajectories was inversely proportional to the deposition rate, with the smallest percentage of short trajectories observed on APTES and APTMS surfaces and the largest percentage observed on plasma-treated glass.

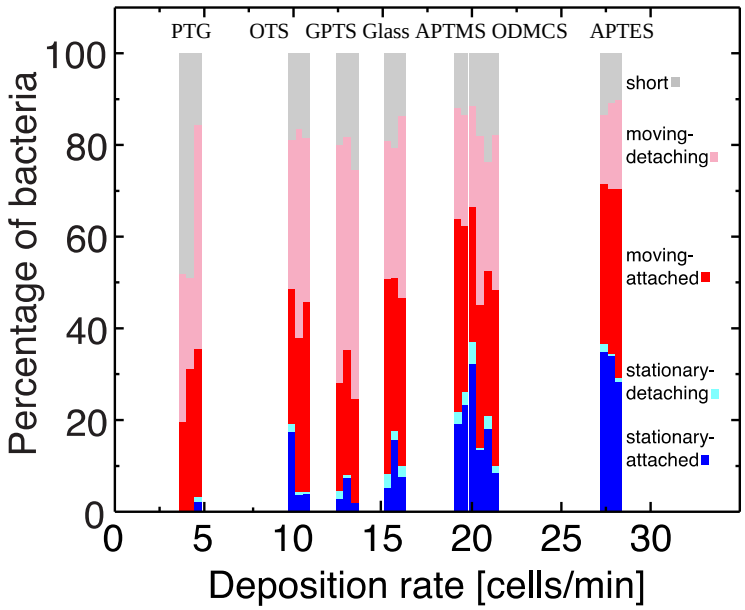

Figure 2.9. Classification of bacteria as a function of deposition rate, as stationary or moving and as attached or detaching, for a suspension flow rate of 1 mL/min. Colors: stationary and attached (dark blue), stationary and detaching (light blue), moving and attached (dark red), moving and detaching (light red); bacteria with trajectories too short to be analyzed are shown in gray. Each vertical bar represents one replicate experiment at a given deposition rate. The total number of bacteria analyzed for each replicate on each substrate was: APTES (N=315, 345, 352), ODMCS (N=321, 405, 435), APTMS (N=244, 282, 298), unmodified glass (N=230, 262 and 270), GPTS (N=296, 309, 316), OTS (N=187, 205, 218), and plasma-treated glass (PTG) (N=90, 106, 158).

Longer trajectories in which the centroid of the bacterium was displaced by at least 0.12 microns between consecutive images were classified as moving; all other longer trajectories were classified as stationary. Longer trajectories of bacteria that left the field of view before the end of the experiment were classified as detaching; all other longer trajectories were classified as attached. For all surfaces, only a tiny fraction of stationary bacteria detached during the experiment. Generally, as the deposition rate increased, the percentage of stationary and attached trajectories increased and the

percentage of moving and detaching trajectories decreased; this metric was less sensitive, however, to the initial flow rate than to the surface chemistry (Figure 2.10). Similar to this observation the extent of surface associated motion was also found to be more sensitive to surface chemistry than flow rate (Figure 2.11) The number of bacteria that detached during each experiment at a suspension flow rate of 1 mL/min typically decreased slightly as the deposition rate increased, as shown in Figure 2.12; this trend, however, did not hold at lower flow rates, where the detachment rates were lower (Figure 2.13). Finally, surfaces on which a large fraction of bacteria exhibited a high degree of surface motion through flagellum-driven flipping or rotation exhibited reduced deposition rates. This observation is consistent with either or both of two potential explanations: flagellum-driven motion helps cells to detach,[48] or that the surface properties correlated with high deposition rates increase the likelihood that bacteria attach irreversibly using other mechanisms.

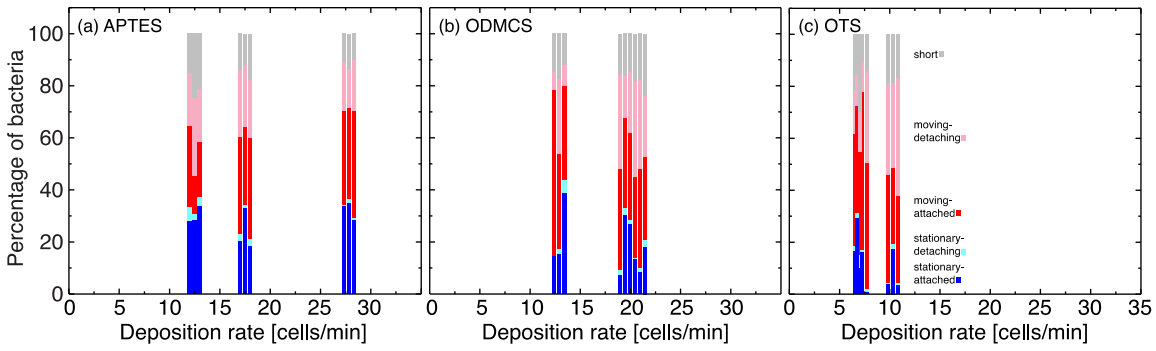

Figure 2.10. Classification of bacteria as stationary or moving and as attached or detaching as a function of deposition rate for (a) APTES, (b) ODMCS, and (c) OTS surfaces at different flow rates of 0.1, 0.3, and 1 mL/min (left to right in each plot).

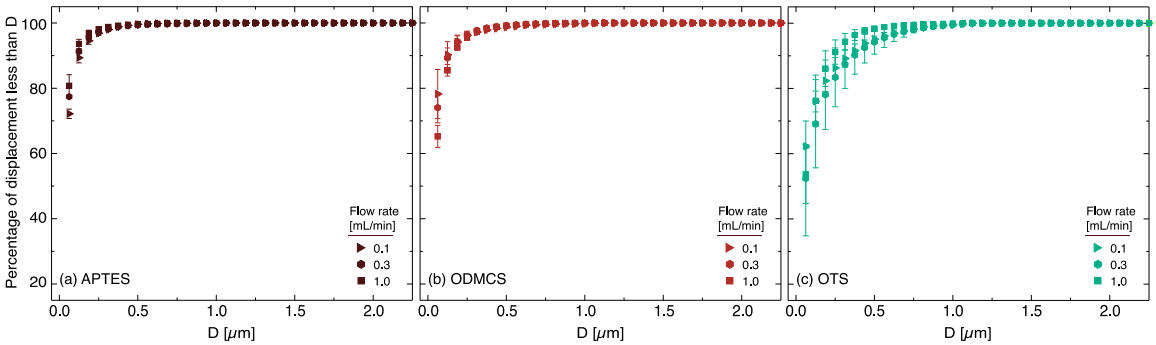

Figure 2.11. Percentage cumulative displacement less than D for (a) APTES, (b) ODMCS, and (c) OTS surfaces at three different flow rates of 0.1 (triangles), 0.3 (hexagons), and 1.0 (squares) mL/min.

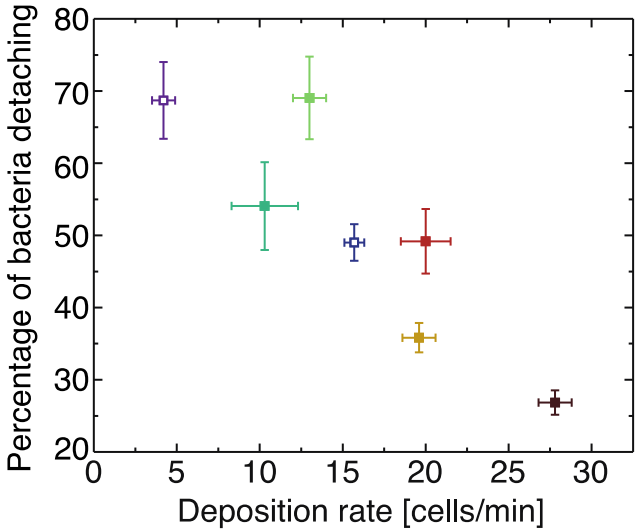

Figure 2.12. Percentage of bacteria that detach during each experiment as a function of deposition rate for a suspension flow rate of 1 mL/min. Error bars indicate standard deviation over three replicates. Colors correspond to those used in Figure 2.2. The total number of detaching bacteria analyzed for each replicate on each substrate was: APTES (N=315, 345, 352), ODMCS (N=321, 405, 435), APTMS (N=244, 282, 298), unmodified glass (N=230, 262 and 270), GPTS (N=296, 309, 316), OTS (N=187, 205, 218), and plasma-treated glass (N=90, 106, 158).

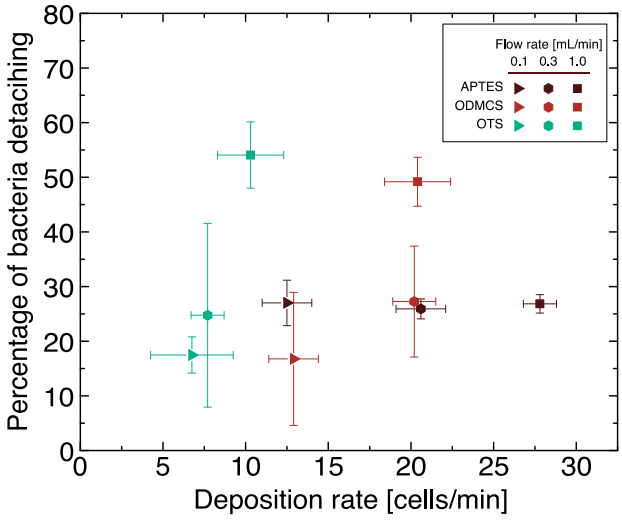

Figure 2.13. Percentage of bacteria that detach during the experiment as a function of deposition rate for three different surfaces (APTES, ODMCS, and OTS) and for three different suspension flow rates (0.1, 0.3, and 1.0 mL/min).

To attempt to distinguish between these explanations, we classified the attachment fate of bacteria that initially exhibited a large degree of motion and were presumably initially attached *via* the flagellum. We first subdivided each trajectory of length greater than twenty-four seconds into equal thirds. Bacteria whose trajectories in which the centroid of the bacterium underwent a large displacement (of greater than 0.12 microns) in the first third of the surface dwell time were classified as initially moving.

We subsequently determined the fate of each initially moving bacterium by searching its trajectory for large displacements in the remaining thirds. Trajectories that exhibited at least one large centroid displacement in each third were classified as moving; trajectories in which no large centroid displacements were seen in the last third were classified as converted to stationary (Figure 2.14). All other behavior was classified as intermediate. The percentage of initially moving bacteria whose fate is moving, stationary, or intermediate is shown as a function of deposition rate in Figure 2.15;

increased deposition rate was correlated with an increase in the percentage of bacteria that converted from moving to stationary over the duration of our experiments. Bacteria most readily became immobilized on the two cationic surfaces (APTES and APTMS) but remained motile on surfaces that resisted initial attachment (plasma-treated glass and OTS).

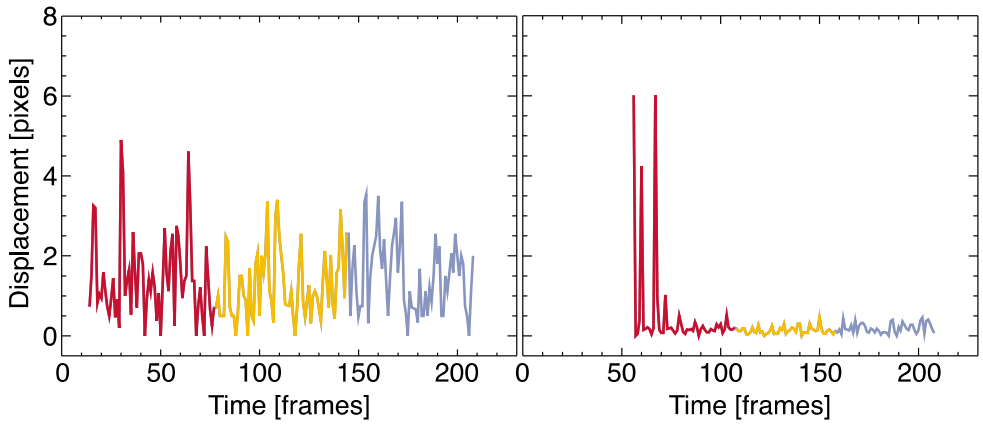

Figure 2.14. (Left) Representative trajectory for an initially mobile bacterium that remained mobile throughout the experiment; (right) representative trajectory for a bacterium that converted to stationary during the experiment. The cutoff for mobility, in units of the y-axis (pixels), was a displacement of one pixel.

Conversion to immobility depended less on flow rate than on surface chemistry (Figure 2.16). This result suggests that the fate of bacteria initially attached by the flagellum depends on the surface properties, with strong and short-ranged electrostatic interactions succeeding the apparently weaker initial attachment frequently mediated by flagella. This mechanism is complementary to the proposed role of flagella in adhesion at low ionic strengths, in which flagella allow bacteria to pierce an unfavorable energetic barrier near the surface.[32]

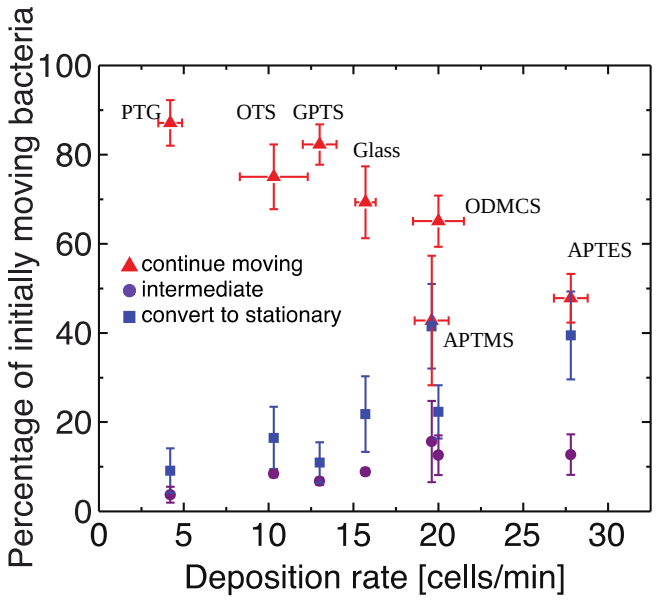

Figure 2.15. Percentage of initially moving bacteria that continue moving (red triangles), convert to stationary (blue squares), and exhibit an intermediate behavior (purple circles). Error bars indicate standard deviation over three replicates acquired at a suspension flow rate of 1 mL/min. The total number of initially moving bacteria analyzed for each replicate on each substrate was: APTES (N=108, 129, 138), ODMCS (N=145, 224 and 243), APTMS (N=106, 111, 124), unmodified glass (N=133, 139,176), GPTS (N=182, 206, 206), OTS (N=102, 132, 133), and plasma-treated glass (PTG) (N=52, 68, 80).

Our results indicate that the rate of deposition and the attachment fate of bacteria on surfaces depend on the surface chemistry. We found significantly less deposition on the OTS surface than on the ODMCS surface, although both surfaces were hydrophobic. OTS has a longer alkyl chain (18 carbons) than ODMCS (8 carbons); ellipsometry measurements on OTS and ODMCS layers on silicon substrates indicated that OTS formed a thicker layer (3.5 ± 0.3 nm) than ODMCS (1.43 ± 0.09 nm) (Table 2.5). We therefore posit that the longer OTS chain somewhat hindered bacteria from accessing the energetic minimum very close to the surface. Our results are consistent with earlier reports of reduced deposition of *E. coli* on OTS.[35, 71]

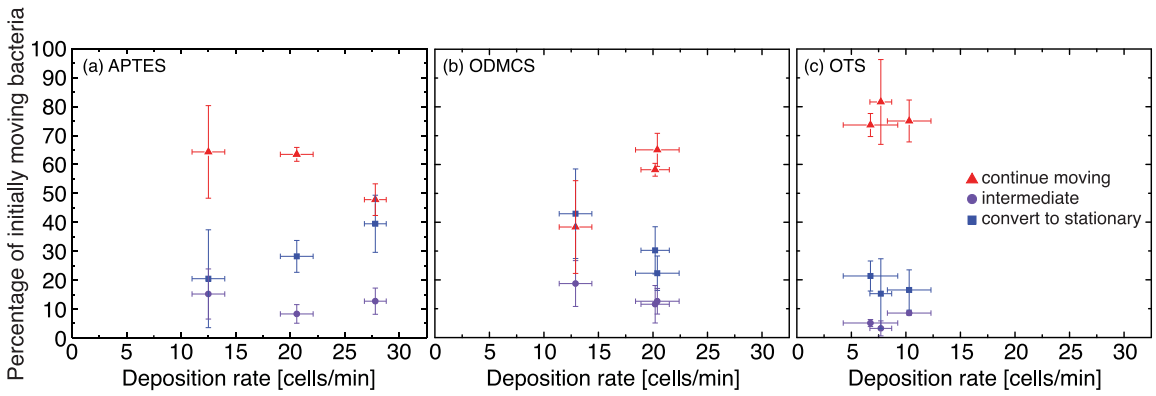

Figure 2.16. Fate of initially moving bacteria as a function of deposition rate on (a) APTES, (b) ODMCS, and (c) OTS at solution flow rates of 0.1, 0.3, and 1.0 mL/min (left to right in each panel).

Table 2.5. Thickness for silane layers deposited on Si-wafer measured using spectroscopic ellipsometry and fits generated using the Cauchy model considering a native oxide layer of 1 nm for each surface. All measurements were performed at an angle of 70°. Numbers in parentheses indicate standard deviation from three spot measurements

Substrate	Thickness [nm]
OTS	3.51 (0.27)
ODMCS	1.43 (0.09)
APTES	1.65 (0.31)
APMTS	2.46 (0.04)
GPTS	1.92 (0.02)

More surprisingly, we observed significantly different deposition rates on the cationic APTES and APTMS, which both bear aminopropyl functional groups and exhibit chemical differences only in the length of the side chains. To gain insight into the molecular-scale origins of the differences in deposition rates, we used XPS and ellipsometry to characterize the properties of these two surfaces.

2.3.3 Additional characterization of cationic substrates: XPS

We used X-ray photoelectron spectroscopy (XPS) to determine the elemental composition of the self-assembled monolayers on APTES and APTMS. Quantitation of the low-resolution spectra was performed using manufacturer-specified empirical sensitivity factors (C1s = 0.314, N1s= 0.499, O1s = 0.733 and Si2p = 0.368). The presence of nitrogen (N1s) peak on both the surfaces confirmed the successful deposition of the silanes (Figure 2.17).

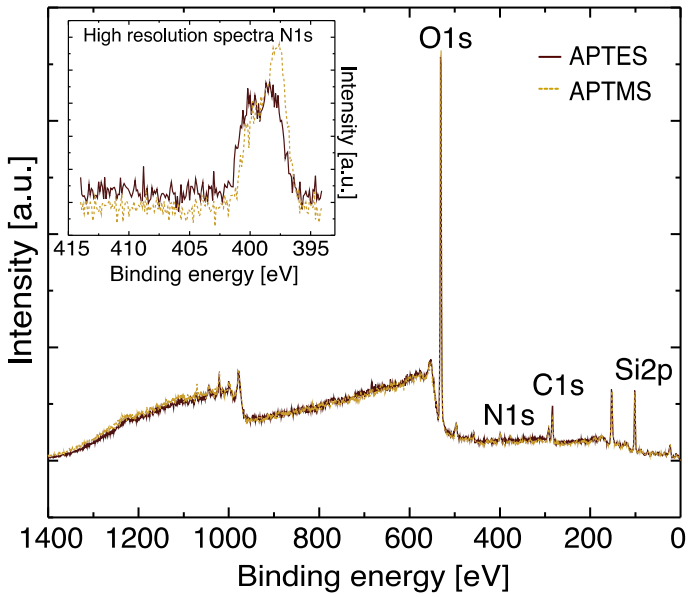

Figure 2.17. Overlaid XPS survey spectra for APTES (solid line) and APTMS (dashed-line) modified glass substrates. Inset: overlaid high-resolution spectra for N1s for each surface.

We found that the ratio of nitrogen to silicon (N/Si=0.1) was equal for both the silanized substrates. However, the ratio of carbon to nitrogen (C: N) was 7:1 for APTES and 4:1 for APTMS. APTES (APTMS) has three hydrolyzable ethoxy (methoxy) side groups that provide multiple sites for attaching to substrates and for polymerizing in the horizontal and/ or vertical directions. If each of the three ethoxy or methoxy group on the

APTES and APTMS, respectively, had reacted with silanol groups on the surface or each side chain were cross-linked with that of a neighboring molecule covalently bonded to the surface (giving a completely cured silane monolayer), the carbon to nitrogen ratio should be 3:1 for each monolayer. The higher ratio could be attributed to an incomplete reaction of the ethoxy and methoxy groups and hence was consistent with a difference in the degree of cross-linking of the side groups. The ratio of 7:1 on APTES was consistent with two unreacted ethoxy groups, whereas one unreacted methoxy group could generate the C:N ratio of 4:1 measured on APTMS. The orientation of the silane molecules and hence relative proximity of the reactive amine group to the surface was affected by the degree of cross linking achieved.[80]

We also obtained high-resolution N1s spectra (shown in the inset to Figure 2.17) for each substrate. Gaussian curve fitting (using MultiPak) revealed the presence of two peaks. The peak at 399.6 ± 0.6 eV could be assigned to the free amine while the one at 401.5 ± 0.5 eV could be assigned to protonated and hydrogen bonded amines.[81] The contributions from the protonated and hydrogen bonded amine for APTES and APTMS were 40.1% and 36.4%, respectively.

We additionally obtained high-resolution XPS spectra for C and Si. Because the Si 2p binding energy is sensitive to the number of O atoms bonded to Si, we were able to distinguish between Si from the silane and that from the underlying substrate using the peak fitting method described by Hare *et al.*[82] Gaussian curve fitting (using MultiPak) on high-resolution XPS spectra (Figure 2.18) for each substrate revealed the presence of two peaks.

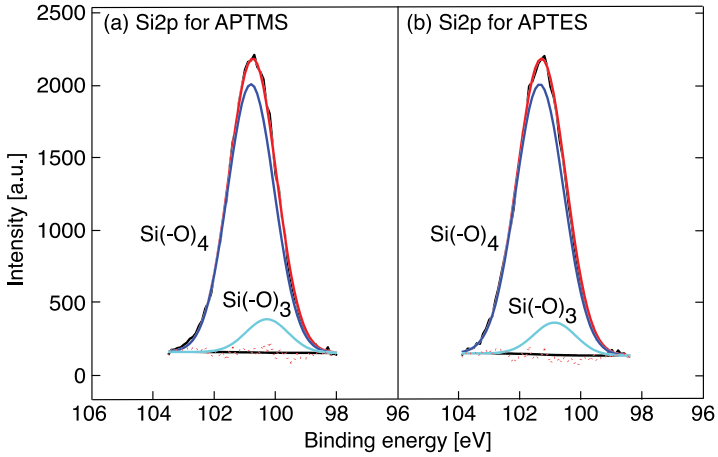

Figure 2.18. High-resolution spectrum for Si2p (black) with core level peaks fitted corresponding to $Si(-O)_4$ (dark blue) and $Si(-O)_3$ (light blue) for (a) APTMS and (b) APTES surfaces.

The peak close to 101 ± 0.2 eV could be assigned to the $Si(-O)_4$ component coming from Si bonded to oxygen within the substrate. The peak at 100.4 ± 0.1 eV could be assigned to the $Si(-O)_3$ component peak, which is the contribution from the Si in the silane (APTES or APTMS) covalently bonded to the substrate. The atomic composition of Si from the film was therefore computed as a relative atomic percentage:

$$\%\mathrm{Si}_{\mathrm{silane}} = \%\mathrm{Si}\frac{A_{\mathrm{Si(-O)_3}}}{A_{\mathrm{Si_{2p}}}}, \tag{2.9}$$

where %Si is the atomic percent of Si, $A_{Si(-O)3}$ is the area of the component peak, and A_{Si2p} is the area of the entire Si_{2p} peak.

Assuming the silane films on our substrate to be self-assembled monolayers, we estimated the surface density of the silane molecules using the relative atomic percentage calculated from XPS data as

$$\sigma_{\mathrm{monolayer}} = \frac{A_{\mathrm{Si(-O)_3}}}{A_{\mathrm{Si_{2p}}}} n_{\mathrm{SiO_2}} z, \tag{2.10}$$

where n_{SiO_2} is the molecular concentration of silica (estimated as 22 SiO_2 molecules/nm^3, based on the density of thermal silica[83]) and z is the depth of analysis. The average inelastic mean free path (λ) for Si was taken as 1 nm and hence z was taken as 2.1 nm ($3\lambda\sin45°$). Based on relative area fractions obtained from peak fitting of high resolution scan for Si2p XPS data, the surface coverage was calculated as 4.3 molecules/nm^2 and 4.8 molecules/nm^2 for APTES and APTMS, respectively.

We also used a method described by Bramblett *et al.*[84] to estimate the surface density of silanes as

$$\sigma_{\text{monolayer}} = \frac{t\rho N_{AV}}{M_w}, \tag{2.11}$$

where t is the film thickness, ρ the density of silane (1.03 g/cm^3, for APTMS and 0.946 g/cm^3 for APTES), N_{AV} is Avogadro's number, and M_W is the molecular weight of the silane (APTES: 221.37 g/mol and APTMS: 179.29 g/mol). Assuming monolayers 0.6 nm thick, the surface density was estimated as 1.5 molecules/nm^2 and 2.1 molecules/nm^2 for APTES and APTMS, respectively. This result and the previous result suggested that the surface density did not significantly vary between the two surfaces. The ratio of C:N on APTES (7:1) was greater than that for APTMS (4:1); if the silane layer were completely cured, then the C:N ratio should be 3:1 for each monolayer. The variation from the ideal C:N ratio suggested that APTMS layers were more crosslinked than APTES layers, which may affect the orientation of the molecules.[80]

Because our silanes were deposited onto glass, we were not able to directly characterize their thickness using spectroscopic ellipsometry. Instead, we deposited silanes on silicon wafers using the same protocol as was used for glass and measured the thickness using a spectroscopic ellipsometer (J.A. Woolam M-2000). The thicknesses of

APTES and APTMS layers deposited on Si wafer were 1.7 ± 0.3 nm and 2.46 ± 0.04 nm, respectively, consistent with an APTMS multilayer. The ellipsometry measurements support the XPS results and indicate that there are molecular-scale differences between the APTES and APTMS layers. These measurements suggest that the differences in the deposition rate may arise from differences in the arrangement (structure, orientation, and layer thickness) of the silane molecules.

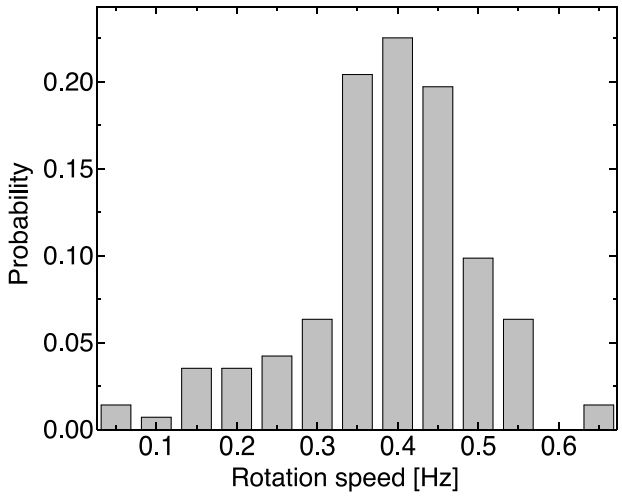

Figure 2.19. Distribution of rotation speed for a representative single bacterium tethered to an OTS surface by its flagellum and steadily rotating.

2.4 Conclusions

We investigated the transition from transient to irreversible attachment of *E. coli* bacteria deposited onto surfaces coated with self-assembled silanes. By analyzing the trajectories of hundreds of bacteria on each surface, we found that the rate at which bacteria were deposited varied non-monotonically with surface wettability and energy. Instead, we found that deposition rate was inversely correlated with the degree of surface-

attached flagella-driven motion. For a given flow rate, bacteria less readily detached and more readily became immobilized on the surfaces onto which they most rapidly deposited. We posit that flagella enable bacteria to transiently attach to surfaces; the fate of transiently attached bacteria, however, is ultimately determined by physicochemical interactions (electrostatic or van der Waals) between bacteria and surfaces. Because the transition from transient to immobilized attachment was also correlated with short-time deposition rate, our results suggest that initial transient surface motility may serve as a metric to rapidly determine the efficacy of surfaces to reduce fouling by bacteria and thereby speed the design of improved antifouling materials for medical, technological, and environmental settings.

These initial results suggest multiple pathways for future studies. First, we examined only the initial rate of deposition of bacteria over relatively short times; as bacteria continue to attach over long time scales we expect that that interactions between bacteria may influence the deposition rate and the transition to irreversible attachment (as suggested by Figure 2.15). Experiments to correlate initial motion to long-time deposition are required to establish the predictive power of the correlations that we identify here. Second, we showed that our motility metric inversely correlates with deposition rate across multiple flow rates. Variations in detachment rates, however, suggests that bacteria may use different shear-rate dependent attachment mechanisms on surfaces of different properties; this idea is consistent with earlier experiments on *E. coli* that suggest that the role of flagella in initial attachment changes as the flow rate is increased[85]. Future experiments using motility- and appendage- or adhesin-deficient mutants will provide further insight into the roles of motility on initial attachment. Finally, we examined only

one strain of *E. coli*. Bacteria that readily form biofilms, such as the opportunistic Gram-negative pathogen *Pseudomonas aeruginosa*, release extracellular polymeric substances (EPS) that modify the surface properties and facilitate initial adhesion and attachment[86] and microcolony formation.[30] Experiments in biofilm-forming strains may therefore provide insight into the role of EPS in the transition from transient to irreversible attachment. We expect that applying our high-throughput methods to analyze bacterial trajectories in these different scenarios will provide additional insight into the role of bacterial, surface, and fluid conditions on the transition to irreversible adhesion.

Note: The material presented in this Chapter has been published in Langmuir.

Sharma, S.; Conrad, J. C. Attachment from Flow of *Escherichia Coli* Bacteria onto Silanized Glass Substrates. *Langmuir* **2014**, *30,* 11147-11155.

The introduction has been summarized to avoid redundancy with Chapter 1. References, Figure number and Table numbers and their order of appearance have changed with the incorporation of article supporting material in the chapter and also for dissertation consistency.

Chapter 3 Sub-nanometric roughness affects the deposition and mobile adhesion of *E. coli* on silanized glass surfaces

3.1 Introduction

Adhesion of bacteria to a surface represents the first step in the formation of biofilms. These organized and stress-resistant bacterial communities have significant negative impacts in industry, fouling industrial pipelines,[87] ship hulls,[88] and food processing equipment.[89] Moreover, biofilms foul biomedical devices implanted in the human body,[57] leading to significant costs associated with hospital-acquired infections, and cause or exacerbate diseases in cystic fibrosis[90] and other immunocompromised patients.[91, 92] Conversely, biofilm formation aids certain beneficial processes; for example, bacteria can remove harmful contaminants in water purification[11, 14] and environmental pollutants in bioremediation.[12, 13] For both deleterious and beneficial applications, controlling biofilm formation on surfaces is hence an important goal. Improving the design of materials and strategies towards this goal, in turn, requires understanding the factors that affect the initial attachment of bacteria.

First, bacterial adhesion is mediated by physicochemical interactions, including non-specific van der Waals, electrostatic, and acid-base interactions between the substrate and bacterium.[93, 94] Receptors on the surface of bacteria can specifically interact with particular ligands on the substrate.[60, 95] Furthermore, molecules termed adhesins that are present on the cell surface affect bacterial adhesion by complex interaction mechanisms that are yet to be unraveled.[96, 97] Thus, the total interaction is influenced by surface properties of bacteria and of substrates. Substrates with amine or aliphatic functional groups typically show higher bacterial deposition than hydroxylic substrates.[41, 98] Most

bacteria are negatively charged above their isoelectric point;[99] hence bacteria are electrostatically attracted by cationic surfaces[100, 101] and repelled by anionic ones.[102] Surface wettability also affects bacterial adhesion. The affinity of bacteria for hydrophobic substrates, for example, is thought to arise from the lower surface energy of bacteria compared to that of the suspending liquid.[17, 103] Nonetheless, the role of wettability in cell adhesion is not straightforward: depending on chemistry and cell type, hydrophilic surfaces are reported to exhibit either lower[42, 104, 105] or equal[106] numbers of adherent cells compared to hydrophobic surfaces. Finally, superhydrophobic surfaces can have very low bacterial adhesion, as these surfaces exhibit low wettability on short time scales.[25, 107]

Second, roughness of the substrate affects bacterial attachment. At the microscale, increased roughness typically increases the rates at which bacteria attach and grow.[107, 108] This enhancement may arise in part from geometry: bacteria adhering to an irregular substratum may be able to fit into microscale surface features that are comparable to their size, thereby protecting themselves from unfavorable environmental factors.[109] At the nanoscale, increased roughness is often correlated to enhanced bacterial attachment for a variety of species, including *Staphyloccocus aureus*,[44, 110] *Pseudomonas aeruginosa*,[44, 111] and *Escherichia coli*.[110] Other studies, however, report decreasing attachment with nanoscale roughness – for example, for *Pseudoalteromonas issachenkonii* KMM 3549^{T}.[112] At length scales smaller than 1 nm, very smooth surfaces are thought to inhibit adhesion; few studies address the effect of sub-nanometric roughness (root-mean-square (RMS) roughness of < 1 nm) on bacterial attachment. Again, different studies report varying effects of roughness, depending on chemistry and species – increasing sub-nm-

scale roughness on polyurethane reduced attachment of several bacterial species (*Staphylococcus epidermidis, E. coli,* and *Proteus mirabilis*),[113] whereas increasing sub-nm-scale roughness on titanium did not affect adhesion of *P. aeruginosa,* but reduced adhesion of *S. aureus*.[114]

Third, hydrodynamic shear forces acting on bacteria in flow conditions affect adhesion. The best-known example of a stress-dependent interaction is the formation of (specific) catch-bonds between the bacteria type I fimbriae adhesin and surface-attached mannose.[60] The increase in strength of the mannose-fimbriae bond with shear stress led to increased long-duration adhesion. Furthermore, this specific interaction generated dynamic "stick-and-roll" translational motion of bacteria on mannose- and oligomannose-covered substrates.[60, 115, 116] Other species also exhibit stress-dependent adhesion, but the mechanisms that mediate these interactions are not known. As one example, shear increased the residence time of *P. aeruginosa* on abiotic surfaces; this interaction did not depend on the substrate and was not mediated by type I pili, type IV pili, flagella, or the extracellular matrix.[117] Even if bacteria do not adhere irreversibly, flow-dependent interactions can give rise to transient or mobile adhesion, which manifests in *S. epidermidis bacteria* flowed in close proximity with a substrate as surface-associated sliding.[106] This state subsequently transitions over time into immobile adhesion through development of frictional forces,[98] which are thought to be influenced by local heterogeneities of both substrate and bacterium.[118]

Finally, the interplay between these different factors (surface chemistry, bacterial surface structures, roughness, and flow) can interact to modulate attachment. For example, substratum wettability depends not only on the exposed functional groups but

also on topography.[119] Similarly, the ability of bacteria to attach under flow may be enhanced by roughness-induced frictional interactions that generate effective tangential forces.[98] The flow-driven appearance of transient motility behaviors such as stick-and-roll or mobile adhesion suggests that both surface properties and flow affect the dynamics of attachment; most extant studies, however, quantify attachment only through cell surface density and not through dynamic measurements of bacteria on surfaces. Hence there is a need for studies that address the interplay of these competing factors on bacterial attachment and on mobile adhesion.

Here, we show that sub-nanoscale roughness affects the deposition and transient near-surface motility of *E. coli*. We create model substrates of controlled chemical functionality by assembling layers of organosilanes bearing one of two different terminal functionalities (CH_3- and CF_3-) on glass coverslips and characterize the physicochemical properties of the surfaces. Using confocal imaging and high-throughput tracking algorithms, we quantify the motion of bacteria deposited onto these surfaces from flow. We find that the rate at which bacteria deposit onto a surface generally decreases as the shear stress is increased, and cannot be predicted based on extended DLVO calculations. Instead, for a fixed shear stress the deposition rate systematically increases as the surface RMS roughness increases, independent of chemical terminal functionality. Similarly, the extent to which surface-tethered cells are able to flip and rotate decreases with RMS roughness, consistent with the increased deposition.[120] Finally, we report here mobile adhesion of *E. coli*, in which cells undergo long linear displacements while located very close to a surface. This behavior occurs in the presence and absence of flagella, suggesting that it is not actively driven. Mobile adhesion depends more strongly on

surface roughness than on surface chemistry, appearing on very smooth surfaces of both terminal functionalities, and vanishes when cells express fimbriae. Because mobile adhesion occurs only in the absence of the Velcro-like fimbriae and on very smooth surfaces, we suggest that this behavior occurs only when frictional interactions between the body of a bacteria and the surface are very low. Together, these results suggest that that even sub-nm scale roughness affects both transient and irreversible cell adhesion. Hence reducing nanoscale roughness, whether on the cell surface (by inhibiting expression of fimbriae[121]) or on the substrate, may help to control initial fouling of surfaces by bacteria.

3.2 Experimental Section

3.2.1 Bacterial strains and plasmids

All strains and plasmids used in the study are summarized in Table 3.1. For shear-rate dependent experiments we used *Escherichia coli* strain MC1061. To test the effect of bacterial surface structures on deposition we used *E. coli* strain BW25113 and two isogenic knockout mutants, JW4277 (Δ*fimA*) and JW1908 (Δ*fliC*)[122], that lack the ability to synthesize fimbriae and flagella, respectively. Plasmid pFG10 conferring constitutive expression of enhanced green fluorescence protein (GFP) and chloramphenicol resistance was introduced into all strains by electroporation. Use of this plasmid allowed cells to be visualized under fluorescence without external labeling. Plasmid pPCC1401 was constructed by cloning the entire *E. coli* MG1655 *fim* operon (genes *fimAICDFGH* were PCR-amplified from genomic DNA) downstream of the *Ptac* promoter (inducible with isopropyl-β-D-1-thiogalactopyranoside (IPTG)) in plasmid pFG1[123] (thus replacing the *araC* gene in pFG1). To test the effect of fimbriae overexpression, strain MG1655Δ*fimA*

deficient in fimbriae production (a gift of Prof. Debora Rodrigues, University of Houston) was transformed with plasmid pPCC1401. This transformation resulted in strain "MG1655-pPCC1401," which overexpresses fimbriae upon induction with IPTG.

Table 3.1. *E. coli* bacteria strains used in this study

Strain (genetic mutation, function)	**Plasmid**	**Culture protocol**	**Experiments**
MC1061	pFG10 (constitutive GFP expression, chloramphenicol resistance)	LB with 30 µg/ml chloramphenicol and 200 rpm shaking at 37°C for 17 h	Flow experiments on all silanized surfaces at three shear stresses (3, 22, 67 mPa)
BW25113	pFG10	LB with 30 µg/ml chloramphenicol and 1 mM IPTG, 200 rpm shaking at 30°C for 17 h	Flow experiments on DTS at a single shear stress of 22 mPa
JW1908 (Δ*fliC*, deficient in flagella production)	pFG10	LB with 30 µg/ml chloramphenicol and 1 mM IPTG, 200 rpm shaking at 30°C for 17 h	Flow experiments on DTS at a single shear stress of 22 mPa
JW4277 (Δ*fimA*, deficient in fimbriae production)	pFG10	LB with 30 µg/ml chloramphenicol and 1 mM IPTG, 200 rpm shaking at 30°C for 17 h	Flow experiments on DTS at a single shear stress of 22 mPa
MG1655Δ*fimA* (deficient in fimbriae production)	-	LB with 200 rpm shaking at 30°C for 17 h	Flow experiments on DTS at a single shear stress of 22 mPa
MG1655-pPCC1401 (MG1655Δ*fim A* transformed with pPCC1401)	pPCC1401 (contains IPTG-inducible fim operon and apramycin resistance)	LB with 50 µg/ml apramycin at 37°C for 17 h followed by 2 h incubation with 1 mM IPTG	Flow experiments on DTS at a single shear stress of 22 mPa

3.2.2 Bacterial culture

Bacteria were streaked on Luria Bertani (LB)-agar plates (5 g yeast extract, 5 g NaCl, 10 g of Bacto-tryptone, 15 g agar, all from BD Chemicals) containing appropriate antibiotic and incubated overnight at 37°C (Nuvaire Inc.). Single colonies from the plate were inoculated into sterile LB medium (5 g yeast extract, 5 g NaCl and 10 g tryptone per 1 liter medium, BD Chemicals) and incubated in an orbital incubator shaker (New Brunswick Scientific) at 200 rpm and 37°C (for MC1061 and MG1655Δ*fimA*) and 30°C (for BW25113, JW4277, and JW1908) for approximately 16 – 17 hours. For MC1061, 30 µg/ml chloramphenicol was used in agar plates and cultures. For BW25113, JW4277 and JW1908, 30 µg/ml chloramphenicol and 1mM IPTG was added to both agar plates and liquid cultures. MG1655Δ*fimA* was grown in LB without any antibiotic. MG1655-pPCC1401 was grown in the presence of apramycin (50 µg/ml) on agar and without shaking in LB for 17 hours followed by induction with 1mM IPTG for two hours before harvesting the cells. A dense cell pellet was obtained by centrifuging the cells at 5000g in a Sorvall ST 16 Centrifuge (Thermo Fisher Scientific). After pelleting, the cells were re-suspended in 0.9% NaCl solution (ionic strength 154 mM). Cells were washed two times in NaCl by repeated mixing, centrifuging, and re-suspension to remove the growth medium. Pellet washing was limited to one centrifuge cycle for the hyperfimbriated MG1655-pPCC1401. Finally, for all imaging experiments, cells were suspended in 154 mM NaCl and diluted to an OD600 of 0.45 measured using a micro-plate reader (Infinte200 Pro, Tecan). The harvested cells were in the late stationary stage of growth based on growth curves measurement done for each strain.

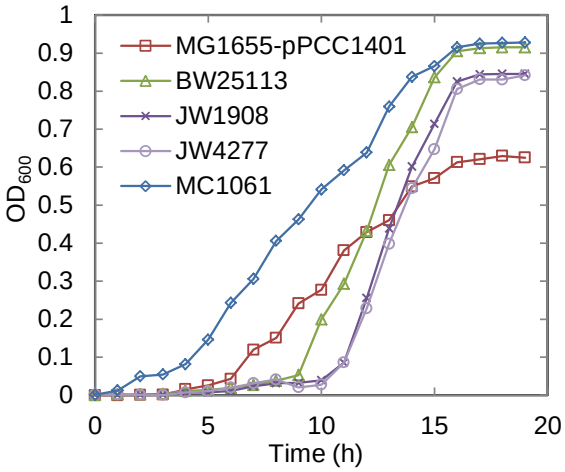

Figure 3.1. Growth curves of *E. coli* bacteria strains used in this study.

3.2.3 Microbial adhesion to hydrocarbons test (MATH) and bacterial electrophoretic mobility

The relative hydrophobicity of the cells was measured using the MATH test with *n*-dodecane and hexadecane.[64] All cells were hydrophilic and minimally adhered to hydrocarbons, as shown in Table 3.2. Zeta potentials for the *E. coli* strains in 154 mM NaCl were measured using a NanoBrook ZetaPALs (Brookhaven Instruments) ζ-potential analyzer. All cells were negatively charged under the experimental conditions used in flow studies.

Table 3.2. Relative hydrophobicity and zeta potentials for the bacterial strains used in this study. Numbers in parentheses correspond to the standard deviation over at least three replicate measurements

Strain	**% hydrophobicity (Std. deviation)**		**Zeta potential [mV] (Std. deviation)**
	n-dodecane	hexadecane	
MC1061	9 (1)	7 (4)	-23 (2)
BW25113 (wild type)	3 (1)	3 (1)	-20 (4)
JW4277 (Δ*fimA*)	4 (2)	5 (2)	-19 (4)
JW1908 (Δ*fliC*)	7 (3)	3 (3)	-17 (3)

3.2.4 Flagellar expression

The expression of flagella for MC1061, BW25113 and JW4277 strains (or absence of flagella in JW1908) was confirmed by a bacteria motility assay[124] (on a 0.3% agar plate) and by microscopic observation of swimming motility (or lack of swimming motility).

3.2.5 Fimbrial expression

The expression of fimbriae in all bacterial strains used in this study was tested using a fluorescence antibody conjugation assay using PAb49 (courtesy of Prof. Evgeni Sokurenko and Prof. Wendy Thomas, University of Washington) and Alexa Fluor® 568 conjugated secondary antibody (Thermo Fisher Scientific) and confocal microscopy (Figure 3.2). Bacterial suspensions were prepared following the same protocols used in the deposition experiments. 50 µL of the sample suspension was mixed with pAB49 (the anti-*fimA* antibody derived from rabbit serum),[125] which attached to any type1 fimbriae that were present on the cells. After 10 – 15 minutes, 10 µL of 0.2 mg/mL AlexaFluor568 conjugated, goat-derived anti-rabbit IgG secondary antibody was added and allowed to (react in the dark for 10 minutes) bind to PAb49. Labeled fimbriae were visualized using confocal microscopy (VTEye, Visitech) equipped with a laser excitation source of wavelength 561 nm. Images were acquired at 100× magnification. We observed fimbriae expression only in strain MG1655-pPCC1401 (Figure 3.1), which was engineered to express fimbriae when induced with IPTG. No fimbriae expression was seen on any of the other bacteria strains under the culture conditions used in the deposition experiments.

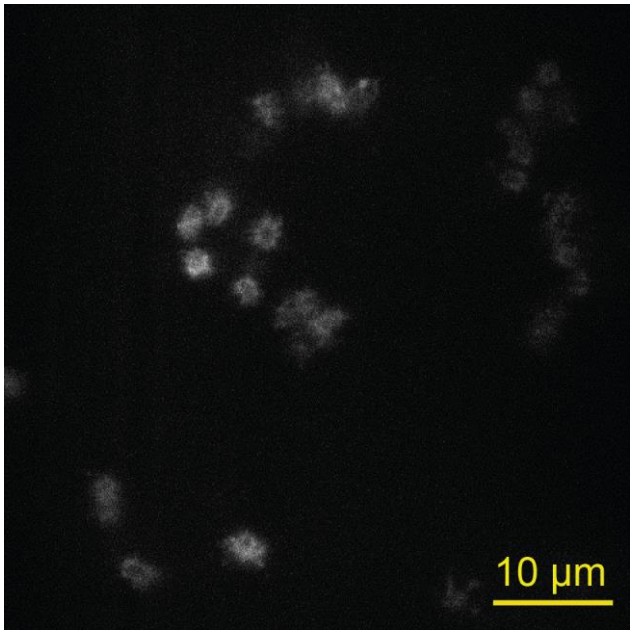

Figure 3.2. Confocal micrograph of MG1655-pPCC1401, showing bristle brush type expression of fimbriae on the cell surface.

3.2.6 Transmission electron microscopy (TEM) imaging of bacteria

TEM imaging of all bacterial strains was used to visualize expression of two bacterial appendages, flagella and fimbriae. For all strains except MG1655-pPCC1401, cell suspensions for imaging were prepared following the same protocol used for flow experiments. For imaging, 2 – 5 µL of bacterial suspension was adsorbed onto a freshly glow-discharged carbon-coated grid (PELCO ®). The sample grid was washed gently with water and stained with 2% (w/v) uranyl acetate. Imaging was done using a JEOL 1200 EX TEM operated at an acceleration voltage of 100 kV. Electron micrographs were recorded at calibrated magnifications using a 3k slow-scan CCD camera (model 15C, SIA) and are shown in Figure 3.2. Flagella expression was observed in all strains except JW1908, which is a flagella-deficient mutant of BW25113. Fimbriae were observed only

for MG1655-pPCC1401 strain grown in static conditions with IPTG induction. All other strains did not express fimbriae.

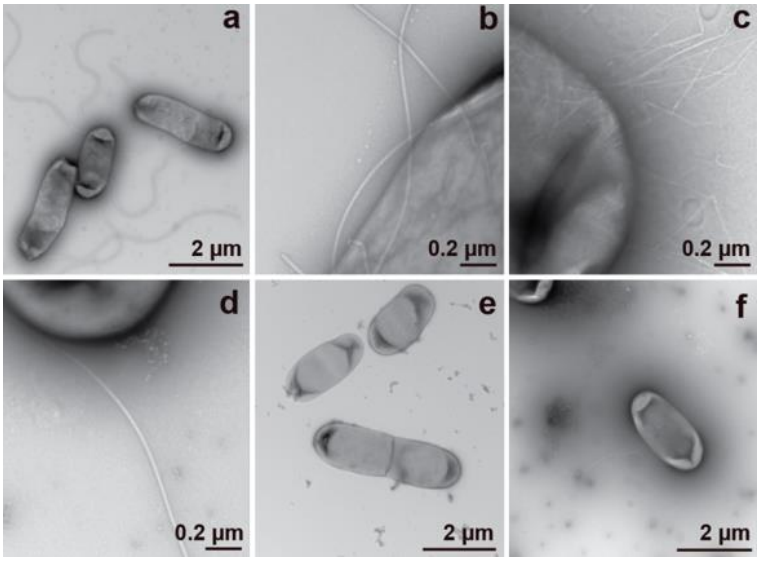

Figure 3.3. TEM micrographs for bacterial strains (a) MC1061, showing flagella and absence of fimbriae expression; (b) MG1655Δ*fimA*, showing presence of flagella but not fimbriae; (c) MG1655-pPCC1401, showing fimbriae expression; (d) BW25113, showing flagella and absence of fimbriae expression; (e) JW1908, showing absence of both flagella and fimbriae; (f) JW4277, showing presence of flagella.

3.2.7 Substrate preparation

To prepare the test substrates for flow experiments, we used silanes bearing one of two different terminal surface chemistries, CH_3- or CF_3-, and varied the C-chain length from 3 to 18 or from 3 to 10 C, respectively (Figure 3.4). All organosilanes were purchased from Gelest and were deposited from solution onto glass coverslips. Prior to deposition, coverslips of dimension 48 × 65 mm^2 (thickness 0.13 – 0.17, Gold Seal) were cleaned by sonication in acetone (Macron, AR grade) followed by de-ionized (DI) water (resistivity 18.2 MΩ·cm, Millipore water purification system), dried under nitrogen, and

then exposed to air plasma (Harrick Plasma) for two minutes. To deposit 1H,1H,2H,2H-perfluorodecyltrichlorosilane (FDTS) and 3,3,3-trifluoropropyltrichlorosilane (FPTS), plasma-treated glass slides were immersed in iso-octane (Sigma Aldrich) for ten minutes and then transferred to a 1 mM solution of either FDTS or FPTS in iso-octane that had been mixed by sonication for five minutes. After allowing deposition to proceed for ten minutes, the slides were successively rinsed with iso-octane, isopropanol, and DI water. To deposit octadecyltrichlorosilane (OTS), n-decyltrichlorosilane (DTS), and propyltrichlorosilane (PTS), slides were immersed in a 1 mM solution of OTS, DTS or PTS in hexane (Sigma Aldrich) for two hours. Slides were then sonicated successively in chloroform (Sigma Aldrich), acetone (Macron), and DI water for two minutes each. After deposition and rinsing, all surfaces were dried under nitrogen and then baked at 110°C. Silanized substrates were placed in petri dishes, sealed with Parafilm, and stored in a desiccator for no more than one day before use in flow experiments.

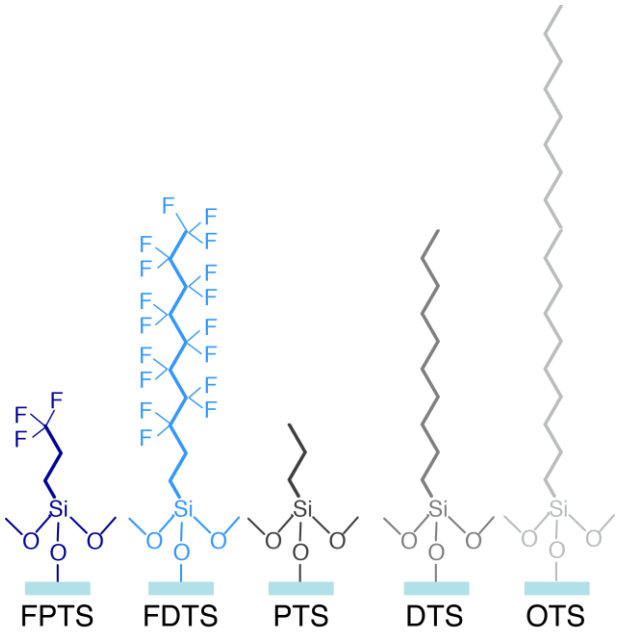

Figure 3.4. Chemical structures of the organosilanes used to create glass surfaces of controlled chemistry used in this study.[126]

3.2.8 Surface characterization

Water contact angles for each silanized surface were measured using a Dataphysics OCA 15EC goniometer. Contact angles for two other test liquids, ethylene glycol (99%, Alfa Aesar) and diiodomethane (99%, Alfa Aesar), were measured for each surface and the surface energy was calculated using the method of van Oss.[127] Thickness of silane layers was estimated by measuring the thickness for equivalent silane depositions made on Si-wafer using spectroscopic ellipsometry (M-2000, J.A. Woolam). All measurements were performed at an angle of 70°. The reported data correspond to at least five spot measurements made on three samples.

To characterize the zeta potentials of silanized surfaces, silanes were deposited on silica nanoparticles (diameter of 170 nm) following the protocols given earlier for surfaces. The zeta potentials of the silanized nanoparticles suspended in 154 mM NaCl was measured using a NanoBrook ZetaPALs (Brookhaven Instruments) ζ-potential analyzer.

Atomic force microscopy (AFM; Nanoscope IV, Digital instruments) was used to measure the surface roughness of silanized glass surfaces. In a typical experiment, a 4 μm^2 area was scanned at 2 Hz in tapping mode in air using an n-type silicon cantilever (μMasch, resonance frequency = 320 kHz, force constant = 40 N/m). AFM images were analyzed using NanoScope 6.13R1 software to calculate roughness parameters.

3.2.8.1 XPS characterization of silanized substrates

The presence of chemical groups expected for self-assembled layers of silanes on glass was confirmed using X-ray photoelectron spectroscopy (Physical Electronics Model

5700) using Al Kα X-ray source (1486.6 eV) under ultrahigh vacuum. The takeoff angle was 45° and the analyzer spot diameter was 800 μm. Survey and high-resolution spectra were recorded at pass energies of 187.85 and 23.5 eV, respectively. The binding energy scales were referenced to 284.6 eV, corresponding to the maximum intensity for a C 1s spectrum. Spectral analysis and peak fitting was performed using the Multipak software package (Multipak V5.0A, Physical Electronics, Inc.). Atomic compositions were estimated from the high-resolution scans. Fluorination of the glass slides treated with FDTS and FPTS was confirmed by the presence of F1s peak at around 688.7 eV, as shown in the survey spectra (Figure 3.5).

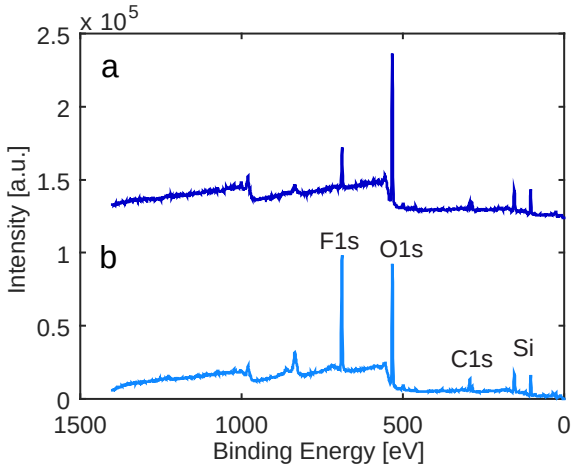

Figure 3.5. XPS survey spectra of (a) FPTS and (b) FDTS surfaces. The distinct F1s peak at 688.7 eV confirms the attachment of the fluorinated silanes

The chemical compositions of the fluorinated substrates were calculated from the high-resolution spectra and reported in Table 3.3. No peaks related to the chlorine species appeared in any spectrum, confirming that the trichlorosilane groups of the silanes reacted completely with the hydroxyl groups on the glass substrate.[128] The measured F/C

mass ratio is 1.28 and 0.49 for FDTS and FPTS, respectively. These ratios are different from the ideal values for a single monolayer; we attributed this difference to presence of additional C expected from exposure of surfaces to air.

Table 3.3. Percentage atomic composition determined by XPS high-resolution spectra for the fluorinated surfaces

Substrate	C1s	O1s	F1s	Si2p	K2p
FPTS	17.83	48.18	8.82	23.24	1.92
FDTS	18.78	35.70	24.10	18.14	3.27

The survey spectra for the alkylsilane surfaces are presented in Figure 3.6. Again, no peaks related to the chlorine species appeared in any spectrum, confirming that the trichlorosilane groups of the silanes reacted completely with the hydroxyl groups on the glass substrate. High-resolution spectra were acquired for C1s, O1s, and Si2p, and were used to calculate the chemical composition of the surfaces (Table 3.4).

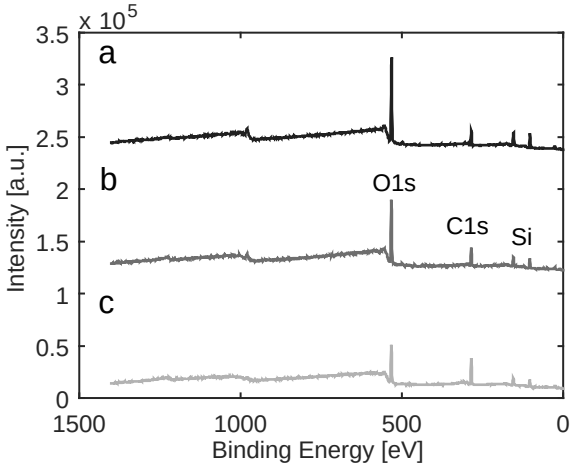

Figure 3.6. XPS survey spectra of the methyl-terminated silanized surfaces: (a) PTS (b) DTS and (c) OTS. The C1s peaks at 284.6 eV reflect contributions of attached alkylchlorosilanes

Table 3.4. Atomic composition determined by XPS high-resolution spectra for the methyl-terminated surfaces

Substrate	C1s	O1s	Si2p
PTS	19.01	55.52	25.47
DTS	30.96	43.21	25.83
OTS	55.89	29.01	15.10

3.2.9 Flow experiments

Suspensions of cells were flowed through a linear channel using a syringe pump (Model 11, Harvard Apparatus) at applied flow rates of Q = 7.5, 60, and 180 mL/h. The shear stress at the wall was $\sigma = 3Q\mu/2Wb^2$, where μ is the viscosity of water (0.89 mPa-s) and W = 4 mm and $2b$ = 1 mm are the width and height, respectively, of the flow channel; in these experiments σ varied from 3 – 67 mPa (1 mPa = 1 pN/μm^2). Cells containing the fluorescent plasmid (pFG10) that were deposited on the surfaces during flow were imaged using a confocal fluorescence scanner (VT Infinity, Visitech) attached to a Leica DM4000 inverted microscope that was equipped with a 100x oil immersion lens (HCX PL APO of numerical aperture 1.4). A laser excitation source with an excitation wavelength λ = 488 nm was used to excite the constitutively-expressed GFP in the cells. One image with an exposure time of 0.3 s and a pixel size of 0.125 ± 0.0006 μm was acquired every three seconds using an ORCA 200 camera (Hamamatsu) that was controlled by Voxcell Scan software (Visitech). In a typical flow experiment, 300 images with an area of 84 × 64 μm^2 (corresponding to 672 pixels × 512 pixels) were acquired over a total time of 15 minutes. Experiments on each silanized surface were performed in triplicate on at least two different surfaces with at least two different bacteria cultures. For experiments involving MG1655Δ*fimA*, which did not contain the fluorescent plasmid, bacteria were imaged using brightfield microscopy and an Olympus DP21 camera. For

experiments involving the hyperfimbriated strain MG1655-pPCC1401, cells were imaged with brightfield microscopy (using non-labeled cells) and with confocal fluorescence scanning (using cells labeled with 300 mM Syto® 9 nucleic acid stain (ThermoFisher)).

3.2.9.1 Hydrodynamic force for particle touching a surface

The hydrodynamic drag force is calculated from the equation given by O'Neil[129] and shown in Table 3.5.

Table 3.5. Hydrodynamic force calculations considering the bacteria as a sphere of equivalent volume

Q (m^3/s)	$\boldsymbol{V_R}$ (m/s)	$\boldsymbol{F_h}$ (N)
2.1×10^{-9}	2.2×10^{-6}	4.4×10^{-14}
1.7×10^{-8}	1.8×10^{-5}	3.5×10^{-13}
5.0×10^{-8}	5.3×10^{-5}	1.1×10^{-12}

In this table, V_R is the fluid velocity at center of the particle and F_h is the hydrodynamic drag force.

3.2.10 Image analysis

Algorithms written in IDL (Exelis VIS)[54] were used to locate and track single cells in a time series of microscopy images. Additional analyses of cell attachment and detachment rates, speed, and residence time of cells in mobile adhesion was performed using routines written in Matlab (MathWorks) and in IDL.

3.3 Results and Discussion

3.3.1 Surface characterization

To generate well-characterized surfaces for bacterial adhesion experiments, we deposit silanes of two different terminal functionalities (CH_3- or CF_3-) and lengths of the carbon (C)-chain (3, 10, and 18). We measure the water contact angle (WCA), surface energy, thickness, and zeta potential of the different surfaces, as summarized in Table 2.4. All surfaces except FPTS are hydrophobic, as assessed from the water contact angle, and exhibit thicknesses that are consistent with multilayer formation. To characterize the surface roughness, we obtain AFM images for each sample. The roughness of the different surfaces varies with silane chemistry, as shown in representative images in Figure 3.7, but is reproducible between different preparations. From the AFM images, we calculate the root-mean-square (RMS) roughness reported in Table 3.8, as well as the average (R_a), ten point average (R_z), and maximum peak to valley (R_{max}) roughnesses (Table 3.6 in Supporting Information).

3.3.2 Atomic Force Microscopy

Atomic force microscopy (AFM; Nanoscope IV, Digital Instruments) was used to measure the surface roughness of silanized glass surfaces. In a typical experiment, a 4 μm^2 area was scanned at 2 Hz in tapping mode in air using an n-type silicon cantilever (μMasch, resonance frequency = 320 kHz, force constant = 40 N/m). AFM images were analyzed using NanoScope 6.13R1 software to calculate roughness parameters, including average surface roughness (R_a), root-mean-square roughness (R_q), ten-point average roughness (R_z, defined as the difference in height between the average of the five highest

peaks and the five lowest valleys along a profile), and mean peak-to-valley profile roughness (R_{max}).

Table 3.6. Roughness measurements of silanized glass surfaces after preparation. Numbers in parentheses indicate standard deviation from three spot measurements on at least three surfaces

	Roughness (nm)			
Sample	R_a	R_q	R_z	R_{max}
FPTS	0.56 (0.07)	0.7 (0.1)	1.4 (0.3)	7 (2)
FDTS	0.12 (0.01)	0.16 (0.02)	0.20 (0.02)	1.2 (0.1)
PTS	0.52 (0.06)	0.68 (0.08)	1.3 (0.1)	6.4 (0.9)
DTS	0.14 (0.03)	0.17 (0.03)	0.31 (0.04)	2.3 (0.4)
OTS	0.4 (0.1)	0.51 (0.2)	0.7 (0.1)	9 (2)

To evaluate if changes to the surface roughness occurred over the duration of the experiment, silanized surfaces were immersed into 0.9 % NaCl for up to 30 min; this time corresponds to the maximum duration of a bacterial deposition experiment. The roughness of DTS increased 17% after immersion during 30 min in the saline solution (Table 3.7). No change in roughness was observed for FDTS surfaces. FDTS and DTS surfaces were still significantly smoother than any of the other studied surfaces.

Table 3.7. Roughness measurements of silanized glass surfaces after immersion in 0.9 % NaCl. Numbers in parentheses indicate standard deviation from three spot measurements done on at least three surfaces

	R_q Roughness (nm)		
Sample	After silanization	After immersion in 0.9% NaCl for 15min	After immersion in 0.9% NaCl for 30 min
FPTS	0.73 (0.1)	0.56 (0.05)	0.60 (0.03)
FDTS	0.16 (0.02)	0.12 (0.01)	0.16 (0.02)
PTS	0.68 (0.08)	0.53 (0.1)	0.57 (0.2)
DTS	0.17 (0.03)	0.18 (0.02)	0.20 (0.04)
OTS	0.5 (0.2)	0.34 (0.05)	0.34 (0.03)

The DTS and FDTS (C-10) surfaces exhibit RMS roughness of less than 0.2 nm, more than a factor of two lower than all other surfaces of similar chemistry and hydrophobicity. These roughnesses are consistent with those obtained in earlier AFM measurements[128] and molecular simulations[130] for these silanes. Finally, we characterize the surface elemental composition using X-ray photoelectron spectroscopy (XPS) (The chemical groups expected from each silane structure are observed in the XPS spectra (Figure 3.5 and Figure 3.6)**,** confirming that in each case we successfully form silane layers on the glass coverslips. Furthermore, no surface contaminants are identified in the XPS analysis. We therefore conclude that our deposition protocols produce reproducible and (to the best of our ability to determine) contaminant-free multilayers.

Table 3.8. Water contact angle, surface energy, thickness, zeta potential, and roughness of silanized glass surfaces. Numbers in parentheses correspond to standard deviations over five spot measurements done on at least three surfaces for WCA, surface energy and thickness; five aliquots per sample for zeta potential; and five spot scans on two surfaces for roughness.

Substrate	**WCA (°)**	**Surface energy [mJ/m^2]**	**Thickness [nm]**	**ζ-potential [mV]**	**RMS roughness [nm]**
FPTS	78 (3)	30 (1)	1.99 (0.04)	-29 (2)	0.73 (0.1)
FDTS	110 (1)	12 (1)	1.63 (0.02)	-31 (2)	0.16 (0.02)
PTS	92 (2)	29 (1)	1.67 (0.08)	-17 (2)	0.68 (0.08)
DTS	106 (3)	23 (1)	1.67 (0.03)	-26 (2)	0.17 (0.03)
OTS	112 (2)	20 (2)	3.10 (0.2)	-16 (1)	0.51 (0.2)

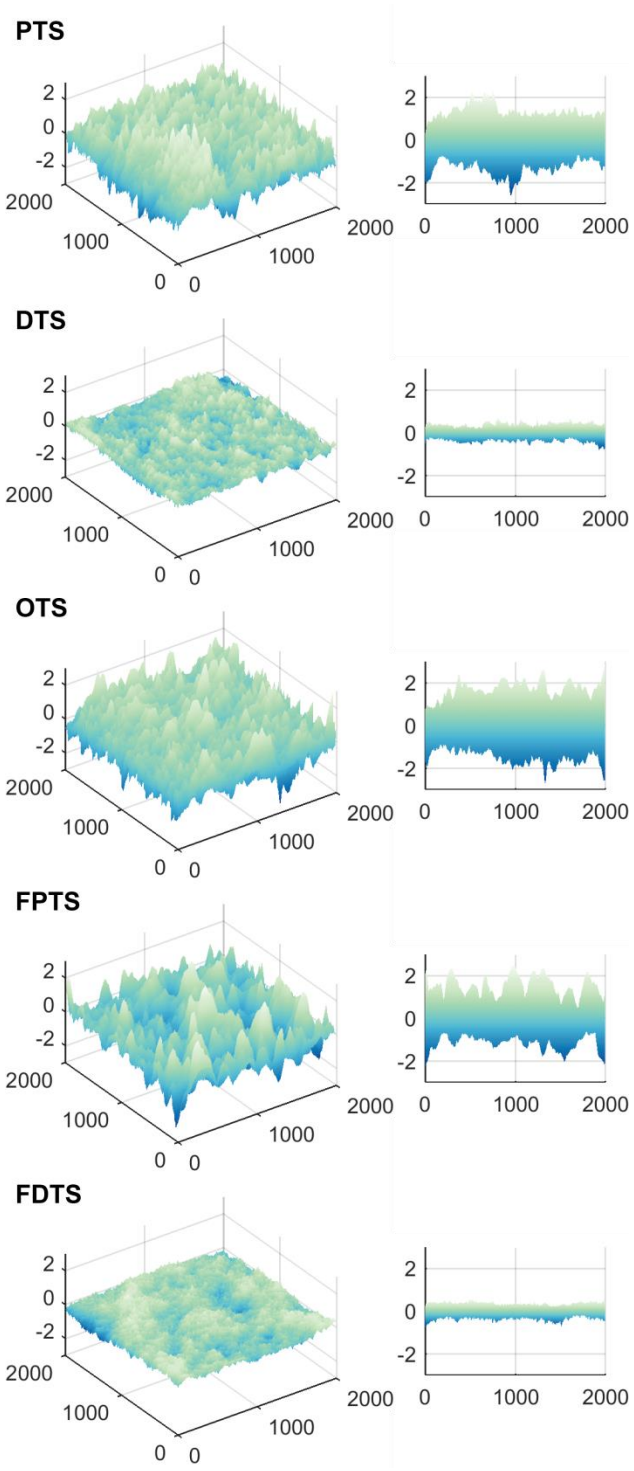

Figure 3.7. AFM images (left) and height maps (right panel) for the five silanized surfaces bearing either -CH_3 or -CF_3 terminal chemistry and C-chain length of 3, 10, or 18. Lengths (on the *x*- and *y*-axes) and heights (on the *z*-axis) are given in nanometers. The FDTS (-CF_3, C-10) and DTS (-CH_3, C-10) surfaces exhibit lower AFM root-mean-square roughness than the FPTS (C-3), PTS (C-3), and OTS (C-18) surfaces of similar terminal functionality.

3.3.3 Bacterial deposition

Subsequently, we flowed bacteria through linear microchannels and allowed them to deposit on the silanized surfaces. For all surfaces, the deposition rate generally decreases with shear stress across the range of shear stresses investigated, as shown in Figure 3.8. The alkyl- and fluoroalkyl-silane surfaces exhibit slightly different dependences of deposition rate on chain length: the deposition rate on fluoroalkyl surfaces varies with C-chain length (Figure 3.8 (a)) whereas the deposition rate did not depend on C-chain length for the alkyl surfaces (Figure 3.8 (b)).

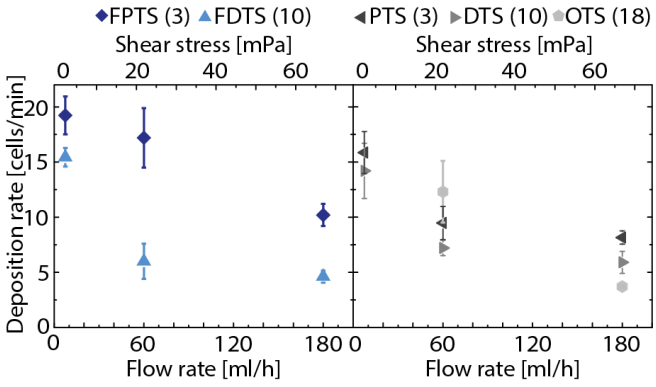

Figure 3.8. Deposition rate (cells/min) as a function of flow rate (bottom *x*-axis) or shear stress (top *x*-axis) for long chain (C-18 and C-10) and short chain (C-3) (a) fluoroalkylsilanes and (b) alkylsilanes on glass. Error bars indicate standard deviation over three replicates. Strain: MC1061.

To understand the variation of deposition rate on the different surfaces, we first estimate the interaction potential between *E. coli* MC1061 bacteria and each silanized substrate using the extended-Derjaguin-Landau-Verwey-Overbeek (xDLVO) theory. The xDLVO potential models the van der Waals, electrostatic, and acid-base interactions between the surface and a rigid spherical bacterium.

3.3.4 Extended DLVO calculation

Extended DLVO theory was used to estimate the interaction between the bacteria and silanized substrates as detailed in our earlier work.[120] Briefly, the interaction of a rigid and spherical bacterium (*b*) with a planar surface (*s*) in a medium (*m*) was calculated as[77]

$$\Delta G^{total} = \Delta G^{LW} + \Delta G^{AB} + \Delta G^{EL}, \quad (3.1)$$

where the superscripts indicate the contributions from Lifshitz-van der Waals (LW), acid base (AB), and electrostatic (EL) interactions.

The surface potential for bacteria and surfaces was estimated from measurements of zeta potential. To approximate the zeta potential of the flat silanized surfaces, we measured the zeta potential of silanized silica nanoparticles. The zeta potentials of the bacteria suspensions and of silanized nanoparticles suspended in 154 mM NaCl was measured using a NanoBrook ZetaPALs (Brookhaven Instruments) ζ-potential analyzer and reported in Table 3.2 and Table 3.8.

To assess the cell surface characteristics of bacteria, we measured the contact angle of water and two other test solvents on bacterial lawns. The bacterial lawns were prepared by spreading 100μL of concentrated bacterial suspension onto a clean glass slide kept during 24 h in a desiccator box.[131] Static water contact angles of the cell lawns were measured using a Dataphysics OCA 15EC goniometer. Reported data correspond to at least eight spot measurements made on three different lawns. The water contact angles obtained for all the studied strains were similar, indicating comparable levels of cell surface hydrophobicity. Contact angles for two other test liquids, ethylene glycol (99%,

Alfa Aesar), and diiodomethane (99%, Alfa Aesar) were also measured on these lawns (Table 3.9). The surface energies of the bacteria and of surfaces were calculated from the water contact angles using the method described by van Oss.[127]

Table 3.9. Contact angles of *E. coli* strains used for surface tension calculations. The standard deviation was calculated from contact angle measurements on at least eight spots on three different bacterial lawns for each bacterial strain.

Strain	Water contact angle [°] (Std. Dev.)	Diiodomethane contact angle [°] (Std. Dev.)	Ethylene glycol contact angle [°] (Std. Dev.)
MC1061	37 (3)	64 (4)	56 (4)
BW25113	40 (4)	63 (6)	58 (2)
JW4277	38 (4)	48(4)	56 (5)
JW1908	37 (4)	60 (5)	59 (4)

Table 3.10. Values of surface energies used in xDLVO calculations

Sample	γ_i^{LW} [mJ/m^2]	γ_i^+ [mJ/m^2]	γ_i^- [mJ/m^2]	γ [mJ/m^2]
MC1061	27	0.11	72	32
BW25113	27	0.16	70	34
JW1908	35	0.80	68	50
JW4277	28	0.41	75	40
PTS	27	0.18	6.2	29
DTS	22	0.010	1.4	23
OTS	20	0	0.3	20
FPTS	23	1.5	8	30
FDTS	11	0.22	2	12

Table 3.11. The maximum attractive force ($F_{\max}^{\mathrm{xDLVO}}$) estimated using the XDLVO theory for different combinations of surfaces and bacterial strains

	$F_{\max}^{\mathrm{xDLVO}}$ (N)			
	MC1061	**BW25113**	**JW1908**	**JW4277**
FPTS	1.9×10^{-8}	1.5×10^{-8}	3.2×10^{-8}	2.3×10^{-8}
FDTS	-6.1×10^{-14}	-6.7×10^{-14}	-8.2×10^{-14}	-1.6×10^{-13}
PTS	3.6×10^{-8}	3.0×10^{-8}	5.0×10^{-8}	4.0×10^{-8}

DTS	5.6×10^{-14}	6.4×10^{-14}	6.2×10^{-9}	1.9×10^{-13}
OTS	-9.5×10^{-15}	-1.1×10^{-14}	-1.3×10^{-14}	-2.5×10^{-14}

The xDLVO calculations predict that *E. coli* MC1061 bacteria experience a strong repulsive interaction upon contacting the long-chain (C-10 or -18) FDTS, DTS, and OTS surfaces but an attractive interaction upon contacting the short-chain (C-3) FPTS or PTS surfaces (Figure 3.9). Our experimental results show that bacteria deposit less on FDTS, DTS, and OTS surfaces compared to FPTS surfaces, but the experimentally observed deposition on PTS is less than expected based on the energetic calculations. The discrepancies between the energetic calculations and the observed deposition patterns suggest that other features on the bacterial surface or silanized substrate affect adhesion. We therefore look for other surface properties that better correlate with observed adhesion.

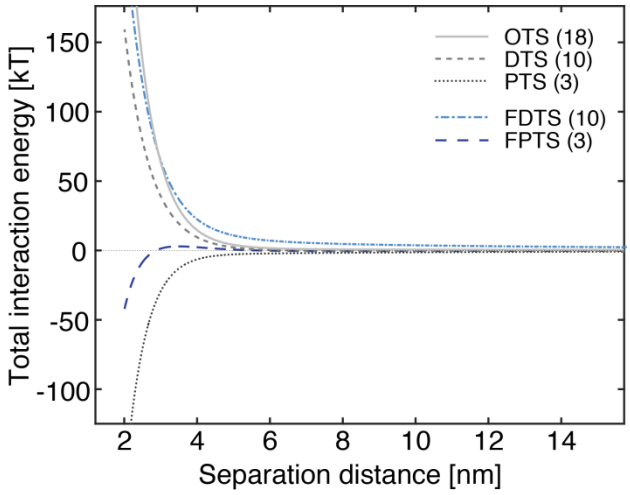

Figure 3.9. Estimated total interaction potential as a function of the separation distance of bacteria from the surface, calculated from xDLVO theory for a sphere-plate interaction, for *E. coli* MC1061 and five silanized glass surfaces in suspensions of ionic strength 154 mM.

The AFM images in Figure 3.7 reveal significant variations in roughness of the different surfaces. The DTS and FDTS surfaces, in particular, exhibit RMS roughness of less than 0.2 nm, more than factor of two lower than all other surfaces of similar chemistry and hydrophobicity (Table 3.8). We therefore surmise that this sub-nm-scale roughness, in addition to shear stress and interaction energy, affects bacterial deposition. To test this idea, we examine the dependence of deposition rate on the RMS roughness. For a given shear stress the deposition rate generally increases with the RMS roughness, as shown in Figure 3.10, with a dependence that is less pronounced than that of shear.

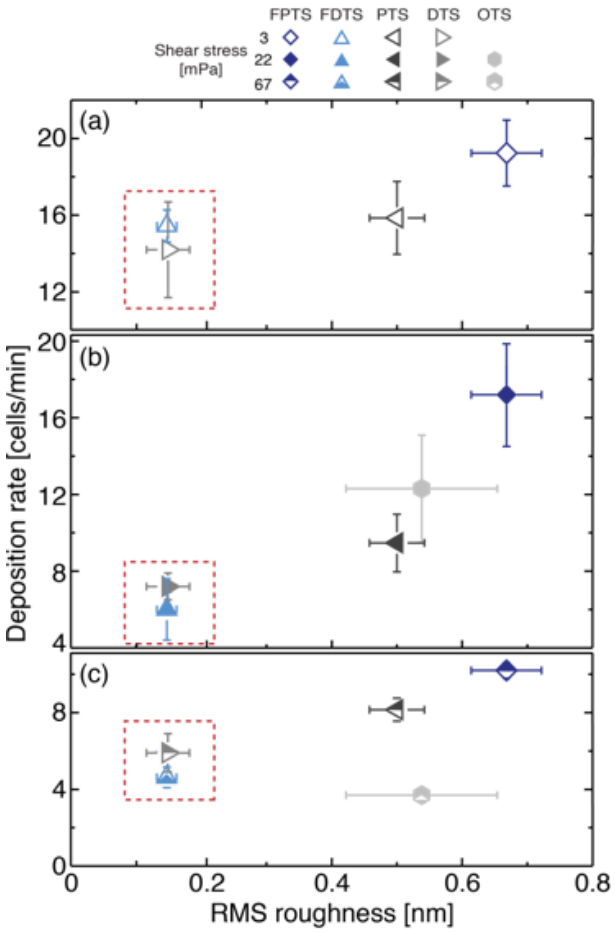

Figure 3.10. Deposition rate as a function of the root-mean-square (RMS) surface roughness at shear stresses of (a) 3 mPa, (b) 22 mPa, and (c) 67 mPa. Error bars indicate standard deviation over at least three replicate measurements. The red boxes indicates the surfaces with roughness less than 0.2 nm, on which cells exhibit mobile adhesion at all shear stresses investigated. The vertical scale is the same for each panel; the different shear stresses are separated for clarity. Strain: MC1061.

It is well known that increasing the surface roughness affects bacterial adhesion. Earlier studies of *E. coli* attachment in static cultures reported decreasing adhesion with increasing sub-nm scale roughness[113] but increasing adhesion with increasing nanoscale roughness.[132, 133] Smooth polymer (Vivathane) surfaces reduced attachment of *E. coli* compared to other rougher biopolymer surfaces.[134] The increase in RMS roughness observed on our silanized glass surfaces are comparable to that reported to reduce adhesion of *E. coli* to nanostructured polyurethane surfaces in static conditions.[113] By contrast, we observe increasing bacterial adhesion with surface roughness at the sub-nm scale.

3.3.5 Near-surface motility

Next, we characterize the amount of motion exhibited by bacteria that closely associate with the substrate. In the microscopy movies, surface-associated bacteria exhibit motion in the form of small displacements of the centroid about a point of tether or site of attachment. In an earlier study, we showed that the rate at which bacteria attach onto silane-functionalized surfaces varied inversely with the extent of this surface-associated motion.[120] To quantify the extent of surface-associated motion on the five test substrates, we define a metric based on the percentage of cells that undergo small displacements.[120] Briefly, we calculate the displacement of the centroid of each bacterium

over each time step (Δt = 3 sec), and calculate, as one metric of the extent of motility, the percentage of individual cell displacements that are larger than 0.12 μm (one pixel). The extent of motility, so defined, generally decreases for each surface with increasing shear stress (Figure 3.11(a)). Differences between motility on different silanes are most pronounced at the lowest shear stress studied (3 mPa) but become insignificant at the highest shear stress (67 mPa). These results suggest that, over the range of shear stresses studied, the surface-associated motion is affected more by shear stress than by surface chemistry. We next examine the dependence of the motility metric on the surface roughness. For a fixed shear stress, the extent of motility decreases slightly with increasing RMS roughness (Figure 3.11 (b)), opposing the trend seen for deposition rate (Figure 3.10); this result is consistent with our earlier study[120] in which this motility metric was inversely correlated with deposition rate.

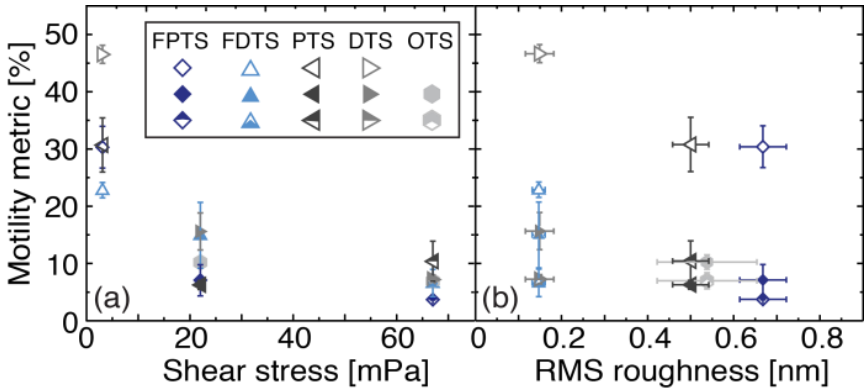

Figure 3.11. The extent of motility metric (percentage of individual cell displacements that are greater than 0.12 μm) as a function of (a) shear stress and (b) root-mean-square (RMS) surface roughness. Symbol weights indicate the shear stress: open symbols: 3 mPa; closed symbols: 22 mPa; half-open symbols: 67 mPa. Errors bars indicate standard deviation over at least three replicate measurements. Strain: MC1061.

In addition, we observe a second type of near-surface motion not seen in our earlier study. On DTS and FDTS surfaces, some bacteria very near the surface translate linearly along the direction of flow (Figure 3.12 (a)). The maximum end-to-end linear displacements of these translating cells, 17 µm on FDTS surfaces and 47 µm on DTS surfaces, are much larger than the cell body dimensions. This long linear translation is qualitatively different from the surface-associated motion about a tethering point also seen on other surfaces of similar terminal chemistry (e.g., PTS, Figure 3.12 (b)).

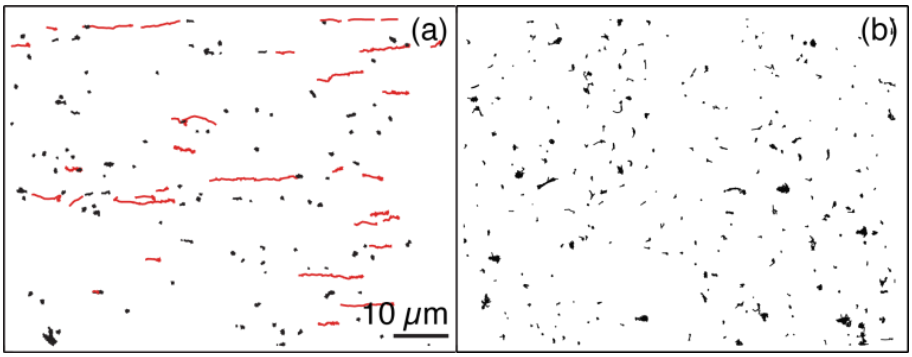

Figure 3.12. (a) Representative trajectories of *E. coli* MC1061 bacteria on (a) DTS-modified glass substrate (shear stress 22 mPa) and (b) a PTS-modified glass substrate (shear stress 3 mPa). Flow is from left to right. Trajectories in red correspond to bacteria exhibiting mobile adhesion, defined as a net linear displacement greater than 2.9 µm; all other trajectories are shown in black. Bacteria exhibit mobile adhesion on DTS but not on PTS surfaces. Scale bar is 10 µm.

In an earlier study on *S. epidermidis,* mobility associated with long linear displacements was termed slipping or mobile adhesion.[106] Here, we identify a near-surface cell as exhibiting mobile adhesion if its net linear displacement in the direction of flow is greater than 2.9 µm. This displacement is greater than twice the maximum displacement observed for bacteria exhibiting surface-associated motion in our earlier

study[120] and is approximately 1.5 times the length of an average *E. coli* bacterium obtained from our image-processing algorithms[54] (which slightly underestimate the cell length). Changing the cutoff by twice the resolution of the tracking algorithm does not change the identification of trajectories exhibiting mobile adhesion (Figure 3.13).

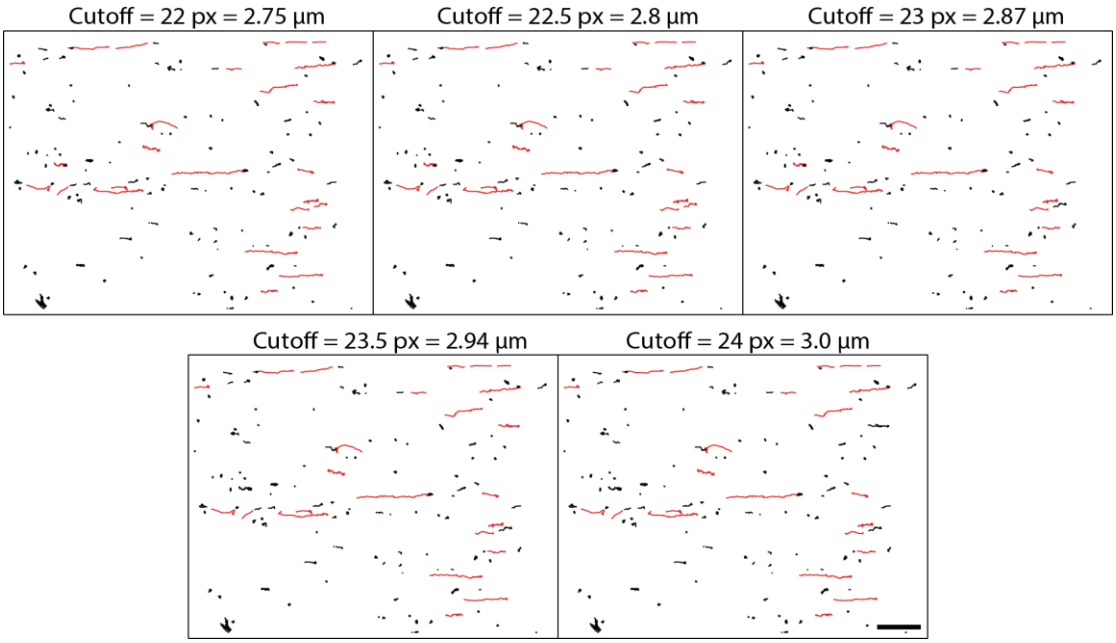

Figure 3.13. The trajectories for mobile (shown in red) and non-mobile cells (shown in black) on a DTS-modified glass substrate (shear stress 22 mPa) for different values of displacement cut-off are compared. The cut-off is defined as the minimum end-to-end displacement of a bacterium used to classify a cell as undergoing mobile adhesion. Scale bar is 10 µm.

We subsequently calculate the fraction of attached cells using mobile adhesion for each surface and for all flow rates. Between 2% and 15% of cells exhibit mobile adhesion on the DTS and FDTS surfaces, depending on the shear rate (Figure 3.14); by contrast, almost no cells on the other three surfaces (FPTS, PTS, OTS) exhibit mobile adhesion. This finding suggests that mobile adhesion does not occur in response to a particular

surface functional (chemical) group: it is observed on alkyl DTS but not on alkyl PTS or OTS; similarly, it is observed on fluoroalkyl FDTS but not on fluoroalkyl FPTS.

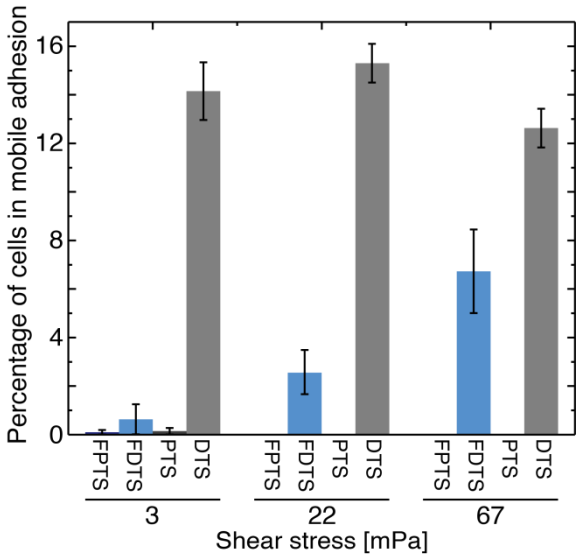

Figure 3.14. Percentage of attaching cells that exhibit mobile adhesion as a function of shear stress. Error bars indicate standard deviation over three replicates. Strain: MC1061.

To understand the factors that give rise to this near-surface mobility, we consider explanations proposed for transient or mobile adhesion in earlier studies. First, XPS analysis reveals no surface contaminants, indicating that chemical contamination does not give rise to mobile adhesion. Next, we consider explanations related to the wettability of the substrates. Earlier experiments on *S. epidermidis* reported that mobile adhesion was favored on hydrophilic substrates.[106] In that study, differences in the likelihood of mobile adhesion on hydrophobic and hydrophilic substrates were attributed to differences in the interaction of water with the surfaces. Bacteria exhibit attractive acid-base interactions with hydrophobic surfaces; as a result, water was readily displaced from the surface to allow bacteria to more closely approach it and establish immobile adhesion. By contrast,

on hydrophilic surfaces there is a significant energy penalty to displace interfacial water, which inhibited the close approach of bacteria to these surfaces; cells that could not closely approach the surface were suggested to be more likely to exhibit mobile adhesion.[106] In our experiments, however, all surfaces are neutrally wetting or hydrophobic (Table 3.8). Nonetheless we observe mobile adhesion of *E. coli* on two of the four hydrophobic substrates, suggesting that hydrophilicity alone is not a sufficient condition for *E. coli* to exhibit mobile adhesion.

Third, we consider explanations related to specific cell-substrate interactions. Earlier reports of mobile or transient adhesion for *E. coli* attributed that mobility to specific chemical interactions between cell surface adhesins and functional groups on the substrate. For example, stick and roll adhesion of *E. coli* is mediated by force-dependent catch bonds between adhesins on the fimbriae and mannose or oligomannose groups on the surface.[115, 135] Stick and roll adhesion was observed when the fimbrial tip protein FimH specifically interacted with mannosylated bovine serum albumin on the surface. When the fluid shear stress was low (0.1 – 1 Pa), cells rolled at speeds of ~30 μm/s across surfaces; at intermediate shear stresses (2 – 10 Pa) cells attached in stationary state, but resumed slow rolling at higher stresses (10 Pa).[60] In another set of experiments, 30 – 50% of bacteria exhibited rolling adhesion on 3-mannose functionalized surfaces at shear stresses between 0.01 – 0.1 Pa; cells converted to stationary adhesion above 2 Pa.[75] In our experiments, however, mobile adhesion does not appear to require specific interactions between the cells and the surfaces. The DTS- and FDTS-modified glass surfaces used in our experiments present no known specific receptors for binding *E. coli* surface adhesins. Moreover, both the fraction of cells exhibiting mobile adhesion in our experiments (2 –

15%) and the speed at which they linearly translate (~0.4 μm/s for shear stresses of 3 – 67 mPa) are smaller than those reported for interaction-mediated mobile (stick-and-roll) adhesion. These comparisons suggest that specific interactions are unlikely to give rise to the mobile adhesion observed here.

Instead, we note that one difference between the DTS and FDTS surfaces (on which we observe mobile adhesion) and FPTS, PTS, and OTS (on which we do not) is the RMS roughness (Table 3.8). DTS and FDTS surfaces are very smooth, with RMS roughnesses of less than 0.2 nm. By contrast, the other surfaces exhibit RMS roughness of 0.5 – 0.7 nm, more than a factor of two greater. No other surface property neatly separates these two groups. Hence we suggest that, because mobile adhesion observed here occurs only on very *smooth* surfaces, it is a physicochemical rather than purely chemical response.

Although cells on both FDTS and DTS surfaces exhibit mobile adhesion, the two surfaces show somewhat different trends as the shear stress is increased. On FDTS surfaces, cells are more likely to use mobile adhesion as the shear stress is increased; by contrast, on DTS surfaces the percentage of cells using this mode does not vary with shear stress (Figure 3.14). Given that the FDTS and DTS surfaces exhibit very similar water contact angles, zeta potentials, thicknesses, and roughness (but somewhat different surface energies), the origin of the different trends is not clear; although the functional groups do not dictate whether mobile adhesion appears, interactions with specific functional groups may still affect the likelihood that cells use mobile adhesion in response to varying shear stress.

3.3.6 Characteristics of mobile adhesion

We first quantify the surface speed of mobile adhering cells from the centroid displacement of each bacterium over each time step ($\Delta t = 3$ sec). On both FDTS and DTS surfaces, mobile adhesion is slow: the speed of cells (< 0.4 μm/s) is significantly slower than both the average velocity of the applied flow (0.05 – 1.25 cm/s) and the typical near-surface swimming speed of *E. coli* (20 – 30 μm/s).[33] On both surfaces, the speed decreases as a function of applied shear stress (Figure 3.16; an explanation of the notched box plot is included as Figure 3.15).

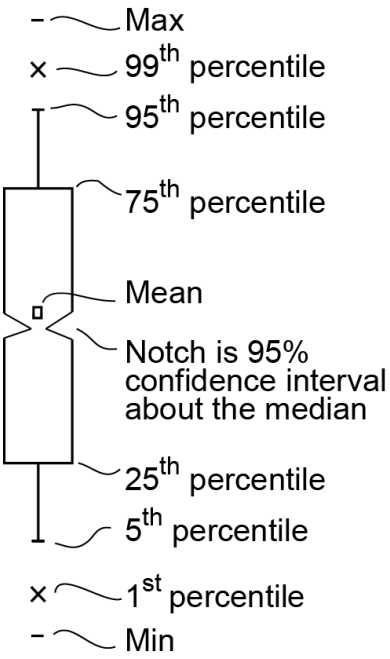

Figure 3.15. Legend defining the notched-box-plot used for reporting data in subsequent figures.

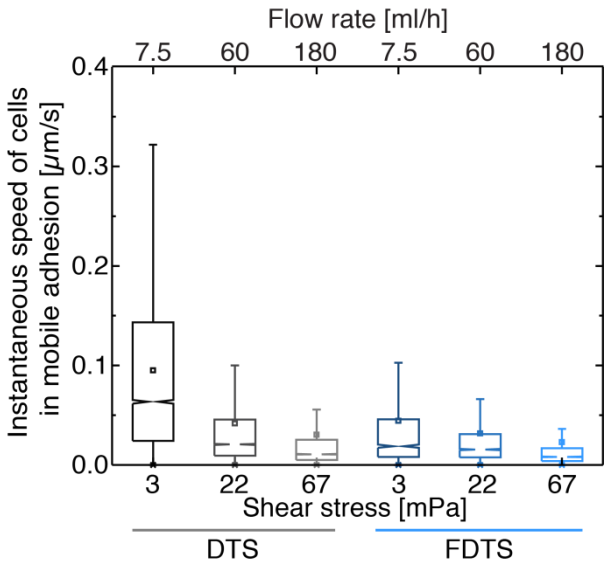

Figure 3.16. Distribution of surface speed (calculated over a single time-step of Δt = 3 sec) of cells in mobile adhesion as a function of volumetric flow rate and shear stress. Number of data points in each speed distribution at volumetric flow rates of 7.5, 60 and 180 mL/h, respectively: DTS (N = 9538, 14381, 7223) and FDTS (N = 1340, 3447, 5110). Notches on the box indicate the 95% confidence interval about the median value. The notches on the box plots above do not overlap for a given surface, indicating that the median values of the speed differ at the 95% confidence level. Strain: MC1061.

This result runs counter to expectations from hydrodynamics; because shear stress increases the hydrodynamic force experienced by a surface-associated bacterium,[136] motions driven solely by hydrodynamic forces would be expected to increase with shear stress. Indeed, earlier studies of colloidal particles rolling on a surface found that their velocity increased from 4 μm/s to 14 μm/s and distance rolled increased from < 1.5 μm to >5 μm as the shear rate was increased from 20 to 50 s^{-1}.[137] Similarly, silica particles on electrostatically heterogeneous surfaces were more likely to persistently roll than to irreversibly arrest as shear stress was increased.[138] Moreover, hydrodynamic colloidal models that predict the shear stresses required for particle detachment through sliding, rolling, or lifting mechanisms[139] or that relate particle detachment to surface and particle

roughness[140, 141] do not correlate to the experimentally-observed mobile adhesion. These comparisons indicate that it is unlikely that mobile adhesion is purely hydrodynamic in origin; instead, we suggest that the slowing of mobile adherent cells in response to increasing shear stress reflects a combination of physicochemical and hydrodynamic interactions to resist detachment as the shear force is increased.

We next consider whether mobile adhesion helps cells to remain near the surface for long times; increased surface residence times could aid cells attempting to colonize environments featuring high shear stresses – with one example being colonization of the urinary tract or of catheters embedded therein.[142, 143] To test whether mobile adhesion allows cells to increase their surface dwell time, we calculated the residence times of each cell interacting with a DTS-functionalized surface, which exhibited the highest frequency of mobile adhesion and the largest cell displacements among all surfaces examined. The residence time of mobile adhering cells on DTS increases with shear stress, as shown in Figure 3.17, and the increase in residence time between 3 – 22 mPa (but not between 22 – 67 mPa) is significant at the 95% confidence level. By contrast, the residence times for cells not in mobile adhesion are uncorrelated with the shear stress. This result suggests that mobile adhesion may enable cells to increase their residence time on the surface, which in turn could promote subsequent irreversible attachment.

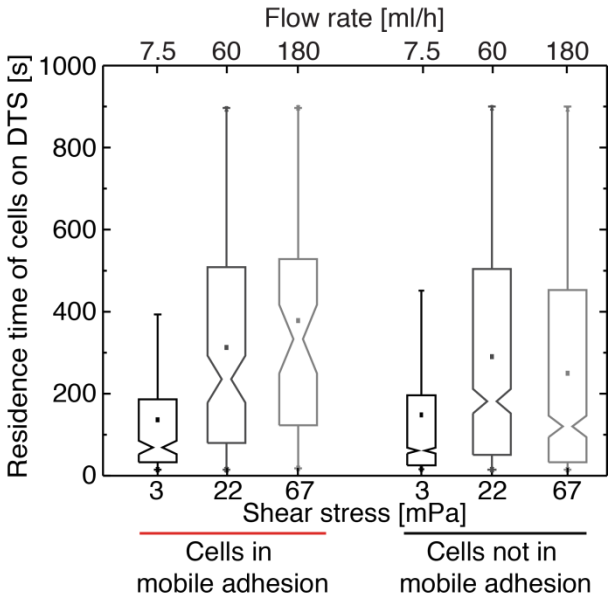

Figure 3.17. Residence time distribution of cells in mobile adhesion (left) and those not in mobile adhesion (right) on DTS. Notches represent the 95% confidence intervals. The (median) residence time of mobile adhering cells increases with shear stress, whereas that for cells not in mobile adhesion does not. Strain: MC1061.

3.3.7 Dependence of mobile adhesion on flagella and fimbriae

Mobile adhesion is observed only on very smooth surfaces. The dependence of mobile adhesion on the sub-nanoscale surface topography is somewhat surprising, as *E. coli* cells have a typical body length and diameter of ~2 μm and ~1 μm, respectively – both significantly larger than the measured nanoscale roughness of the silane surfaces. *E. coli* also possesses surface appendages and extracellular structures, of which two are widely studied and known to mediate attachment on biotic and abiotic surfaces:[25, 46, 97, 144] fimbriae (5 – 7 nm wide and ~1 μm long)[144] and flagella (~ 20 nm wide and 5 – 10 μm long).[144] In addition, fimbriae mediate another kind of (faster) transient adhesion observed in *E. coli*, stick and roll, through specific interaction of the FimH adhesin with mannosylated surfaces.[97] We therefore hypothesize that these surface structures may

affect whether *E. coli* cells exhibit mobile adhesion. To test this idea, we also perform deposition experiments using two different derivatives of *E. coli* K-12: strain BW25113 and two isogenic mutants JW4277 (Δ*fimA*) and JW1908 (Δ*fliC*), that lack the ability to produce fimbriae and flagella, respectively; strain MG1655(Δ*fimA*), which lacks the ability to produce fimbriae (also of K-12 origin); and MG1655-pPCC1401, an engineered strain that overexpresses fimbriae upon induction with IPTG. Expression of flagella in the wild type strains, in MG1655(Δ*fimA*), and in MG1655-pPCC1401, and lack of expression of flagella in the JW1908 strain, respectively, is confirmed through a motility assay and through transmission electron microscopy (TEM). TEM imaging of MC1061, BW25113, and its two mutants reveals that none of these strains express fimbriae, and confirms that MG1655-pPCC1401 expresses fimbriae (Figure 3.3) under the culture conditions used for deposition experiments.

To test the effects of these surface structures on mobile adhesion, we use DTS-coated surfaces and a single flow rate of 60 ml/h (corresponding to a shear stress of 22 mPa); these conditions produce the greatest number of mobile adherent cells in the first set of experiments with *E. coli* MC1061 (Figure 3.14). We observe mobile adhesion for BW25113 and its mutants (Figure 3.18) and also for MG1655Δ*fimA*, none of which express fimbriae (Figure 3.3) but do not observe mobile adhesion on DTS surfaces for the fimbriated strain MG1655-pPCC1401. This result suggests that lack of fimbriae is a necessary condition for mobile adhesion. The frequency of mobile adhesion observed in BW25113 and its mutants is comparable but is approximately half that observed for MC1061 on DTS at 22 mPa shear stress. MC1061 and BW25113, however, are two

different derivatives of *E. coli* K-12 and bear distinct genetic mutations that may contribute to differences in cell-surface interactions.

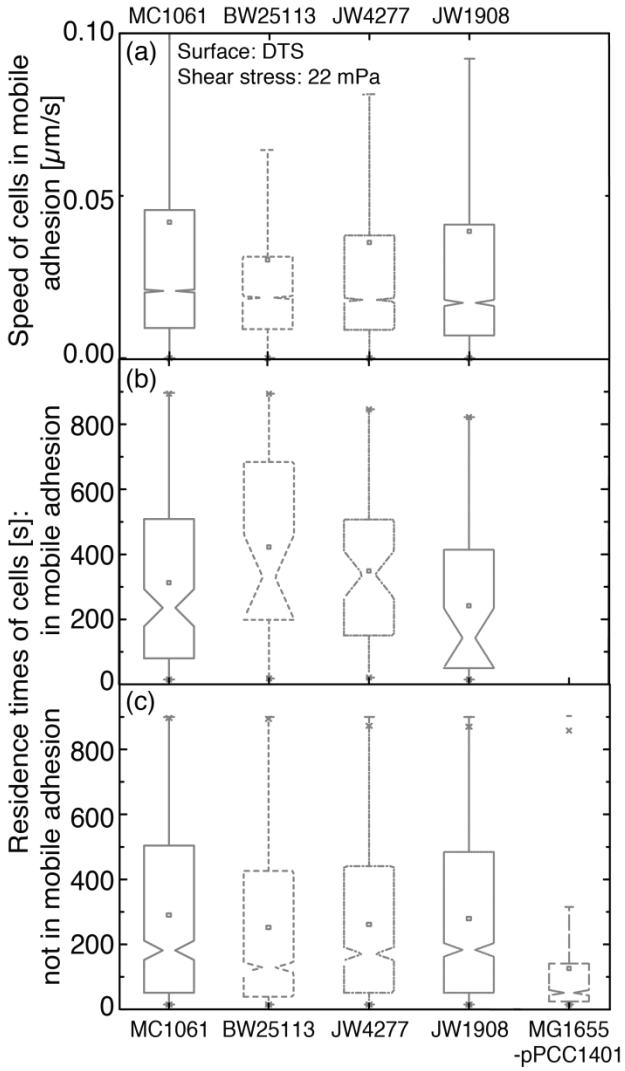

Figure 3.18. Effects of surface adhesins on mobile adhesion of *E. coli* cells flowed at 60 mL/h (shear stress: 22 mPa) on DTS-functionalized surfaces. (a) Distribution of instantaneous speed of bacteria in mobile adhesion on DTS at 22 mPa for *E. coli* K-12 strains MC1061 (wild type), BW25113 (wild type), and isogenic mutants JW4277 and JW1908 (b) Distributions of residence times of bacteria in mobile adhesion. Notches on the box plot represent 95% confidence interval about the mean. The 95% confidence intervals for *E. coli* strain BW25113 and its isogenic mutants JW4277 and JW1908 overlap, indicating that the instantaneous speeds and residence times for these cells does not differ at this confidence level. (c) Distribution of residence times for cells not exhibiting mobile adhesion (for five bacterial strains) on DTS at 22 mPa.

Our results suggest that nanoscale surface roughness plays a critical role in attachment of bacteria on surfaces that do not present specific interaction sites for adhesion. On very smooth surfaces (of roughness below 0.2 nm), and in the absence of fimbriae expression, bacteria in our experiments exhibit mobile adhesion until they either become irreversibly adhered or detach from the surface. Although the differences in roughness are significantly smaller than the dimensions of the cell body, the maximum peak-to-valley height on the silane surfaces (1.4 to 5.6 nm) is comparable to the width of fimbriae and other shorter cell surface adhesins. Therefore, we suggest that changes in bacterial adhesion on surfaces with sub-nm scale roughness arise from interactions of bacterial surface adhesins with the roughness. Hence mobile adhesion occurs for "smooth" (fimbriae-deficient) bacteria on "smooth" (minimally rough) surfaces, suggesting that reduced frictional interactions give rise to this motility behavior. Although reports of non-specific and non-appendage driven bacterial transient motility are rare, two earlier studies relate transient bacterial motility to frictional interactions. First, friction forces acting laterally along the substratum were suggested to induce a transition from mobile to immobile adhesion of *S. epidermidis* on soft and rigid polymer brushes.[98] Second, a theoretical study on deposition of *Streptococcus oralis* on an ideally smooth surface predicted mobile adhesion, arising from the absence of lateral interactions that cause immobilization.[118]

Although the metaphor of friction unifies the two requirements for mobile adhesion (smooth surfaces and lack of fimbriae), one result cannot be explained by such a simple picture: over the limited range of stress probed, increasing shear stress increases the residence time of cells in mobile adhesion. This enhancement is greater than that

observed for cells not in mobile adhesion (Figure 3.17). Specific (fimH-mediated) interactions between cells and substrates weaken over this range of shear stresses and cannot explain this enhancement.[135] Instead, our results appear to be consistent with an earlier report of (apparently) non-specific shear-enhanced adhesion in *Pseudomonas aeruginosa*.[117] In that study, the shear-enhanced increase in residence time could not be linked to a specific interaction; it was independent of the substrate and not mediated by type I pili, type IV pili, flagella, or extracellular matrix. Hence we suggest that the slight increase in residence time for our cells also originates from an as-yet unidentified stress-sensitive mechanism.

3.4 Conclusions

We characterized near-surface motility associated with adhesion in *E. coli* bacteria deposited from flow on glass substrates bearing self-assembled alkylsilane and fluoroalkylsilane films. By analyzing the trajectories of hundreds of bacteria deposited on these surfaces, we found that the deposition rate for all surfaces generally decreased with increasing shear stress. The discrepancy between the predicted xDLVO interaction potentials and the observed relative deposition rates suggested that other interactions influenced deposition. We found that the deposition rate increased approximately linearly with the RMS surface roughness. Similarly, the extent of surface-associated motion decreased with RMS roughness, consistent with greater cell adhesion to the rougher surfaces. Cells exhibited mobile adhesion on very smooth surfaces undergoing large linear displacements. As shear stress was increased, the speed of mobile adhesion decreased and residence time of cells increased. In contrast to earlier reports of near-

surface transient adhesion in *E. coli*,[60, 116, 145] mobile adhesion did not involve specific interactions between bacterial adhesins and the surface. Instead, only cells that did not express fimbriae exhibited mobile adhesion. Because mobile adhesion required very smooth surfaces as well as absence of the adhesive fimbriae, we suggest that this mode reflects reduced friction between cells and surfaces and hence arises from a physical origin. This is in contrast for most known modes of near-surface motility, which are driven directly by appendages[33, 146] or indirectly by specific interactions.[26, 60]

The effects reported here do not apparently depend on active processes of the bacteria but only on roughness, which is known to influence deposition and transient adhesion of abiotic microscale particles. For example, both theoretical and experimental studies of colloidal deposition on surfaces of varying roughness indicate that rough surfaces are more favorable for particle deposition.[147, 148, 149] These studies proposed that the increase in deposition arose from a reduction in the repulsive energy barrier with increased roughness, and/or attractive colloidal and steric interactions that are absent for smooth surfaces.[148, 149] Similarly, rolling adhesion of colloidal particles depends on nm-scale surface chemical/charge heterogeneities.[138, 150] With increasing density of surface heterogeneity (charge) particle motion switched from dynamic rolling to sudden arrest without particle deceleration.[138] This observation is similar to our finding that surface roughness (i.e. heterogeneity in surface topography) determines the transition from mobile to immobile adhesion for bacteria.

Initial cell-surface interactions are thought to affect biofilm growth and composition.[15] Reducing frictional interactions between cells and surfaces, either by engineering nanoscale-smooth surfaces or by suppressing expression of cell surface

adhesins, may help to reduce fouling during initial deposition. After the initial surface interaction, however, mobile adhesion increases the residence time of cells near surfaces; this behavior may help cells to resist detachment and hence promote *E. coli* biofilm formation in settings in which cells are exposed to varying and/or high shear stresses, such as in bioreactors[151] or on medical implants.[44] In the later stages of biofilm formation, however, cells excrete extracellular polymeric substances that condition the surface and promote surface attachment. Hence we expect that strategies to reduce frictional interactions will be most effective in the very earliest stages at which cells initially encounter surfaces.

Note: The material presented in this Chapter has been published.

Sharma, S.; Jaimes-Lizcano, Y. A.; McLay, R. B.; Cirino, P. C.; Conrad, J. C. Subnanometric Roughness Affects the Deposition and Mobile Adhesion of Escherichia Coli on Silanized Glass Surfaces. *Langmuir* **2016**, *32*, 5422-5433.

References, Figure numbers and Table numbers and their order of appearance have changed with incorporation of article supporting material in the chapter and also for dissertation consistency.

Chapter 4 Surface- and near-surface-associated motion of *E. coli* in viscous suspensions

4.1 Introduction

Bacterial adhesion to surfaces typically involves transport to the surface in a fluid medium.[152] Therefore, the properties of the fluid medium are expected to play as important of a role in bacterial attachment as those of the surface. In industrial applications such as oil recovery and treatment,[153] pulp making,[154] and food processing,[89] bacteria are transported through fluids of varying salt concentration and viscoelasticity in the presence of non-Newtonian fluids. Similarly, bacteria encounter viscoelastic and non-Newtonian fluids such as saliva,[155] mucus,[156] and blood serum[157] in human and animal hosts. Therefore preventing biofouling and biofilm formation in industrial and biomedical applications requires understanding how bacterial adhesion and motility are affected by the rheological behavior of the surrounding environment. Existing studies have focused on understanding the effect of solution viscoelasticity[158, 159] or ionic strength[38, 160] or surface properties[120, 161] on bacterial adhesion and/motility. Some experimental[162, 163] and simulation studies[163, 164, 165] have investigated the dynamical behavior of rigid spheres in viscoelastic media in close proximity of solid boundaries. Another previous computational study[166] investigated the motion of swimming microorganisms in viscoelastic media near a surface. There remains the need to address and understand the effects of both fluid and surface properties on near-surface bacterial adhesion and mobility.

The effects of fluid properties and of surface properties on the motility of bacteria have been reported in the literature. Prior experiments on bacteria showed that 'run and tumble' motility, typical of peritrichously-flagellated bacteria such as *E. coli*, is affected by the presence of polymers in the fluid medium. In these environments, polymer additives enhance translational motion and reduce rotation of cells, thereby suppressing tumbling.[159] Separately, other studies showed that bacterial adhesion on surfaces is significantly affected by solution ionic strength,[160, 167] and by functional groups on the surface. There is a need for a well-characterized model system in which to separately tune fluid and surface properties. Self-assembled layers of silanes are a convenient model system in which to vary functional groups, as silanes can inhibit bacterial adhesion and biofilm formation[30, 70] and the functional groups present on silanes and resulting surface chemistry [charge, wettability and roughness] of the silane layer sensitively affected the force of bacterial adhesion[71, 120, 168] Role of solution ionic strength can be studied by changing concentration of non-toxic salts such as NaCl that also replicate physiological conditions and are known to affect adhesion and deposition of both rigid colloids[169] and active bio-colloids.[160] Polymers such as polysaccharides provide a simple model wherein solution viscoelasticity can be varied without affecting bacterial viability.[159] It is required to design experimental studies where both solution and surface properties are systematically varied to understand their role in bacterial adhesion and near-surface motion.

Here, we experimentally investigate the competing effects of solution ionic strength, surface wetting, and fluid viscoelasticity on bacterial attachment and near-surface motion. To create model surfaces of controlled wettability, we deposited a silane

bearing an alkyl functional group to obtain a hydrophobic glass surface and used cleaned glass slides as a hydrophilic control surface. Solution ionic strength was varied by adding a monovalent salt, NaCl. Solution viscosity was varied by adding a widely-studied model polysaccharide, xanthan gum, to sample suspensions after cell culture. Bacteria moving near surfaces can be separated into swimming and non-swimming cells using a criterion based on the maximum displacement of each cell. The mobility of non-swimming cells is nearly diffusive on short time scales and sub-diffusive on long time scales irrespective of surface chemistry, solution ionic strength, or polymer concentration. By contrast, the mobility of swimming cells is nearly ballistic in all conditions investigated. Ionic strength and polymer concentration affect the proportion of cells not-swimming or swimming near glass surfaces; by contrast, no significant effect is seen for the DDMCS surface. Addition of polymer increases mobility of swimming cells until a concentration of 13c*, independent of solution ionic strength or surface chemistry; further increase in polymer concentration to 23c* surprisingly reduces the mobility. The radius of trajectories for cells swimming in circles near the surfaces increases linearly with polymer concentration and solution viscosity. We attributed the increase in swimming speed with addition of polymer until a concentration of 13c* to a combination of local shear thinning and elasticity of the polymer leading to enhanced bacterial transport. Finally, at the highest polymer concentration (23c*) swimming bacteria can reverse direction and retrace their paths, characteristic of hindered motion near an obstacle. We posit that increased entanglements between polymer chains impeded the motion of the bacteria resulting in both reduced speed and hindered motion.

4.2 Materials and methods

4.2.1 Bacteria culture

The K12-derived *Escherichia coli* strain MC1061 was used in this study (strain courtesy of Prof. Patrick Cirino and Christopher Frei, University of Houston). The cells contained a plasmid (pFG10) for chloramphenicol resistance and for enhanced green fluorescence protein (GFP), which allowed visualization of cells under fluorescence microscopy.

Bacteria were streaked on Luria Bertani-Agar plates (5 grams yeast extract, 10 grams of Bacto-tryptone, 5 g NaCl, 15 grams agar, all from BD Chemicals) containing 30 µg/ml of chloramphenicol (Spectrum) and incubated overnight at 37ºC (Nuvaire Inc.). Single colonies from the plate were used to inoculate 50 mL sterile Luria Bertani medium, (5 g yeast extract, 5 g NaCl and 10 g tryptone per 1 liter medium, BD Chemicals) containing 30 µg/ml of chloramphenicol and incubated in an orbital incubator shaker (IncuShaker Mini, Southwest Scientific) at 200 rpm and 37ºC for approximately 17 hours. To create a dense pellet, cells were centrifuged at 5000g in a Sorvall ST 16 Centrifuge (Thermo Fisher Scientific) for 10 minutes. After pelleting, the cells were re-suspended either in 0.9% NaCl solution (ionic strength 154 mM) or deionized (DI) water (resistivity 18.2 MΩ-cm, Millipore water purification system). Cells were washed twice in NaCl or DI water by repeated gentle swirling for mixing, centrifuging, and re-suspension to remove the growth medium. Finally, before preparing sample suspensions for imaging, cells were suspended in either 154 mM NaCl or DI water and diluted volumetrically to an optical density (measured at a wavelength of 600 nm) OD600 of 0.42 (with a background subtraction of 0.03 applied), measured using a cell density meter

(Cole Parmer). Cells in all experiments were in a stationary stage of growth, based on a growth curve generated by measuring the OD600 of a growing culture at 30-minute intervals for 24 hours.

4.2.2 Polymer solutions and characterization

Xanthan gum (Sigma Aldrich) was used as the crowding agent. Solutions of xanthan gum at concentrations of 0.5, 1, 2, and 3.5 mg/mL were prepared by weighing appropriate amounts of solid xanthan gum into a vial. Subsequently, the xanthan was dissolved in sterile DI water by gentle tumbling on a roll mill for at least two days to homogenize. The samples were visually inspected to ensure complete homogenization. To prepare suspensions of xanthan at higher solution ionic strengths, an appropriate amount of solid NaCl was added to polymer solutions and allowed to tumble for at least 1 h before use in experiments. The samples were visually inspected again after salt addition to confirm that the salt completely dissolved.

4.2.2.1 Intrinsic viscosity and polymer overlap concentration

A stock solution of 0.5 mg/mL xanthan gum in sterile DI water was prepared as described above. Xanthan gum solutions over a range of dilute concentrations were prepared by diluting appropriate amounts of this stock with sterile DI water. Each solution was passed through an Ubbelohde viscometer (either Technical Glass Product 1 or Cannon 0C) that was suspended in a water bath at 25 ºC; subsequently, to measure the viscosity at a shear rate of 101 – 306 s^{-1}, we determined the efflux time through the viscometer. The intrinsic viscosity $[\eta]$ = 68 dL/g was calculated from the change in viscosity as a function of concentration as shown in Figure 4.1 and the overlap

concentration was determined as $c^* = 1/[\eta] = 0.15$ mg/mL. This value is similar to those reported for xanthan gum measured using rheology or dynamic light scattering (DLS).[170]

Table 4.1. Concentration of polymer solutions

Xanthan gum concentration c [mg/mL]	c/c*
0.5	3
1	7
2	17
3.5	23

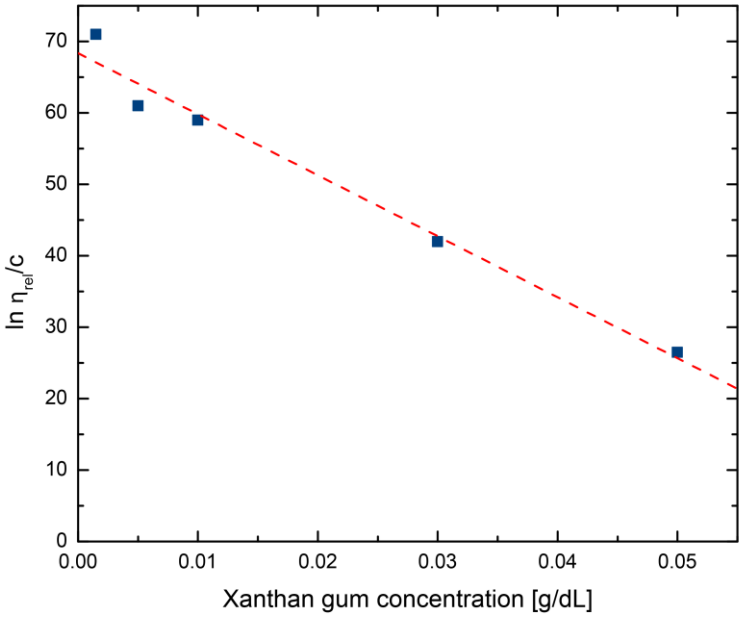

Figure 4.1. Natural logarithm of the relative viscosity of xanthan gum solutions as a function of polymer concentration (in g/dL). The dashed line indicates a linear fit.

4.2.2.2 Rheology of polymer solutions

To measure the rheological properties of the polymer solutions we used a DHR rheometer (TA Instruments) equipped with a Couette geometry (cup diameter 30.36 mm, bob diameter 27.92 mm, bob length 41.89 mm, and gap height 4 mm). Approximately 8

mL of each polymer solution was loaded gently into the Couette cell, with care taken to ensure that no bubbles formed during the loading. We performed steady-rate sweep tests on each polymer solution and thereby measured the viscosity as a function of shear rate over the range 10^{-3} s^{-1} to 10^{2} s^{-1}. To verify the reproducibility of the viscosity measurements, we measured the change in viscosity as a function of increasing and decreasing shear rates, as shown in Figure 4.2. Our measurements were reproducible between polymer solutions prepared from separate dilutions. Additionally, for one concentration of polymer (3.5 mg/mL) we performed a steady sweep test using both Couette and cone and plate geometries. The viscosities obtained in these replicate measurements were in reasonable agreement within experimental error, confirming the reproducibility of the measurements.

The viscosity decreased with increasing shear rate, as expected based on earlier measurements on xanthan gum,[171] and increased with the concentration of polymer, as shown in Figure 4.2. We fit the shear-rate-dependent steady-shear viscosity using the Carreau-Yasuda model (equation 4.1)[172] commonly used to describe shear–thinning fluids. In this model, the viscosity is high and nearly constant at low shear rates; exhibits shear-thinning at intermediate shear rates; and is low and nearly constant at high shear rates. Numerically, in the Carreau-Yasuda model, the viscosity as a function of the shear rate, $\dot{\gamma}$ is given as

$$\frac{\eta-\eta_\infty}{\eta_0-\eta_\infty} = [1 + (\lambda\dot{\gamma})^a]^{(n-1)/a} . \quad (4.1)$$

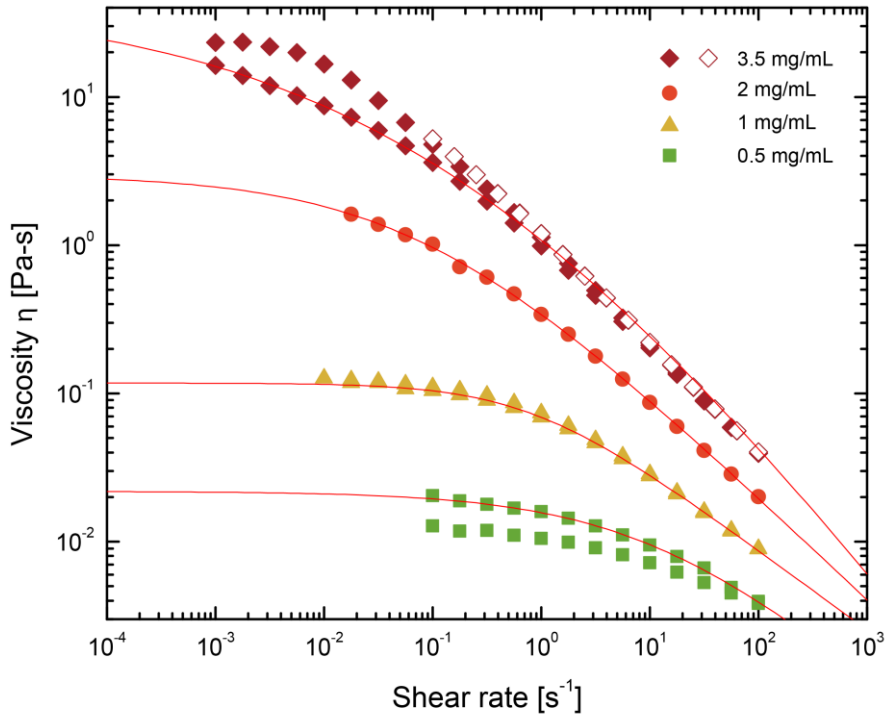

Figure 4.2. Steady state viscosities as a function of shear rate for polymer concentrations varying from 0.5 – 3.5 mg/mL and solution ionic strength 154 mM NaCl. Colors indicate polymer concentration 0.5 (green), 1 (yellow), 2 (orange) and 3.5 mg/mL (red). Open symbols indicate data from steady sweep test done on cone and plate geometry. Lines indicate fits to Carreau-Yasuda model (Equation 4.1).

Here η_∞ is the high-shear viscosity, η_0 is the zero-shear viscosity, λ is the relaxation rate, a is the transition control factor, and n is the power law exponent.

To test the effect of solution ionic strength on viscosity, solutions of xanthan gum in water and in 154 mM NaCl at 1 mg/mL and 3.5 mg/mL concentration were characterized using bulk rheology. We found that addition of salt did not significantly alter the viscosity of xanthan gum solutions over this range of polymer concentrations (Figure 4.3). The zero shear viscosities extracted from fits of the Carreau -Yasuda model are in agreement again indicating that over this range of salt and polymer concentration, the viscosity did not vary significantly (Table 4.2).

We first extracted the zero shear viscosity as a function of polymer concentration from fits to the Carreau -Yasuda model (equation 4.1). The zero shear viscosity increased with polymer concentration, as shown in Figure 4.4 At concentrations up to ~8.5*c** the viscosity scaled with polymer concentration as a power law with a slope of 2, whereas at higher concentrations it scaled with a slope of 4.7. The change in scaling exponent with concentration was consistent with a crossover from semi-dilute unentangled behavior (at concentrations below ~8.5*c**) to semi-dilute entangled behavior (at concentrations somewhat above ~8.5*c**) expected for neutral polymers; hence we tentatively identified this crossover concentration (8.5*c**) as the entanglement concentration. The scaling behavior observed for xanthan gum solutions here is in good agreement with the scaling predictions for a neutral polymers in a theta solvent.[171]

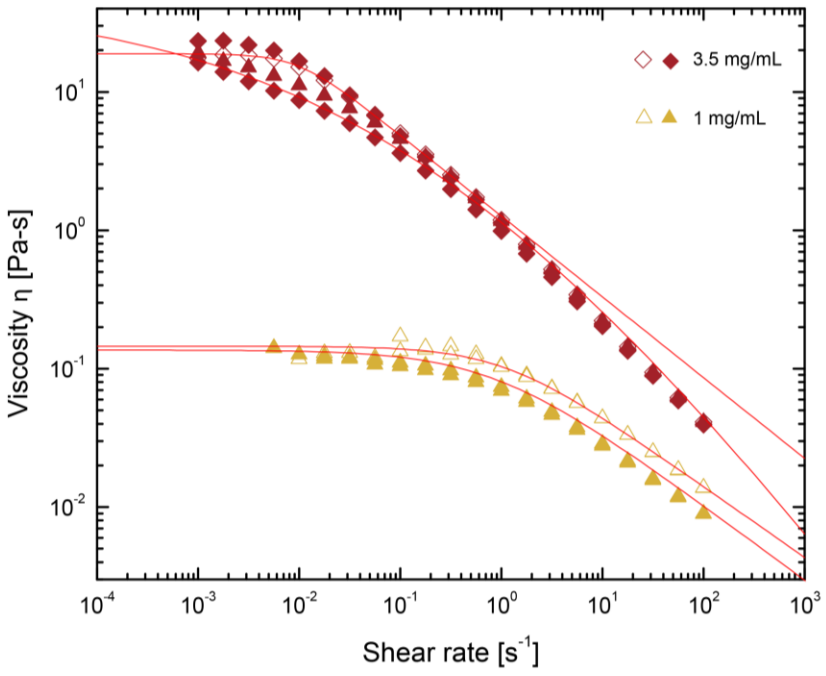

Figure 4.3. Viscosity as a function of shear rate for xanthan gum solutions in water (open symbols) and in 154 mM NaCl (closed symbols). Lines indicate fits to the Carreau-Yasuda model (equation 4.1).

Table 4.2. Zero-shear viscosities, relaxation time and power law exponent obtained from fitting the Carreau-Yasuda model (equation 4.1) to steady-sweep viscosity curves for xanthan gum solutions in water and in 154 mM NaCl

Polymer concentration [mg/mL]	**Solution ionic strength [mM NaCl]**	**Zero shear viscosity [Pa-s]**	**Relaxation time [s]**	**Exponent *n***
1	0	0.14	0.95	0.48
1	154	0.13	1.3	0.46
3.5	0	19	101	0.41
3.5	154	23	128	0.37

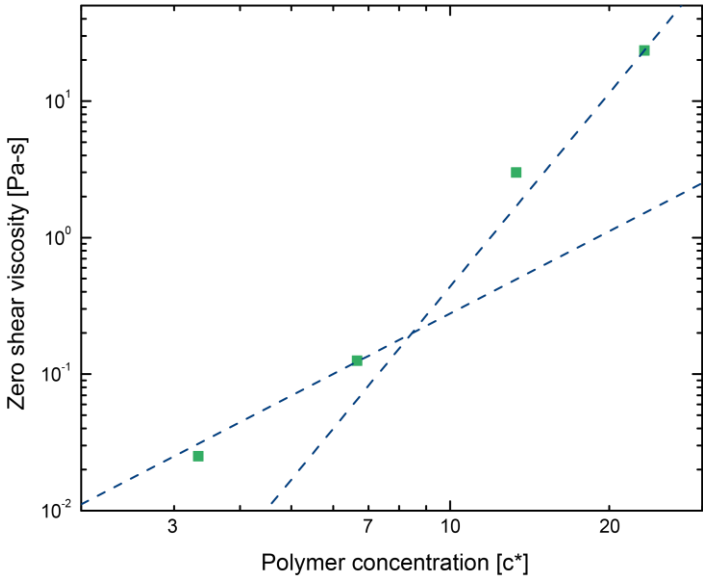

Figure 4.4. Zero shear viscosity extracted from fitting of the Carreau-Yasuda model (equation 4.1) to the steady-state viscosity data in Figure 4.2, as a function of polymer concentration. Lines indicate power law fits to the data. At low concentrations the viscosity scaled with a power law of exponent 2 whereas at higher concentrations, it scaled with a power law exponent of 4.7. From the crossover, the transition from semidilute-unentangled to semidilute-entangled is estimated to be 8.5c^*.

Second, to determine whether the shear thinning behavior changes with polymer concentration we also extracted from the Carreau-Yasuda fits, the shear thinning exponent, n. The plot of exponent, n as a function of polymer concentration (Figure 4.5) showed that, over this range of concentration the shear thinning behavior did not vary systematically and significantly.

Third, fits to the Carreau-Yasuda model provide an estimate of the characteristic polymer relaxation time λ. On time scales shorter than λ, the polymers act elastically and store energy; on longer time scales, the polymers dissipate energy. The relaxation time λ increased as a function of polymer concentration, consistent with frictional forces between the polymer chains slowing the polymer relaxation (Figure 4.6). A power law fit to the relaxation time revealed a scaling behavior of 4.2. This dependence on concentration was somewhat stronger than that expected for a neutral or charged polymer in a good solvent[173] but was similar to that observed for salt-free xanthan gum solutions above the critical concentration $c_{D.}$[171] This critical concentration is defined as a concentration above which polymer chains are entangled, with the number of entanglements increasing with concentration.[171]

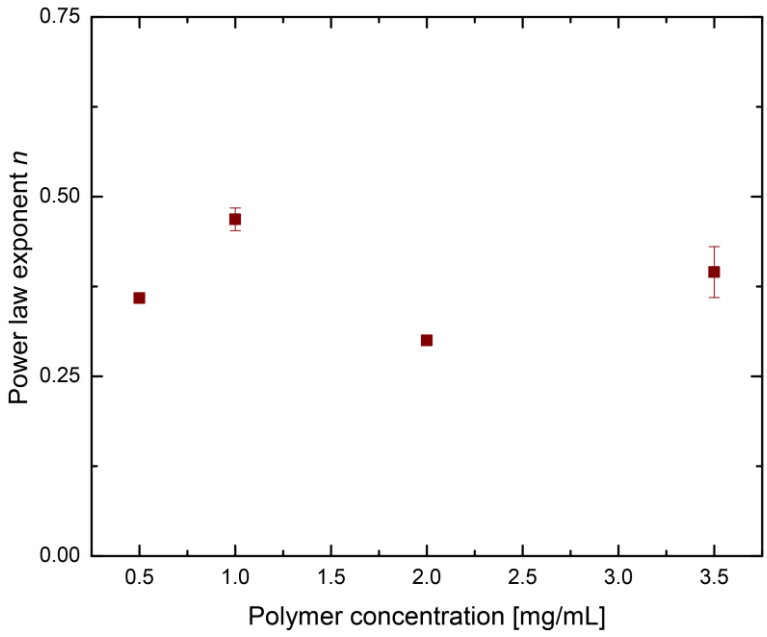

Figure 4.5. Shear thinning exponent *n* as a function of polymer concentration. The shear thinning behavior of xanthan gum does not vary systematically and significantly over the range of polymer concentration studied.

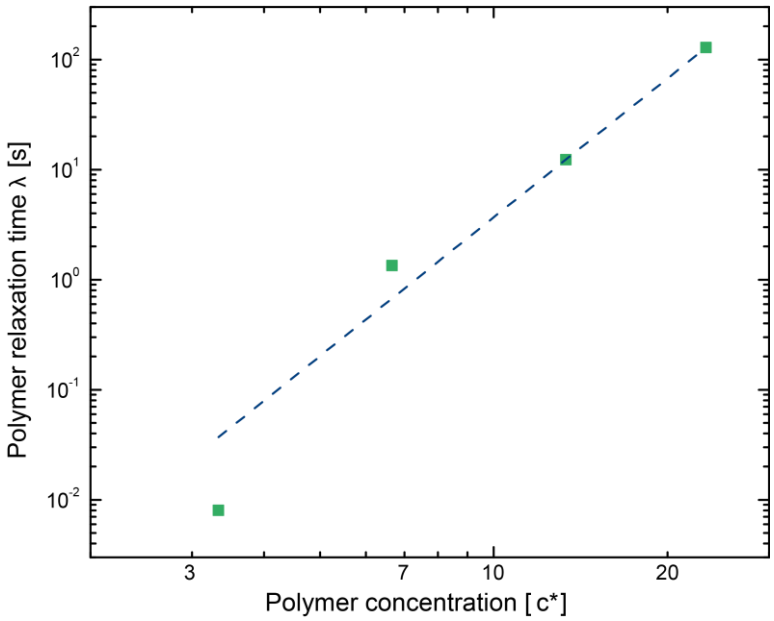

Figure 4.6. Polymer relaxation time λ as a function of concentration. The line indicates a power law fit with a scaling exponent of 4.2.

4.2.3 Substrate preparation

Hydrophobic substrates for quiescent bacteria experiments were prepared by solution deposition of decyldimethylchlorosilane (DDMCS) (Gelest) on glass (Figure 4.7). This silane bears an alkyl functional group; in the absence of reactive side groups, this silane was expected to form monolayers on glass, so that the resulting surfaces were expected to be somewhat hydrophobic. Glass coverslips of dimension 48 × 65 mm^2 (thickness 0.13—0.17, Gold Seal) were first cleaned by successive sonication in acetone (Macron, AR grade) and double de-ionized (DI) water (resistivity 18.2 MΩ-cm, Millipore water purification system) for five minutes each and then treated with air plasma for two minutes. The plasma-treated slides were then immersed in a 0.96 mM solution of DDMCS in hexane (Sigma Aldrich) for two hours. After deposition, slides were sonicated in chloroform (Sigma Aldrich), acetone (Macron), and DI water successively for two minutes each. Slides were finally dried under nitrogen and baked at 110 ºC for 10 minutes. As a control, we also generated a hydrophilic substrate. For this control, glass slides were cleaned by sonication in acetone and water and dried under nitrogen less than 2 hours before being used in an imaging experiment. Water contact angles for both surfaces were measured using a Dataphysics OCA 15EC goniometer. Reported data corresponded to at least five spot measurements made on three surfaces (Table 4.3).

Table 4.3. Water contact angles for glass and for DDMCS-modified glass.

Surface	Water contact angle [std. dev.]
Glass	23 [4]
DDMCS	83 [4]

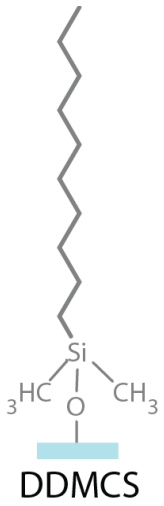

Figure 4.7. Schematic of expected chemical structure of decyldimethylchlorosilane (DDMCS) as-deposited on glass.

4.2.4 Imaging bacteria suspensions

Samples for imaging were prepared by mixing bacteria suspended in water or in NaCl solutions with polymers dissolved in water or in NaCl solution in a 1:3 ratio by volume resulting in a final sample OD of 0.11. Specifically, we prepared samples with ionic strength of 0, 38.5, or 154 mM and polymer concentrations of 0, 0.5, 1, 2, and 3.5 mg/mL, corresponding to 0, 3, 7, 13, and 23c*. Bacteria-polymer suspensions were gently vortex mixed for 5 s. After mixing, 20 – 30 μL of a given sample was pipetted into a sample chamber, which was prepared by affixing double sided tape to the functionalized or cleaned glass substrate, and covered with a cover-glass to prevent the sample from drying during imaging.

Near-surface motion of bacteria in these samples was imaged using a confocal fluorescence scanner (VT Infinity, Visitech) attached to a Leica DM4000 inverted microscope equipped with a 63x oil immersion lens (HCX PL APO CS of numerical aperture 1.4) and laser excitation source λ = 488 nm. Images were acquired at a frame

rate of 12.5 fps, an exposure time of 40 ms, and a pixel size of 0.196 ± 0.0006 μm using an ORCA 200 camera (Hamamatsu) that is controlled by Voxcell Scan software (Visitech). For each sample, 1000 images with area of 131 × 100 μm^2 (corresponding to 672 pixels × 512 pixels) were acquired at least four minutes after sample was loaded into the chamber. Experiments on each of the surfaces were performed in triplicate; at least one experiment in each set was performed on a different substrate and with a different bacteria culture.

Single bacterium-tracking algorithms, written in IDL (Exelis VIS) and based on algorithms used to track rodlike colloidal particles[69] and modified for elongated bacteria,[54] were employed to locate and track the centroid of each bacterium in the microscopy images. Further analysis of bacteria displacements and swimming speeds was performed using routines written in Matlab (MathWorks) and in IDL.

4.3 Results and discussion

We imaged and tracked the near-surface motion of *E. coli* on hydrophilic glass and hydrophobic DDMCS modified glass in suspensions of varying ionic strength and polymer concentration. First, we consider cells swimming in solutions of fixed ionic strength and surface chemistry but varying polymer concentrations. We examine the trajectories of all bacteria and observe that there are at least two distinction populations of cells, which can be distinguished by their near-surface mobility: (a) cells exhibiting surface-associated (non-swimming) motion, which is characterized by small displacements (less than 3 μm); and (b) cells swimming near the surface, which is characterized by large displacements (greater than 3 μm) (Figure 4.8). We therefore use

the maximum displacement between any two points along a particle trajectory as the criteria to classify each bacterium as swimming or non-swimming throughout all experiments.

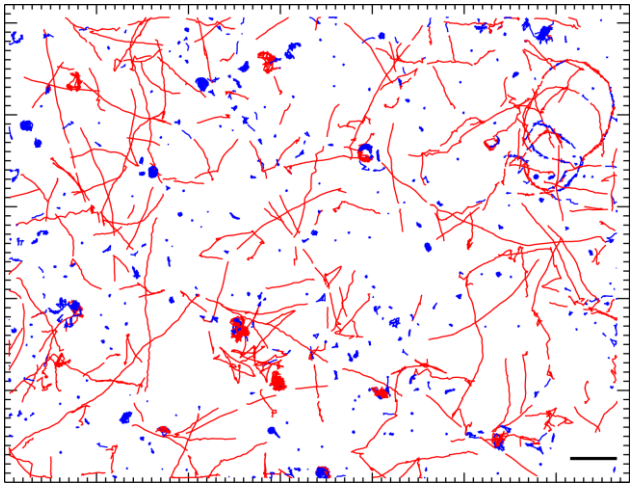

Figure 4.8. Representative trajectories of swimming bacteria (red) and non-swimming cells (blue), classified by the maximum displacement between any two points on the trajectory (as greater than or less than 3 μm respectively) on a DDMCS modified glass surface and a polymer concentration of 7c^* and ionic strength 154 mM NaCl. Scale bar corresponds to 10 μm.

Next, we calculate the ensemble-averaged mean square displacement (MSD) for swimming and non-swimming populations in experiments of varying surface chemistry, solution ionic strength, and polymer concentration. The magnitudes of the MSD for each population are distinct, as expected from the criterion used to separate trajectories (which depends on an absolute displacement). More interestingly, we find that swimming trajectories typically show a MSD of slope 1.6 – 1.8 indicating that the motion of swimming cells is near ballistic. By contrast, the non-swimming trajectories show a MSD with initial slopes of 0.8 – 1 and a long time slope of 0.4 – 0.5, indicating that the

mobility of non-swimming cells is nearly diffusive on short time scales and sub-diffusive on long time scales.

First, we examine the dependence of the MSD near a DDMCS surface on polymer concentration. The MSD of non-swimming cells is nearly independent of polymer concentration and decreases slightly only at the highest polymer concentrations (23c*); by contrast, the MSD for swimming cells increases with the addition of polymer but decreases above 13c* (Figure 4.9). Next, we compare the MSD values for cells in solutions of constant polymer concentration but different solution ionic strengths. Bacteria in these solutions also sort into populations of swimming and non-swimming cells (Figure 4.10 (a-e)). We find that ionic strength has little effect on the dynamics of non-swimming cells at a nonzero polymer concentration. The MSD values for swimming cells are of similar order of magnitude across all ionic strengths for all polymer concentrations, (Figure 4.10 (a-d)) and are greatest at the intermediate ionic strength (38 mM) for all tested polymer concentrations save 23c*. In sharp contrast, the dynamics of cells noticeably slow with increasing ionic strength for the control suspensions without polymer (Figure 4.10 (e)); in these conditions the ions in solution are expected to screen charge interactions between surface and negatively charged cells and allow greater attachment. Ionic strength controls the mobility of both swimming and non-swimming cells in absence of polymer, whereas in presence of polymer the effect of ionic strength on bacteria-surface interactions is not significant.

Finally, we compare the MSD of cells on DDMCS and glass surfaces (Figure 4.11). The MSD again exhibits consistent distinctions between the two (swimming and non-swimming) populations, indicating that sorting into two populations is not affected

by the surface properties. The dynamics of swimming cells are slower near a DDMCS surface than near a glass surface. Also, the MSD values for non-swimming cells are lower on DDMCS than on glass (in presence of polymer); and similar on both surfaces (for the control). We attribute these differences to the different interactions expected for surfaces of different surface wettability and chemistry.[120] Additionally, the MSD initially increases with addition of polymer (e.g. 7c*) and then decreases at the highest concentration (23c*) for both surfaces indicating that effect of polymer concentration is not affected by differences in surface chemistry. Collectively, the measurements reported in Figures 4.9 – 4.11 suggest the distinction between non-swimming and swimming populations is robust across surface wettability and solution ionic strength and viscoelasticity, although changes in solution or surface properties may generate modest changes in dynamics.

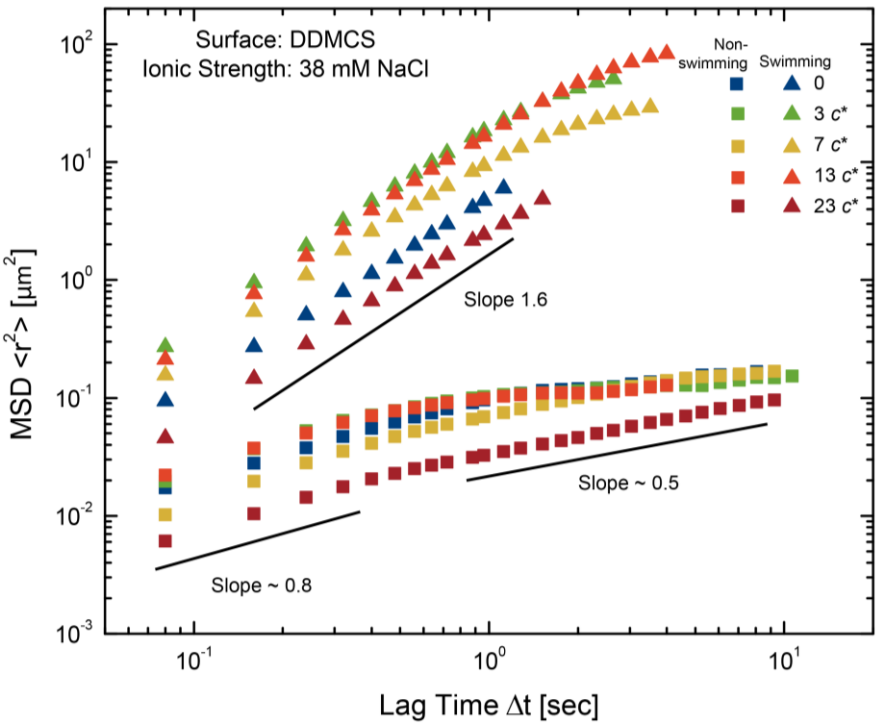

Figure 4.9. Representative ensemble-averaged MSD as a function of lag time for *E. coli* on DDMCS surface at a solution ionic strength of 38 mM and for varying xanthan gum concentration from 0 – 23*c**. Squares indicate the non-swimming cells and triangles indicate swimming cells.

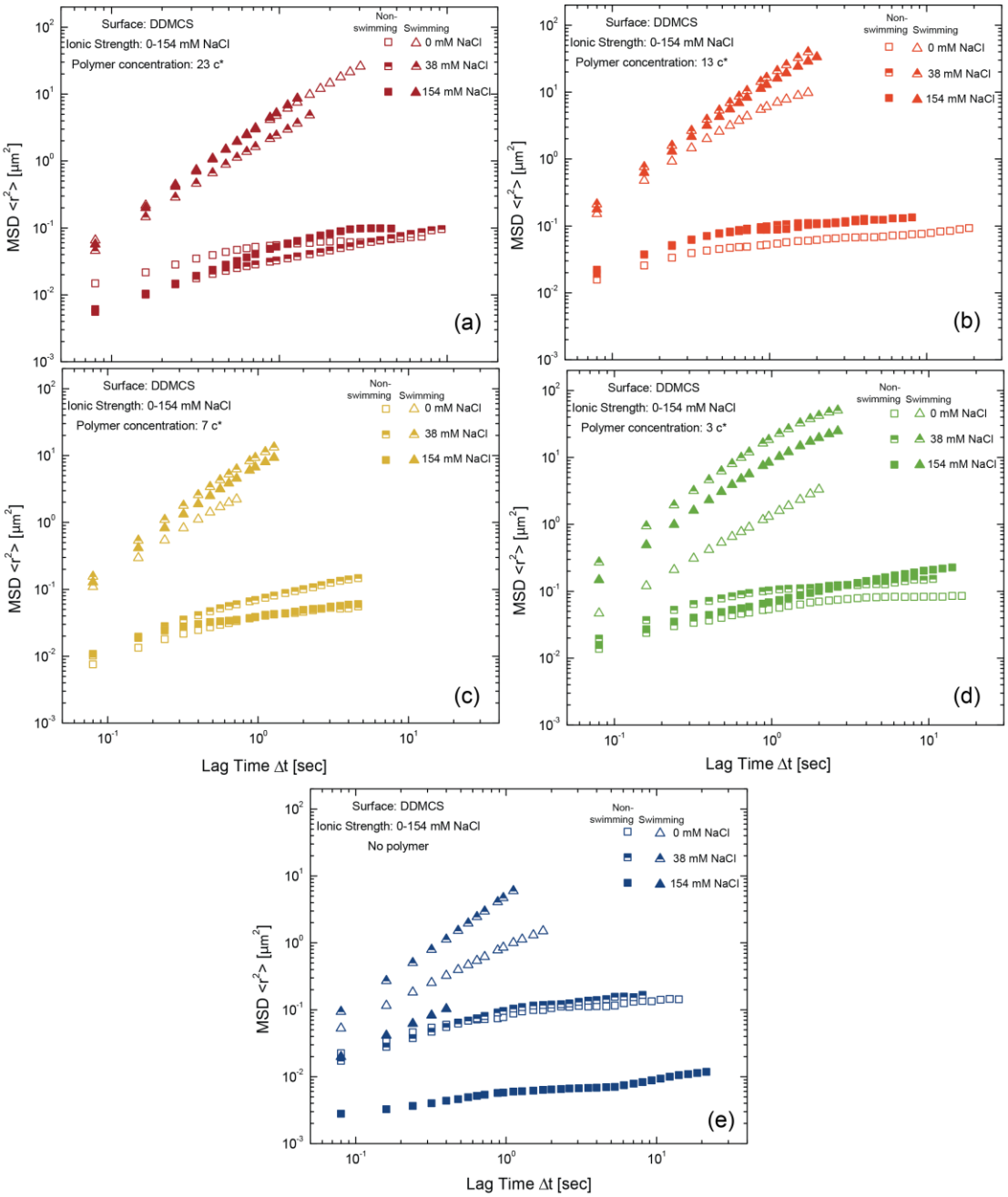

Figure 4.10. MSD for *E. coli* on DDMCS surface as a function of lag time for solutions of polymer concentration (a) 23*c**, (b) 13*c**, (c) 7*c**, (d) 3*c**, and (e) no polymer; and varying ionic strength (IS). Filled symbols indicate IS = 154 mM, half-filled symbols indicate 38 mM and open symbols indicate 0 mM IS.

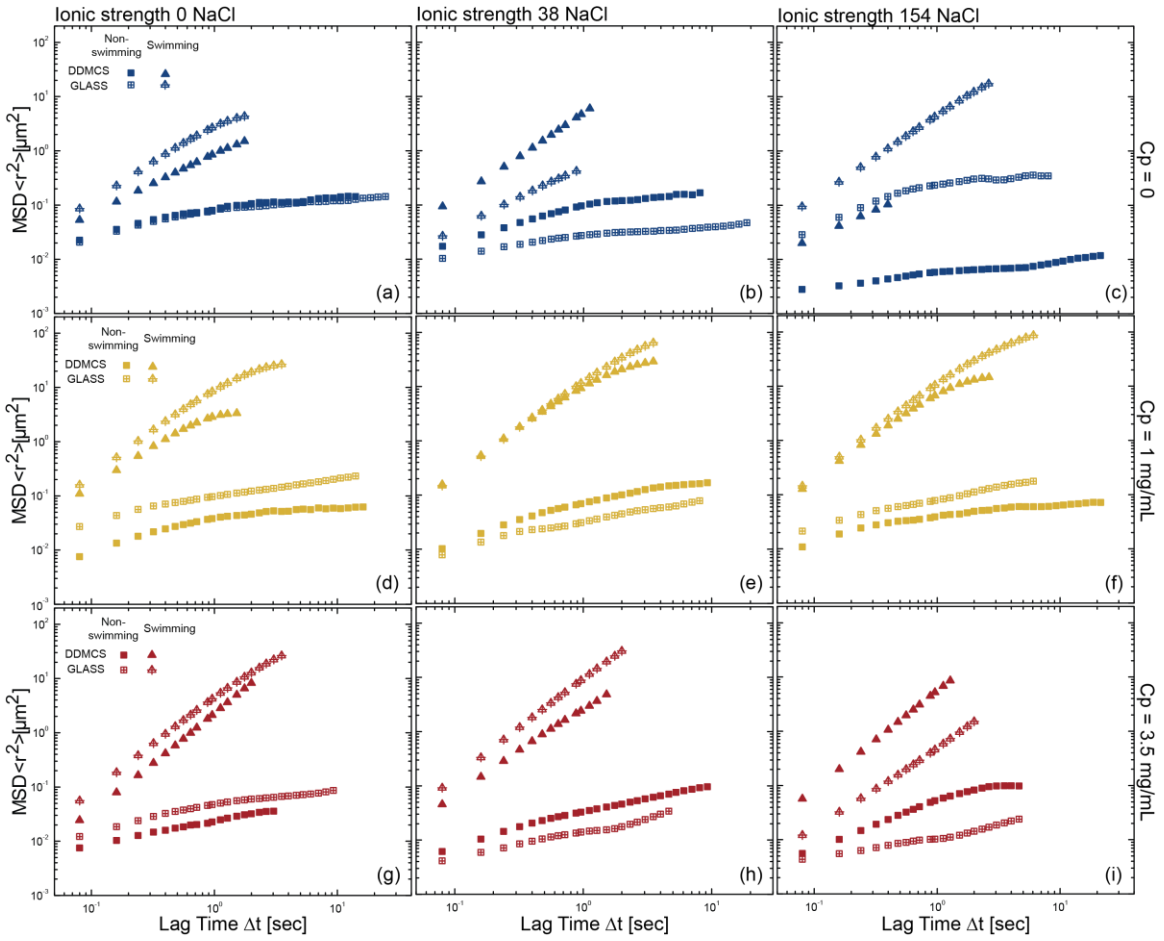

Figure 4.11. MSD as a function of lag time near DDMCS (solid symbols) and glass (empty crossed symbols) surfaces at solution ionic strength 0-154 mM NaCl and polymer concentrations, Cp (a-c) 0 (blue), (d-f) 7*c** (yellow), and (g-i) 23*c** (red). Squares indicate non-swimming cells and triangles indicate swimming cells.

Next, we quantify the fraction of cells that swim or not-swim on each surface at varying ionic strength and polymer concentrations. On glass, the fraction of cells associating with the surface and swimming (not swimming) first increases (decreases) with increasing polymer concentration up until 13*c** and then decreases (increases) above 13*c** (Figure 4.12 (a) –(c)). We observe no significant difference between the fraction of cells exhibiting the two modes of motion on DDMCS as the ionic strength or polymer

concentration is varied (Figure 4.12 (d) – (f)). Moreover, the fraction of cells exhibiting either modes of motion varied significantly between different DDMCS surfaces resulting in larger errors of measurement for these surfaces as opposed to glass. At low ionic strengths, larger fractions of cells swim in polymer suspensions than in polymer free solutions, whereas at higher ionic strength this difference is not significant likely due to screening of charge interactions between cells and surface.

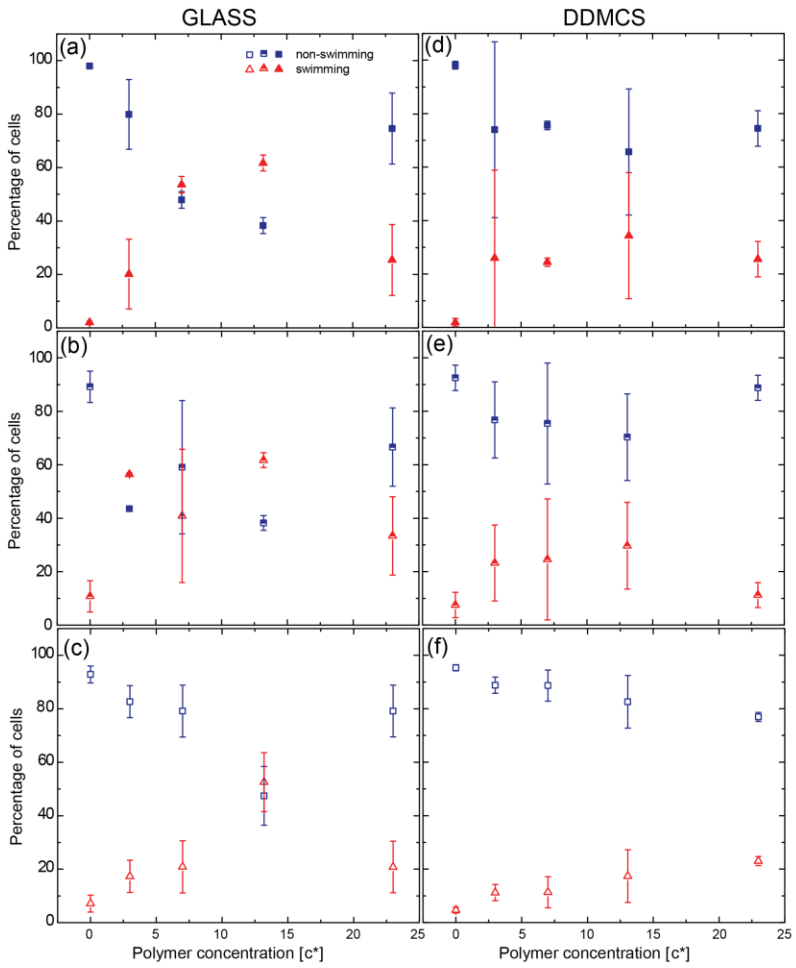

Figure 4.12. Percentage of swimming and non-swimming cells on glass with solution ionic strengths of (a) 0 mM, (b) 38 mM, and (c) 154 mM or on DDMCS with solution ionic strengths of (d) 0 mM, (e) 38 mM, and (f) 154 mM. Filled symbols indicate IS = 154 mM, half-filled symbols indicate 38 mM, and open symbols indicate 0 mM IS.

Polymer additives are known to modify the properties of swimming bacteria,[158, 159] and hence we characterized the effect of polymer concentration on near-surface swimming characteristics. First, we examined the distribution of average swimming speeds. To calculate the average swimming speed, the total displacement of each swimming cell trajectory was divided by the time duration of each trajectory. The average swim speed first increased as polymer was added to the sample suspension, but then decreased beyond when the polymer concentration was increased above 13*c** (Figure 4.13). This result is consistent with the decrease in MSD values observed for samples with the highest polymer concentration (23*c**) (Figure 4.9).

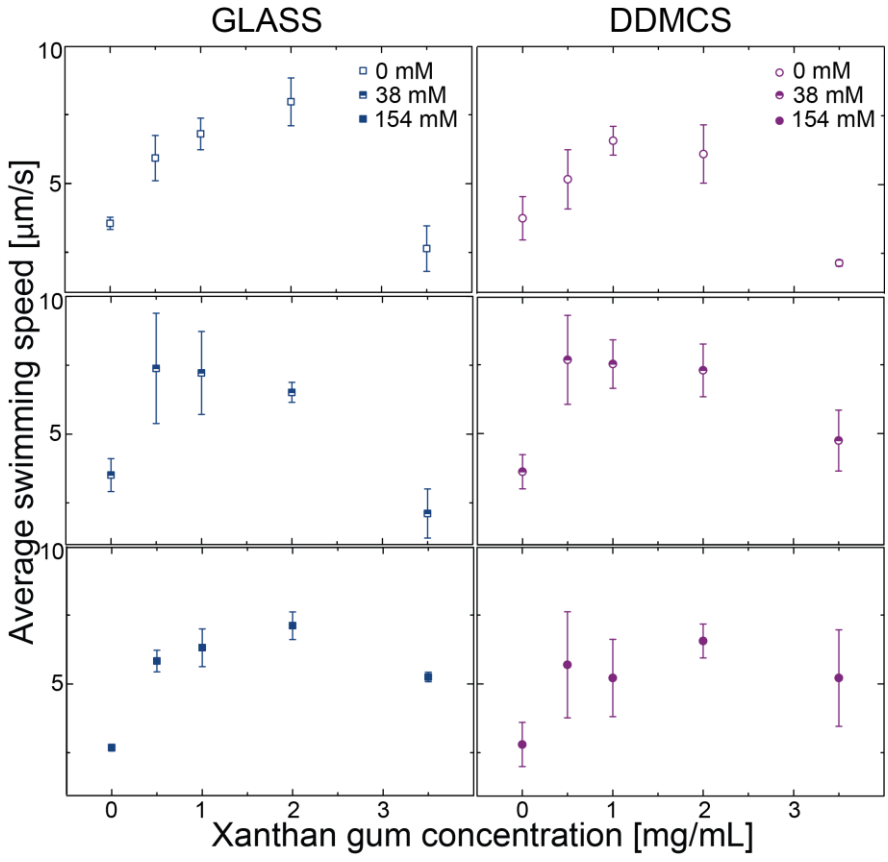

Figure 4.13. Average swimming speed of cells as a function of polymer concentration for (left) Glass surface and (right) DDMCS surfaces. Ionic strength (IS): 154 mM (filled symbols), 38 mM (half-filled symbols), 0 mM (empty symbols).

From the trajectories of swimming cells, we calculated the radius of curvature of the trajectories, as cells near surfaces are known to become hydrodynamically trapped[174] and swim in circular trajectories. The average radius of curvature increased with increasing concentration of polymer and hence with the suspension zero shear viscosity and local shear viscosity (Figure 4.14). The zero-shear viscosity is obtained from the fits to the shear-thinning Carreau-Yasuda model (equation 4.1) to steady state viscosity of polymer solutions as a function of shear rate. We estimate the local viscosity experienced by the bacteria, obtained from the steady-state viscosity at a local shear rate corresponding to the deformation of the polymer. The local shear rate is estimated as

$$\dot{\boldsymbol{\gamma}} = \frac{\boldsymbol{v}_{\mathbf{average}}}{\boldsymbol{b}_{\mathbf{average}}} \quad , \tag{4.2}$$

where, $\dot{\boldsymbol{\gamma}}$ is the shear rate, $\boldsymbol{v}_{\mathbf{average}}$ the average swimming speed of bacteria, and $\boldsymbol{b}_{\mathbf{average}}$ the average length of bacteria. In earlier studies the radius of swimming trajectories has been reported to increase with temperature, size of cells,[33] and distance from the surface.[175] Mathematical models for swimming of bacteria in circles proposed that the local drag coefficient parallel to the local length of cell body is proportional to viscosity of the liquid and that swimming velocity is linearly related to the radius of swimming.[33] We examine the dependence of swimming radius on the swim speed (Figure 4.15) and find that except for the highest polymer concentration 23*c**, the swim radius increases as the speed of swimming cells increases within errors of measurement. We propose that the likely origin of the increase in swim radius is the increase in swimming speed for polymer concentrations less than or equal to 13*c**. At the highest polymer concentration studied, 23*c**, the linear relationship does not hold; this result suggests that

the polymer dynamics and elasticity begin to play a role in modifying the swimming behavior of the bacteria.

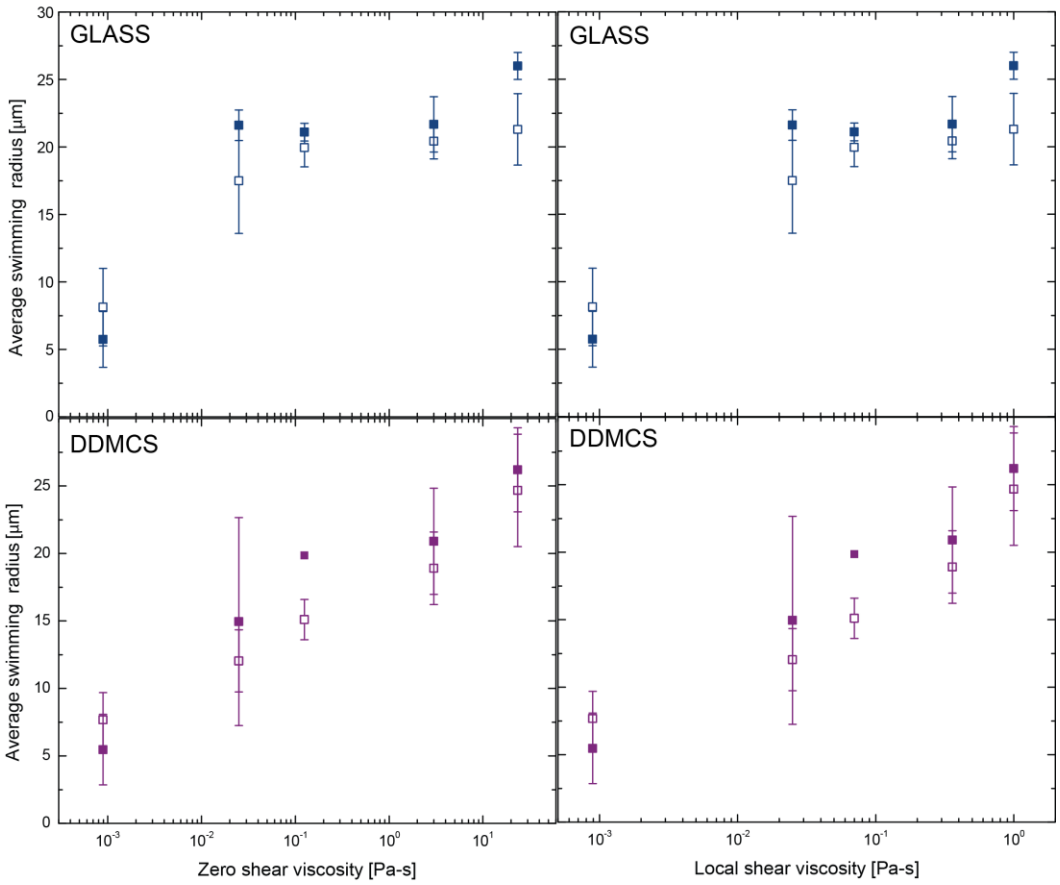

Figure 4.14. Average swim radius of circular trajectories as a function of the solution viscosity (left panel) and local shear viscosity (right panel) for glass (top row) and DDMCS surfaces (bottom row). Filled symbols indicate ionic strength (IS)154 mM and empty symbols indicate 0 mM IS.

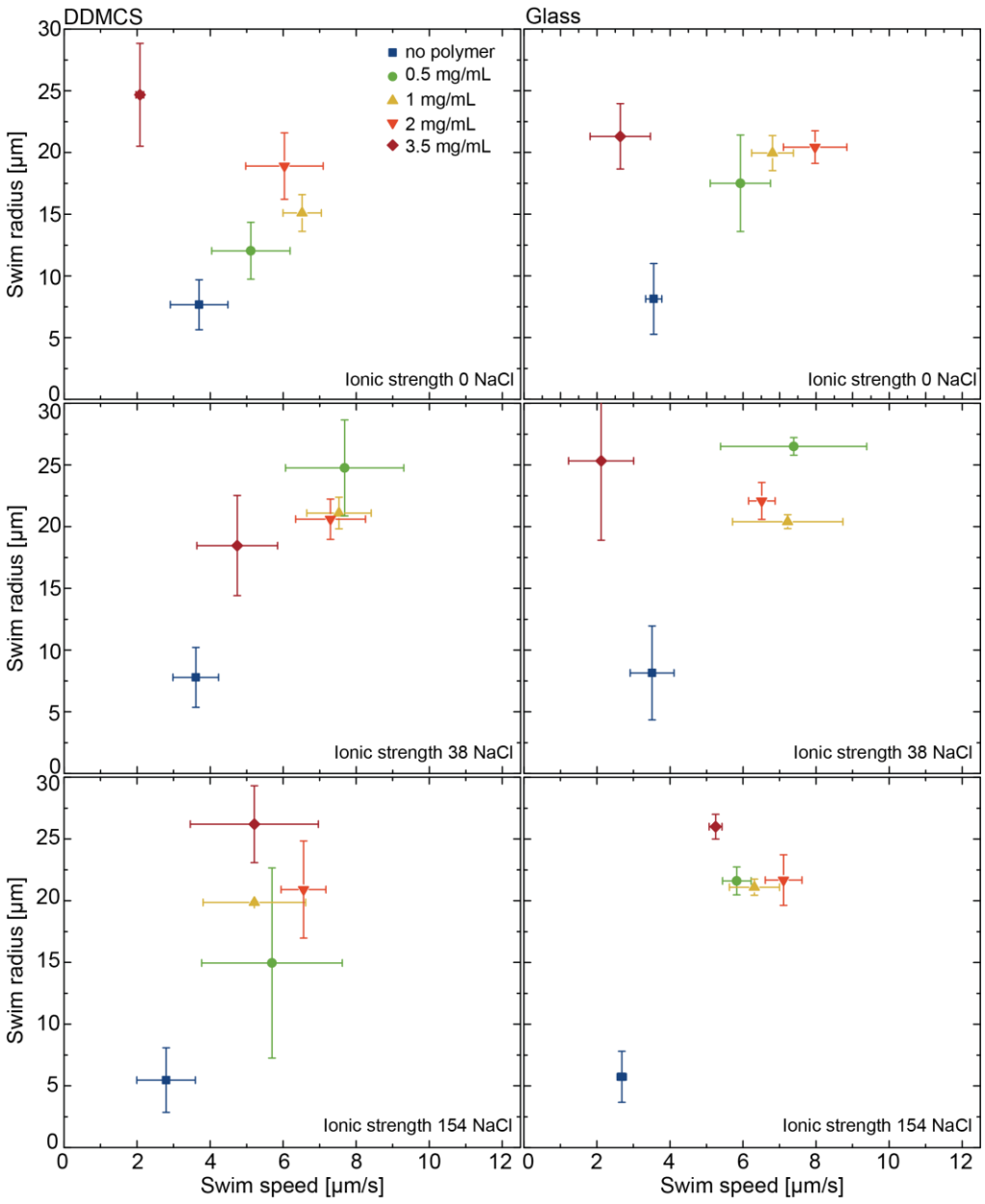

Figure 4.15. Average radius of swimming trajectories as a function of the average swim speed for DDMCS (left panel) and glass (right panel) for all three ionic strengths 0, 38, and 154 mM NaCl.

To understand the origin of the increase of swimming speed with addition of polymer, we first test whether xanthan gum acts as a nutrient source in the system. We incubate the bacteria cells in water and in polymer solutions at 37ºC and with shaking at

200 rpm to aerate the samples. No growth of bacteria is observed in the polymer solutions, confirming that xanthan gum does not provide a nutrient-rich environment for the cells.

The rheology of xanthan gum indicates that the polymer chains are in the semi-dilute unentangled regime below ~8.5c*; at higher concentrations of polymer, the polymer is expected to be in the semi-dilute entangled regime (Figure 4.4). The average swimming speed increases up until a polymer concentration of 13c* but decreases at the highest concentration (23c*). To understand the origin of the increase at low concentrations, we calculate the local shear rate generated by the swimming of bacteria (equation 4.2) and estimate the corresponding local viscosity from the rheology data (Figure 4.2) as shown in Table 4.4. The local viscosities are all greater than that for polymer-free suspensions and change significantly more than the swimming speed. Therefore the enhancement of swim speeds in these polymer suspensions cannot be directly attributed to local shear thinning. Earlier reports on enhancement of swimming speeds in polymer solution instead attributed this enhancement to fluid elasticity and showed that local flow generated by swimming *E. coli* cells stretches the polymer molecules, inducing elastic stresses that can enhance cell motion.[159] We therefore suggest that the increase in swim speeds at low but nonzero polymer concentration (3 – 13c*) can be attributed to a combination of local shear thinning coupled with polymer dynamics. Second, we propose that the decreased mobility of bacteria at 23c* occurs due to polymer entanglements, resulting in caging of the bacteria. This caging cannot be simply due to proximity of the polymer chains, as the correlation length for the polymer at all

concentrations (estimated from scaling relationships in (Table 4.5)) is always smaller than the characteristic length of the bacteria.

Table 4.4. Local shear viscosity for solutions of each polymer concentration.

Polymer concentration [c/c*]	Local viscosity [Pa-s]
3	0.025
7	0.07
13	0.36
23	1

Table 4.5. Polymer correlation length estimated for xanthan gum of radius of gyration R_g ~ 264 nm over the range of polymer concentrations used in experiments.

Polymer concentration [c/c*]	Polymer correlation length [nm]
3	106
7	62
13	37
23	24

Further support for the idea that entanglement-induced caging affects the swimming bacteria in concentrated polymer solutions is provided by the observation of reversals in the trajectories of swimming bacteria. Typical cell trajectories exhibiting reversals are shown in Figure 4.16. In a reversal trajectory, cells appear to encounter a hindrance to motion, and then retrace their trajectory without changing their angular orientation, (i.e., such that the formerly trailing end of the cell becomes the leading end); subsequently, the cell probes another path by reorienting its body axis (i.e. with an angular reorientation such that the formerly leading end resumes the lead). Cells may

undergo multiple reversals in a short period of time until the cell is able to swim smoothly or becomes immobilized. Similar reversals in motion of *Bacillus subtilis* have been reported near a physical obstacle.[176]

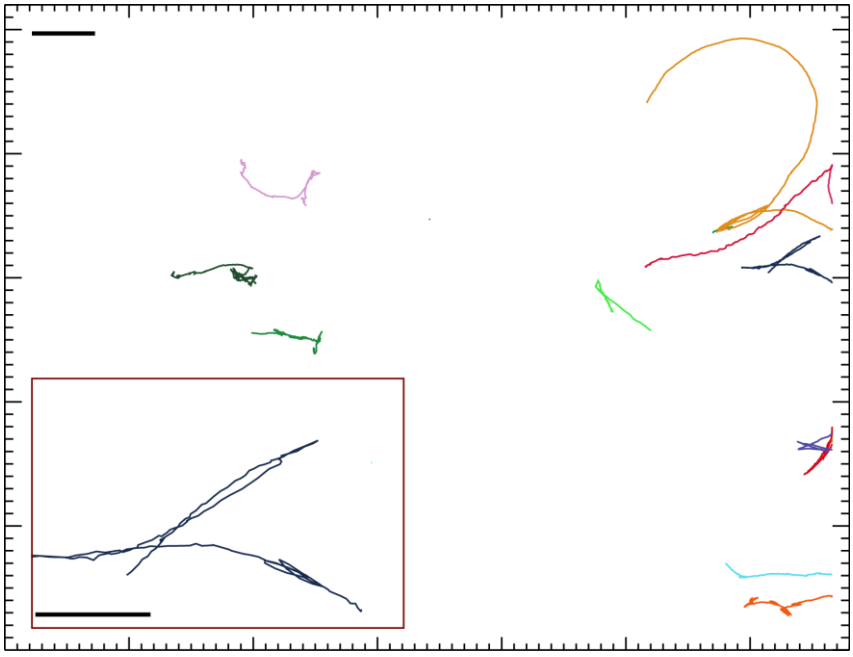

Figure 4.16. Representative trajectories for bacteria showing reversal in a polymer solution of concentration 23c*. Scale bar is 10 µm. Inset shows magnified view of a sample trajectory (scale bar 5 µm).

To identify reversals, we examine the change in velocity angle of bacteria. Smooth swimming cells do not exhibit sharp and large changes in direction of velocity (Figure 4.17 (a)); cells that reverse direction, however, exhibit a rapid change in direction of velocity (θ) by 180º (corresponding to cosθ = -1) (Figure 4.18 (b)). Similarly, we examine the magnitude of velocity as a function of time for trajectories of smooth swimming cells without reversal and for cells that reverse direction. Smooth swimming is characterized by uniform fluctuations of the velocity of the cell about a mean, whereas

rapid acceleration of cells coincides with the time of reversal (Figure 4.18). These metrics allow us to automatically search for reversals in the trajectories of bacteria in a high-throughput fashion.

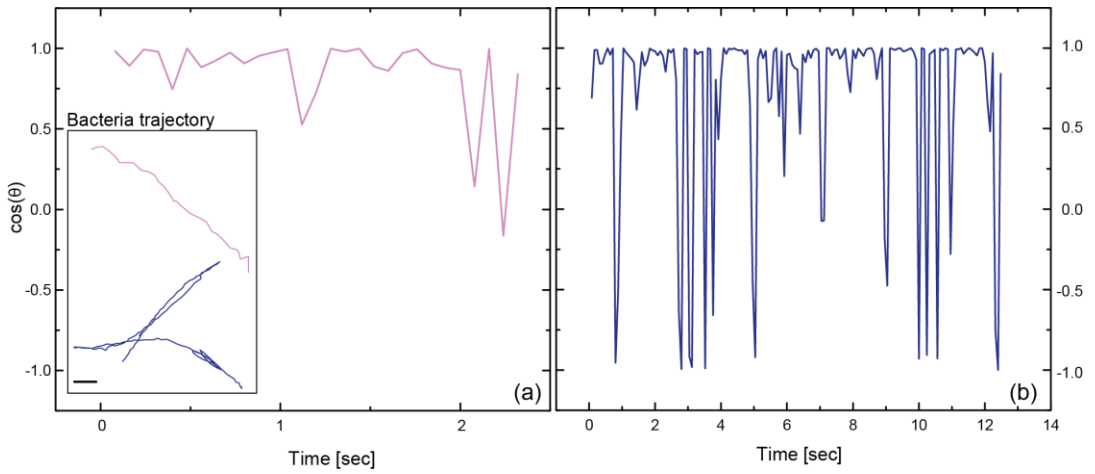

Figure 4.17. Cosine of change in direction of velocity vector cos(θ) for (a) a smooth swimming cell and (b) a cell showing reversal in trajectory. Inset to (a) shows the trajectories of smooth swimming (top) and reversing bacteria (bottom). Scale bar is 2 µm.

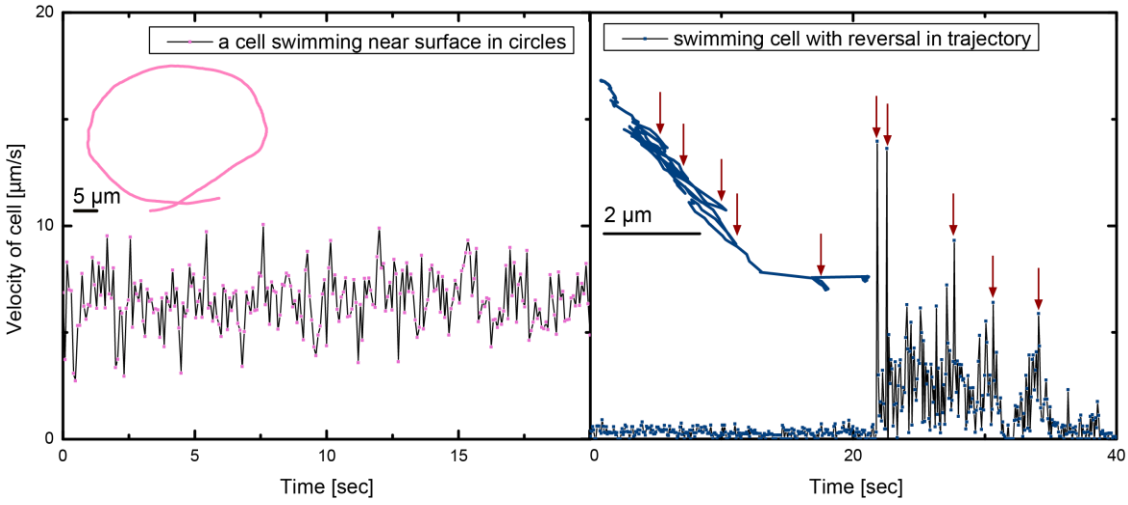

Figure 4.18. Velocity as a function of time for a smooth swimming cell near the surface (left) showing uniform fluctuations about a mean and that for a cell exhibiting reversal without change of orientation (right), showing a large change in velocity at the time of reversal [indicated with red arrows]. Trajectories for each type of motion are shown as insets.

In our experiments, reversals are observed infrequently at 13*c** and more frequently at 23*c**; both solutions are expected to contain entangled polymers. By contrast, we observe no signs of reversals in the trajectories of cells in polymer solutions at 3 and 7*c** nor in the polymer-free solution. Finally, we also observe reversals in bacteria trajectories in bulk (15 μm) above the surface, which implies that the origin of this hindered locomotion is related to polymer concentration and dynamics and not physical interactions with the surface alone. Together, these results suggest that the ability of cells to retrace their paths is related to entanglements.

4.4 Conclusions

We studied the effect of surface hydrophobicity, solution ionic strength, and solution viscosity on the near surface attachment and mobility of *E. coli*. Cells exhibited two distinct modes of motion near surface: (a) surface-associated motion, characterized by near diffusive behavior at short times (MSD slope of 0.8 – 1) and sub-diffusive behavior at long times (MSD slope of 0.4 – 0.5), and (b) near-surface swimming of cells, characterized by near ballistic motion (MSD slope of 1.6 – 1.8). In the absence of polymer, increasing the ionic strength of solution significantly reduced the mobility of swimming cells; in this case charges on the surface were screened so that the cells were more likely to adhere. The fraction of swimming cells varied with polymer concentration near a glass surface but was nearly constant near a DDMCS surface. Mobility of swimming cells on both surfaces increased with addition of polymer up to a concentration of 13*c**, but decreased when the polymer concentration was further

increased to 23c*. Solution ionic strength did not affect the swimming speeds of the cells near either surface in the presence of polymer.

To tentatively explain these initial results, we considered the effects of the polymer at low and high concentrations on the swimming motility of bacteria. At low concentrations, adding polymer increased the swimming speed of cells; this increase likely arose from the combination of local shear thinning of the polymer solution and elasticity of polymer. At the highest concentrations, adding polymer reduced the mobility of swimming cells. We attributed this decrease to increased entanglements in the polymer solution which hindered the motion of the bacteria. In further support of this idea, we observed that swimming bacteria often reversed direction at the highest polymer concentration, as observed previously in vicinity of obstacles[176] or in highly constricted environments.[177] In contrast to these earlier observations, however, a reversing bacterium retraced its path upon encountering an obstacle in the polymer network by reversing direction without changing its body axis orientation, then reoriented slightly to probe another direction until it was able to swim smoothly ahead or became immobilized.

Our results suggest that the interplay of surface chemistry, solution chemistry and viscoelasticity affects the extent to which bacteria adhered to surfaces or were able to swim near them. Changes in mobility due to increased ionic strength were pronounced only in the absence of polymer. Furthermore, the fraction of cells that swim or adhere on surface depended on the surface chemistry as well as polymer concentration. Finally, interactions between swimming cells and polymers significantly altered the speed and hence the amount of time that cells spend in close proximity to the surface. This result is significant because increasing the near-surface residence time affects the likelihood that

bacteria accumulate on the surface, and hence affects the subsequent biofilm formation. We expect that improved understanding of near-surface mobility of bacteria in a model heterogeneous system will lead to improved strategies for controlling adhesion in practical environments often encountered in both medicine and industry.

Chapter 5 Conclusions and recommendations for future work

5.1 Summary

In this study we investigated the attachment, surface-associated and near-surface behavior of *Escherichia coli* on silanized glass surfaces. We characterized the near surface-associated behavior of cells to obtain mechanistic insight into bacterial adhesion and towards the larger goal of developing a fundamental understanding of bacteria-surface interactions for rational design of surfaces to control bacterial attachment and hence biofouling. Specifically, we designed experiments to study the role of surface chemistry, roughness, shear stress from flow, and combined effect surface chemistry with solution ionic strength and viscosity in initial adhesion and near surface mobility of attaching bacteria.

In the first part, we investigated the transition from initial transient to irreversible attachment of *E. coli* deposited from flow onto surfaces of controlled chemistry created by self-assembly of organosilanes on glass. We employed high throughput bacteria tracking and analysis tools to analyze the dynamic adhesion events for hundreds of bacteria on each surface. We found that the rate at which bacteria were deposited showed poor and non-monotonic correlation with conventional metrics to characterize surfaces, such as surface wettability and energy. Instead, the deposition rate was inversely correlated with the degree of surface-attached flagella-driven motion. We posit that flagella mediates transient bacterial attachment to surface; the fate of initial transient attachment is ultimately determined by physicochemical interactions (electrostatic or van der Waals) between bacteria and surfaces. Moreover, the transition from transient to

immobilized (likely irreversible) attachment is also correlated with short-time deposition rate. Our results suggest that the techniques and methods to characterize transient surface motility presented in this study can potentially serve as a serve as a metric to rapidly determine the efficacy of surfaces to reduce fouling by bacteria. This rapid high throughput assay can and thereby speed the design of improved antifouling materials for medical, technological, and environmental applications.

In the second part of our work, we characterized near-surface motility associated with adhesion in *E. coli* bacteria deposited from flow on glass substrates bearing self-assembled alkylsilane and fluoroalkylsilane films. We found that the deposition rate for all surfaces generally decreased with increasing shear stress and increased approximately linearly with the RMS surface roughness. Consistent with greater cell adhesion to the rougher surfaces, the extent of surface-associated motion decreased with RMS roughness. Cells exhibited mobile adhesion on very smooth surfaces undergoing large linear displacements. As shear stress was increased, the speed of mobile adhesion decreased and residence time of cells increased. We found that mobile adhesion did not involve specific interactions between bacterial adhesins and the surface. Instead, only cells that did not express fimbriae exhibited mobile adhesion. Mobile adhesion required very smooth surfaces as well as absence of the adhesive fimbriae. Since this form of surface-associated behavior reflects reduced friction between cells and surfaces hence we posit that it arises from a physical origin rather than known modes of motility which are driven directly by appendages[33, 146] or indirectly by specific interactions.[26, 60] Consistent with earlier studies for colloid deposition in heterogeneous surface environments, [138] we found

that surface roughness (i.e. heterogeneity in surface topography) determines the transition from mobile to immobile adhesion for bacteria suggesting that strategies to reduce frictional interactions between cells and surfaces, either by engineering nanoscale-smooth surfaces or by suppressing expression of cell surface adhesins, may help to reduce fouling during initial deposition.

In the third part of our work, we examined the effect of crowding due to addition of polymer on near surface behavior of cells in a quiescent environment on hydrophilic glass and hydrophobic silanized glass surface under conditions of varying suspension ionic strength. We sorted the near-surface behavior of cells under these conditions can be into swimming and non-swimming modes based on their maximum displacement. We characterized the dynamics of each population of cells and find that the swimming cells show near ballistic motion; and the non-swimming cells show near diffusive behavior at short and sub-diffusive behavior at long times. Of the three variables in the system: ionic strength, surface chemistry, and polymer concentration, the last had most pronounced effect on dynamics and average speeds of swimming cells. Interestingly, we also found that bacteria show reversal of trajectory without changing direction and seek alternate routes for translational motion in high concentration xanthan gum solutions. Based on these results we suggest that characterizing the rheological properties of ambient environment is more vital to effective design of surfaces for applications such as medical implants, sensors in oil exploration etc. where highly bacterial attachment occurs under moderate to highly viscous and Newtonian to highly non-Newtonian environments.

5.2 Recommendations for future work

Based on the findings from the present study, the following recommendations are proposed for future work:

5.2.1 Origin of shear enhanced residence time

The study of mobile adhesion of *E.coli* on nano-smooth silanized surfaces revealed that residence time increased along with shear stress, especially for cells in mobile adhesion. Neither surface property roughness nor cell-surface characteristics (specifically, presence or absence of fimbriae, and/or flagella) in mobile adhesion is able to explain this enhancement of residence time.

It is therefore proposed to understand the origin of shear enhancement of residence time using a bi-faceted approach. Specifically the following hypotheses to be tested are proposed:

5.2.1.1 Hypothesis 1

Enhancement of residence time for mobile adhering cells on sub-nanoscale smooth surfaces is mediated by shear stress and force on adhering cells rather than shear rate and kinetic effects. To test this hypothesis the following approach is proposed:

(a) Image the deposition of bacteria on the surfaces exhibiting mobile adhesion (DTS and FDTS) at the same shear stresses (3, 22, and 67 mPa) but at varying shear rates by varying the suspension viscosity through addition of modifiers such as Ficoll, which at low concentrations is not toxic to the bacteria.

(b) Compare the rate of deposition and residence times as a function of shear stress and shear rates for the two sets of experiments in 154 mM NaCl solution and in a Ficoll suspension. This comparison determine whether the increased residence times are a result

of shear stress (and hence of the effective force acting on cells) or whether it is a shear rate (and hence a kinetic effect) that underlies the shear dependence of adhesion.

5.2.1.2 Hypothesis 2

It is proposed to test the hypothesis that enhancement in residence time is a result of effective force on cells and not due to the effect of cell surface structures. The time scale of the experiments done to study mobile adhesion of bacteria is sufficiently short so as to eliminate any role of exo-polysaccharides in enhancement of mobile adhesion. We have already tested that bacterial flagella and fimbriae do not play a role in shear enhanced residence time. Besides flagella and fimbriae, curli[178] and lipopolysaccharides (LPS)[179] are major bacterial appendages implicated in bacterial attachment to surfaces and considered important in virulence and pathogenesis in many bacteria including *E. coli*. TEM imaging of MC1061, BW25113 and its mutants, and MG1655 and its mutants, did not show any expression of curli on these bacterial strains under the culture conditions used for the experiment. The imaging protocol used in this study (Chapter 3), however, does not allow for visualization of LPS. To test the hypothesis by determining the effect of other cell surface organelles such as lipopolysaccharides, the following approach is proposed:

(a) Confirm whether the strains used in this study: MC1061, MG1655, BW25113, JW1908; and JW4277 express lipopolysaccharides (LPS). It is proposed to use either a LPS extraction technique [180] or freeze-substitution for visualizing the LPS chains[181] for this test.

(b) If the strains are found to express LPS, it is proposed to understand the role of LPS in the shear-mediated dependence of mobile adhesion and residence time by studying LPS deficient mutants of *E. coli* in deposition experiments under the conditions described in Chapter 3.

5.2.2 Origin of electrostatic interaction with cationic surfaces

Study of bacterial adhesion on silanized glass of varying surface chemistry (Chapter 2) revealed that surface-associated motion is a potential metric for distinguishing the antifouling efficacy of test surfaces. Based on the nature of surface-associated motion, we proposed that flagella plays a key role in mediating initial attachment on GPTS, ODMCS, OTS and Plasma treated glass surfaces. Surface-associated motion is not the suitable metric in determining the origin of strong electrostatic interactions observed on APTES and APTMS leading to immobilization of cells. These motility based metrics, therefore, do not provide information on whether the interaction of cell-surface protein or flagellar protein is responsible for the electrostatic interaction on cationic surfaces.

5.2.2.1 Hypothesis to be tested

Bacterial adhesion on cationic surfaces is mediated by electrostatic interaction with bacterial flagella. Following approach is outlined for testing above hypothesis:

(a) Flow experiments should be done at a fixed shear stress on a cationic surface such as APDMES (aminopropyldimethylethoxy silane) that allows formation of monolayers on glass using *E. coli* strains that are wild type (expressing both fimbriae and flagella), and its isogenic mutants deficient in fimbriae, flagella and both. By quantifying the extent of immobilized adhesion seen on the cationic surface with each of these strains, we can

identify whether the surface electrostatic interaction is with the cell surface, flagellar protein, or the fimbriae.

(b) Preliminary experiments done in collaboration with Dr. D. Velegol (Pennsylvania State University) for *E. coli* BW25113 and JW4277 suggest that charge distribution present on *E. coli* can be quantified using charge non-uniformity light scattering. [182] Estimation of charge distribution on wild type cells and the flagella and fimbriae deficient mutants will help to verify the results obtained from flow experiments.

(c) Control experiments for this test are proposed to be run on a neutral silane monolayer such as GPDMES (glycydoxypropyldimethylethoxy silane). Together, these experiments will allow us to distinguish the role of specific surface adhesins in mediating electrostatic interaction with a cationic surface.

5.2.3 Understanding near surface mobility of bacteria on silanized glass surface in non-Newtonian media

The study of near surface motion and dynamics of *E. coli* (Chapter 4) opens up new routes to investigate the effects of crowding in deposition of bacteria from flow. The results presented so far are from a quiescent study of bacterial suspension on hydrophilic and hydrophobic surfaces under varying ionic strength and polymer concentrations. These experiments were not able to generate information on effect of shear stress alongside the heterogeneity of the system. In practical environments, bacteria encounter environments ranging from moderate to high viscosity and fluids ranging from Newtonian to highly non-Newtonian in nature. In most natural and industrial settings attachment of bacteria occurs from flow. Therefore it is of interest to study the

attachment behavior of bacteria under non-Newtonian environment from flow. Following hypothesis is proposed to be tested –

5.2.3.1 Hypothesis to be tested

Deposition of bacteria from flow on silanized glass depends on solution viscosity and rheology. Following approach is outlined for testing the hypothesis:

(a) Flow experiments of bacterial suspensions in presence of xanthan gum as viscosity modifier and crowding agent will generate data for deposition rates and detachment behavior (if any) under these conditions.

Preliminary experiments done on DDMCS under flow conditions (22 mPa shear stress) with bacterial suspension in 1 mg/mL xanthan gum in 154 mM NaCl show very different behavior of adhering cells compared to earlier experiments on a surface of similar chemistry (DTS) at the same suspension ionic strength (154 mM NaCl) but without polymer. In addition to immobile surface-associated motion and mobile adhesion (c.f. Chapters 2 and 3), we observe that a fraction of cells exhibit motion and/or mobile adhesion in the direction opposing that of flow.

(b) To understand the mechanism of near surface rheotaxis, deposition experiments should be conducted by varying polymer concentrations over dilute ($< c^*$), semi-dilute unentangled ($> c^*$ and $< 8c^*$ for xanthan gum) and semi-dilute entangled solutions ($> 8c^*$ for xanthan gum). Corresponding experiments on appropriate controls such as clean glass are proposed to substantiate that solution viscosity and not surface chemistry play the significant role in observed rheotaxis. It is expected that these deposition experiments from flow will help identify features of surface adhesion that will impact understanding of bacterial adhesion in non-Newtonian environment.

References

1. Konstantinou, I. K.; Albanis, T. A. Worldwide Occurrence and Effects of Antifouling Paint Booster Biocides in the Aquatic Environment: A Review. *Environment International* **2004**, *30*, 235-248.

2. Sun, J.; Deng, Z.; Yan, A. Bacterial Multidrug Efflux Pumps: Mechanisms, Physiology and Pharmacological Exploitations. *Biochemical and Biophysical Research Communications* **2014**, *453*, 254-267.

3. Costerton, J. W.; Stewart, P. S.; Greenberg, E. P. Bacterial Biofilms: A Common Cause of Persistent Infections. *Science* **1999**, *284*, 1318-1322.

4. Hall-Stoodley, L.; Costerton, J. W.; Stoodley, P. Bacterial Biofilms: From the Natural Environment to Infectious Diseases. *Nature Reviews Microbiology* **2004**, *2*, 95-108.

5. Bryers, J. D. Medical Biofilms. *Biotechnology and Bioengineering* **2008**, *100*, 1-18.

6. Verran, J. Fouling, Cleaning and Disinfectionbiofouling in Food Processing: Biofilm or Biotransfer Potential? *Food and Bioproducts Processing* **2002**, *80*, 292-298.

7. Nguyen, T.; Roddick, F.; Fan, L. Biofouling of Water Treatment Membranes: A Review of the Underlying Causes, Monitoring Techniques and Control Measures. *Membranes* **2012**, *2*, 804.

8. Shafiqur, R.; Luai, M. A.-H. Web-Based National Corrosion Cost Inventory System for Saudi Arabia. *Anti-Corrosion Methods and Materials* **2014**, *61*, 72-92.

9. Melo, L. F.; Pinheiro, M. M. Biofouling in Heat Exchangers. In *Biofilms — Science and Technology*, Melo, L. F.; Bott, T. R.; Fletcher, M.; Capdeville, B., Eds.; Springer Netherlands: Dordrecht, 1992, pp 499-509.

10. Schultz, M.; Swain, G. The Influence of Biofilms on Skin Friction Drag. *Biofouling* **2000**, *15*, 129-139.

11. García, C.; Moreno, D. A.; Ballester, A.; Blázquez, M. L.; González, F. Bioremediation of an Industrial Acid Mine Water by Metal-Tolerant Sulphate-Reducing Bacteria. *Minerals Engineering* **2001**, *14*, 997-1008.

12. Bouwer, E. J.; Zehnder, A. J. B. Bioremediation of Organic Compounds - Putting Microbial Metabolism to Work. *Trends in Biotechnology* **1993**, *11*, 360-367.

13. Singh, R.; Paul, D.; Jain, R. K. Biofilms: Implications in Bioremediation. *Trends Microbiol.* **2006**, *14*, 389-397.

14. Pearce, C. I.; Lloyd, J. R.; Guthrie, J. T. The Removal of Colour from Textile Wastewater Using Whole Bacterial Cells: A Review. *Dyes and Pigments* **2003**, *58*, 179-196.

15. Busscher, H. J.; van der Mei, H. C. Physico-Chemical Interactions in Initial Microbial Adhesion and Relevance for Biofilm Formation. *Advances in Dental Research* **1997**, *11*, 24-32.

16. Reshes, G.; Vanounou, S.; Fishov, I.; Feingold, M. Cell Shape Dynamics in Escherichia Coli. *Biophysical Journal* **2008**, *94*, 251-264.

17. Absolom, D. R.; Lamberti, F. V.; Policova, Z.; Zingg, W.; van Oss, C. J.; Neumann, A. W. Surface Thermodynamics of Bacterial Adhesion. *Applied and Environmental Microbiology* **1983**, *46*, 90-97.

18. Busscher, H. J.; Weerkamp, A. H.; van der Mei, H. C.; van Pelt, A. W. J.; de Jong, H. P.; Arends, J. Measurement of the Surface Free Energy of Bacterial Cell Surfaces and Its Relevance for Adhesion. *Applied and Environmental Microbiology* **1984**, *48*, 980-983.

19. Marshall, K. C.; Stout, R.; Mitchell, R. Mechanism of the Initial Events in the Sorption of Marine Bacteria to Surfaces. *Journal of General Microbiology* **1971**, *68*, 337-348.

20. van Loosdrecht, M. C. M.; Lyklema, J.; Norde, W.; Zehnder, A. J. B. Bacterial Adhesion - a Physicochemical Approach. *Microbial Ecology* **1989**, *17*, 1-15.

21. Wood, J.; Sharma, R. How Long Is the Long-Range Hydrophobic Attraction? *Langmuir* **1995**, *11*, 4797-4802.

22. Elimelech, M.; O'Melia, C. R. *Langmuir* **1990**, *6*, 1153.

23. Burrows, L. L. Pseudomonas Aeruginosa Twitching Motility: Type Iv Pili in Action. *Annual Review Of Microbiology* **2012**, *66*, 493-520.

24. Diaz, C.; Schilardi, P. L.; Salvarezza, R. C.; Fernandez Lorenzo de Mele, M. A. Have Flagella a Preferred Orientation During Early Stages of Biofilm Formation?: Afm Study Using Patterned Substrates. *Colloids and Surfaces B: Biointerfaces* **2011**, *82*, 536-542.

25. Friedlander, R. S.; Vlamakis, H.; Kim, P.; Khan, M.; Kolter, R.; Aizenberg, J. Bacterial Flagella Explore Microscale Hummocks and Hollows to Increase Adhesion. *Proceedings of the National Academy of Sciences of the United States of America* **2013**, *110*, 5624-5629.

26. Forero, M.; Thomas, W.; Bland, C.; Nilsson, L. M.; Sokurenko, E. V.; Vogel, V. A Catch-Bond Based Nanoadhesive Sensitive to Shear Stress. *Nano Letters* **2004**, *4*, 1593-1597.

27. Rodrigues, D. F.; Elimelech, M. Role of Type 1 Fimbriae and Mannose in the Development of Escherichia Coli K12 Biofilm: From Initial Cell Adhesion to Biofilm Formation. *Biofouling* **2009**, *25*, 401-411.

28. Walker, S. L.; Redman, J. A.; Elimelech, M. Role of Cell Surface Lipopolysaccharides in Escherichia Coli K12 Adhesion and Transport. *Langmuir* **2004**, *20*, 7736-7746.

29. Kim, H. N.; Hong, Y.; Lee, I.; Bradford, S. A.; Walker, S. L. Surface Characteristics and Adhesion Behavior of Escherichia Coli O157:H7: Role of Extracellular Macromolecules. *Biomacromolecules* **2009**, *10*, 2556-2564.

30. Zhao, K.; Tseng, B. S.; Beckerman, B.; Jin, F.; Gibiansky, M. L.; Harrison, J. J.; Luijten, E.; Parsek, M. R.; Wong, G. C. L. Psl Trails Guide Exploration and Microcolony Formation in Pseudomonas Aeruginosa Biofilms. *Nature* **2013**, *497*, 388-391.

31. Cooley, B. J.; Thatcher, T. W.; Hashmi, S. M.; L'Her, G.; Le, H. H.; Hurwitz, D. A.; Provenzano, D.; Touhami, A.; Gordon, V. D. The Extracellular Polysaccharide Pel Makes the Attachment of P. Aeruginosa to Surfaces Symmetric and Short-Ranged. *Soft Matter* **2013**, *9*, 3871-3876.

32. Hori, K.; Matsumoto, S. Bacterial Adhesion: From Mechanism to Control. *Biochemical Engineering Journal* **2010**, *48*, 424-434.

33. Lauga, E.; DiLuzio, W. R.; Whitesides, G. M.; Stone, H. A. Swimming in Circles: Motion of Bacteria near Solid Boundaries. *Biophysical Journal* **2006**, *90*, 400-412.

34. Hill, J.; Kalkanci, O.; Mcmurry, J. L.; Koser, H. Hydrodynamic Surface Interactions Enable Escherichia Coli to Seek Efficient Routes to Swim Upstream. *Physical Review Letters* **2007**, *98*, 068101.

35. Wang, H.; Sodagari, M.; Ju, L. K.; Newby, B. Z. Effects of Shear on Initial Bacterial Attachment in Slow Flowing Systems. *Colloids and Surfaces B: Biointerfaces* **2013**, *109*, 32-39.

36. Vigeant, M. A. S.; Ford, R. M. Interactions between Motile Escherichia Coli and Glass in Media with Various Ionic Strengths, as Observed with a Three-Dimensional-Tracking Microscope. *Applied and Environmental Microbiology* **1997**, *63*, 3474-3479.

37. Olsson, A. L. J.; Arun, N.; Kanger, J. S.; Busscher, H. J.; Ivanov, I. E.; Camesano, T. A.; Chen, Y.; Johannsmann, D.; Van Der Mei, H. C.; Sharma, P. K. The Influence of Ionic Strength on the Adhesive Bond Stiffness of Oral Streptococci Possessing Different Surface Appendages as Probed Using Afm and Qcm-D. *Soft Matter* **2012**, *8*, 9870-9876.

38. Kim, H.; Walker, S. Escherichia Coli Transport in Porous Media: Influence of Cell Strain, Solution Chemistry, and Temperature. *Colloids and Surfaces B: Biointerfaces* **2009**, *71*, 160-167.

39. van Merode, A. E. J.; Pothoven, D. C.; van der Mei, H. C.; Busscher, H. J.; Krom, B. P. Surface Charge Influences Enterococcal Prevalence in Mixed-Species Biofilms. *Journal of Applied Microbiology* **2007**, *102*, 1254-1260.

40. Ojeda, J. J.; Romero-Gonzalez, M. E.; Bachmann, R. T.; Edyvean, R. G. J.; Banwart, S. A. Characterization of the Cell Surface and Cell Wall Chemistry of Drinking Water Bacteria by Combining XPS, FTIR Spectroscopy, Modeling, and Potentiometric Titrations. *Langmuir* **2008**, *24*, 4032-4040.

41. Cunliffe, D.; Smart, C. A.; Alexander, C.; Vulfson, E. N. Bacterial Adhesion at Synthetic Surfaces. *Applied and Environmental Microbiology* **1999**, *65*, 4995-5002.

42. Cerca, N.; Pier, G. B.; Vilanova, M.; Oliveira, R.; Azeredo, J. Quantitative Analysis of Adhesion and Biofilm Formation on Hydrophilic and Hydrophobic Surfaces of Clinical Isolates of Staphylococcus Epidermidis. *Research In Microbiology* **2005**, *156*, 506-514.

43. Pompilio, A.; Piccolomini, R.; Picciani, C.; D'Antonio, D.; Savini, V.; Di Bonaventura, G. Factors Associated with Adherence to and Biofilm Formation on Polystyrene by Stenotrophomonas Maltophilia: The Role of Cell Surface Hydrophobicity and Motility. *FEMS Microbiology Letters* **2008**, *287*, 41-47.

44. Truong, V. K.; Lapovok, R.; Estrin, Y. S.; Rundell, S.; Wang, J. Y.; Fluke, C. J.; Crawford, R. J.; Ivanova, E. P. The Influence of Nano-Scale Surface Roughness on Bacterial Adhesion to Ultrafine-Grained Titanium. *Biomaterials* **2010**, *31*, 3674-3683.

45. Giraldez MJ, R. C., Lira M, Oliveira ME, Magariños B, Toranzo AE, Yebra-Pimentel E. Contact Lens Hydrophobicity and Roughness Effects on Bacterial Adhesion. *Optom Vis Sci*. **2010**, *87*, 426-31.

46. Díaz, C.; Schilardi, P. L.; dos Santos Claro, P. C.; Salvarezza, R. C.; Fernández Lorenzo de Mele, M. A. Submicron Trenches Reduce the *Pseudomonas Fluorescens* Colonization Rate on Solid Surfaces. *ACS Applied Materials & Interfaces* **2009**, *1*, 136-143.

47. Hou, S.; Gu, H.; Smith, C.; Ren, D. Microtopographic Patterns Affect Escherichia Coil Biofilm Formation on Poly(Dimethylsiloxane) Surfaces. *Langmuir* **2011**, *27*, 2686-2691.

48. Meel, C.; Kouzel, N.; Oldewurtel, E. R.; Maier, B. Three-Dimensional Obstacles for Bacterial Surface Motility. *Small* **2012**, *8*, 530-534.

49. Klemm, P.; Schembri, M. A. Bacterial Adhesins: Function and Structure. *International Journal of Medical Microbiology* **2000**, *290*, 27-35.

50. Wood, T. K.; González Barrios, A. F.; Herzberg, M.; Lee, J. Motility Influences Biofilm Architecture in Escherichia Coli. *Applied Microbiology and Biotechnology* **2006**, *72*, 361-367.

51. Gilbert, P.; McBain, A. J. Potential Impact of Increased Use of Biocides in Consumer Products on Prevalence of Antibiotic Resistance. *Clinical Microbiology Reviews* **2003**, *16*, 189-208.

52. Antizar-Ladislao, B. Environmental Levels, Toxicity and Human Exposure to Tributyltin (Tbt)-Contaminated Marine Environment. A Review. *Environment International* **2008**, *34*, 292-308.

53. Conrad, J. C.; Gibiansky, M. L.; Jin, F.; Gordon, V. D.; Motto, D. A.; Mathewson, M. A.; Stopka, W. G.; Zelasko, D. C.; Shrout, J. D.; Wong, G. C. L. Flagella and Pili-Mediated near-Surface Single-Cell Motility Mechanisms in P. Aeruginosa. *Biophysical Journal* **2011**, *100*, 1608-1616.

54. Gibiansky, M. L.; Conrad, J. C.; Jin, F.; Gordon, V. D.; Motto, D. A.; Mathewson, M. A.; Stopka, W. G.; Zelasko, D. C.; Shrout, J. D.; Wong, G. C. L. Bacteria Use Type Iv Pili to Walk Upright and Detach from Surfaces. *Science* **2010**, *330*, 197.

55. Gibiansky, M. L.; Hu, W.; Dahmen, K. A.; Shi, W.; Wong, G. C. L. Earthquake-Like Dynamics in Myxococcus Xanthus Social Motility. *Proceedings of the National Academy of Sciences of the United States of America* **2013**, *110*, 2330-2335.

56. Jin, F.; Conrad, J. C.; Gibiansky, M. L.; Wong, G. C. L. Bacteria Use Type-Iv Pili to Slingshot on Surfaces. *Proceedings of the National Academy of Sciences of the United States of America* **2011**, *108*, 12617-12622.

57. Donlan, R. M. Biofilm Formation: A Clinically Relevant Microbiological Process. *Clinical Infectious Diseases* **2001**, *33*, 1387-1392.

58. Verran, J.; Airey, P.; Packer, A.; Whitehead, K. A. Microbial Retention on Open Food Contact Surfaces and Implications for Food Contamination. *Advances In Applied Microbiology* **2008**, *64*, 223-246.

59. Le Trong, I.; Aprikian, P.; Kidd, B. A.; Forero-Shelton, M.; Tchesnokova, V.; Rajagopal, P.; Rodriguez, V.; Interlandi, G.; Klevit, R.; Vogel, V.; Stenkamp, R. E.; Sokurenko, E. V.; Thomas, W. E. Structural Basis for Mechanical Force Regulation of the Adhesin Fimh Via Finger Trap-Like Beta Sheet Twisting. *Cell* **2010**, *141*, 645-655.

60. Thomas, W. E.; Nilsson, L. M.; Forero, M.; Sokurenko, E. V.; Vogel, V. Shear-Dependent 'Stick-and-Roll' Adhesion of Type 1 Fimbriated *Escherichia Coli*. *Molecular Microbiology* **2004**, *53*, 1545-1557.

61. Ovchinnikova, E. S.; Krom, B. P.; Van Der Mei, H. C.; Busscher, H. J. Force Microscopic and Thermodynamic Analysis of the Adhesion between Pseudomonas Aeruginosa and Candida Albicans. *Soft Matter* **2012**, *8*, 2454.

62. Maier, B. The Bacterial Type Iv Pilus System – a Tunable Molecular Motor. *Soft Matter* **2013**, *9*, 5667-5671.

63. Berg, H. C. *E. Coli in Motion*; Springer 2004.

64. Walker, S. L.; Redman, J. A.; Elimelech, M. Influence of Growth Phase on Bacterial Deposition: Interaction Mechanisms in Packed-Bed Column and Radial

Stagnation Point Flow Systems. *Environmental Science and Technology* **2005**, *39*, 6405-6411.

65. Hunter, R. J. Zeta Potential in Colloid Science, Academic Press, New York. **1981**.

66. Wu, S. Surface and Interfacial Tensions of Polymer Melts. Ii. Poly (Methyl Methacrylate), Poly (N-Butyl Metharylate), and Polystyrene. *Journal of Physical Chemistry* **1970**, *74*, 632-638.

67. Shirley, D. A. High-Resolution X-Ray Photoemission Spectrum of the Valence Bands of Gold. *Physical Review B* **1972**, *5*, 4709.

68. Heydorn, A.; Ersboll, B.; Hentzer, M.; Parsek, M. R.; Givskov, M.; Molin, S. Experimental Reproducibility in Flow-Chamber Biofilms. *Microbiology-Uk* **2000**, *146*, 2409-2415.

69. Mohraz, A.; Solomon, M. J. Direct Visualization of Colloidal Rod Assembly by Confocal Microscopy. *Langmuir* **2005**, *21*, 5298-5306.

70. Toutain, C. M.; Caizza, N. C.; Zegans, M. E.; O'Toole, G. A. Roles for Flagellar Stators in Biofilm Formation by Pseudomonas Aeruginosa. *Research In Microbiology* **2007**, *158*, 471-477.

71. Salerno, M. B.; Logan, B. E.; Velegol, D. Importance of Molecular Details in Predicting Bacterial Adhesion to Hydrophobic Surfaces. *Langmuir* **2004**, *20*, 10625-10629.

72. Frymier, P. D.; Ford, R. M.; Berg, H. C.; Cummings, P. T. Three-Dimensional Tracking of Motile Bacteria near a Solid Planar Surface. *Proceedings of the National Academy of Sciences of the United States of America* **1995**, *92*, 6195-6199.

73. Neuman, K. C.; Chadd, E. H.; Liou, G.; Bergman, K.; Block, S. M. Characterization of Photodamage to Escherichia Coli in Optical Traps. *Biophysical Journal* **1999**, *77*, 2856-2863.

74. Vigeant, M. A. S.; Wagner, M.; Tamm, L. K.; Ford, R. M. Nanometer Distances between Swimming Bacteria and Surfaces Measured by Total Internal Reflection Aqueous Fluorescence Microscopy. *Langmuir* **2001**, *17*, 2235-2242.

75. Anderson, B. N.; Ding, A. M.; Nilsson, L. M.; Kusuma, K.; Tchesnokova, V.; Vogel, V.; Sokurenko, E. V.; Thomas, W. E. Weak Rolling Adhesion Enhances Bacterial Surface Colonization. *Journal Of Bacteriology* **2007**, *189*, 1794-1802.

76. Gottenbos, B.; Grijpma, D.; Van Der Mei, H. C.; Feijen, J.; Busscher, H. J. Antimicrobial Effects of Positively Charged Surfaces on Adhering Gram-Positive and Gram-Negative Bacteria. *Journal Of Antimicrobial Chemotherapy* **2001**, *48*, 7-13.

77. van Oss, C. J.; Good, R. J.; Chaudhury, M. K. The Role of Van Der Waals Forces and Hydrogen Bonds in "Hydrophobic Interactions" between Biopolymers and Low Energy Surfaces. *Journal Of Colloid and Interface Science* **1986**, *111*, 378-390.

78. Wang, H.; Sodagari, M.; Chen, Y.; He, X.; Newby, B. M.; Ju, L. K. Initial Bacterial Attachment in Slow Flowing Systems: Effects of Cell and Substrate Surface Properties. *Colloids and surfaces. B, Biointerfaces* **2011**, *87*, 415-22.

79. van Oss, C. J. Polar or Lewis Acid-Base Interactions. In *Interfacial Forces in Aqueous Media*; Marcel Dekker: New York, 1994, pp 18-46.

80. Acres, R. G.; Ellis, A. V.; Alvino, J.; Lenahan, C. E.; Khodakov, D. A.; Metha, G. F.; Andersson, G. G. Molecular Structure of 3-Aminopropyltriethoxysilane Layers

Formed on Silanol-Terminated Silicon Surfaces. *Journal of Physical Chemistry C* **2012**, *116*, 6289-6297.

81. Vandenberg, E. T.; Bertilsson, L.; Liedberg, B.; Uvdal, K.; Erlandsson, R.; Elwing, H.; Lunström, I. Structure of 3-Aminopropyl Triethoxy Silane on Silicon-Oxide. *Journal Of Colloid and Interface Science* **1991**, *147*, 103-118.

82. O'Hare, L.-A.; Hynes, A.; Alexander, M. R. A Methodology for Curve-Fitting of the Xps Si 2p Core Level from Thin Siloxane Coatings. *Surface and Interface Analysis* **2007**, *39*, 926-936.

83. Petersen, K. E. Dynamic Micromechanics on Silicon: Techniques and Devices. *IEEE Transactions on Electronic Devices* **1978**, *10*, 1241-1250.

84. Bramblett, A. L.; S. Boeckl, M.; Hauch, K. D.; Ratner, B. D.; Sasaki, T.; Rogers, J. W. Determination of Surface Coverage for Tetraphenylporphyrin Monolayers Using Ultraviolet Visible Absorption and X-Ray Photoelectron Spectroscopies. *Surface and Interface Analysis* **2002**, *33*, 506-515.

85. McClaine, J.; Ford, R. M. Reversal of Flagellar Rotation Is Important in Initial Attachment of Escherichia Coli to Glass in a Dynamic System with High- and Low-Ionic-Strength Buffers. *Applied and Environmental Microbiology* **2002**, *68*, 1280-1289.

86. Gomez-Suarez, C.; Pasma, J.; van der Borden, A.; Wingender, J.; Flemming, H.-C.; Busscher, H. J.; Van Der Mei, H. C. Influence of Extracellular Polymeric Substances on Deposition and Redeposition of Pseudomonas Aeruginosa to Surfaces. *Microbiology-Sgm* **2002**, *148*, 1161-1169.

87. Neria-González, I.; Wang, E. T.; Ramírez, F.; Romero, J. M.; Hernández-Rodríguez, C. Characterization of Bacterial Community Associated to Biofilms of Corroded Oil Pipelines from the Southeast of Mexico. *Anaerobe* **2006**, *12*, 122-133.

88. Tribou, M.; Swain, G. The Use of Proactive in-Water Grooming to Improve the Performance of Ship Hull Antifouling Coatings. *Biofouling* **2009**, *26*, 47-56.

89. Chmielewski, R. A. N.; Frank, J. F. Biofilm Formation and Control in Food Processing Facilities. *Compr. Rev. Food Sci. Food Saf.* **2003**, *2*, 22-32.

90. Costerton, J. W. Cystic Fibrosis Pathogenesis and the Role of Biofilms in Persistent Infection. *Trends in Microbiology* **2001**, *9*, 50-52.

91. Bosio, S.; Leekha, S.; Gamb, S. I.; Wright, A. J.; Terrell, C. L.; Miller, D. V. *Mycobacterium Fortuitum* Prosthetic Valve Endocarditis: A Case for the Pathogenetic Role of Biofilms. *Cardiovascular Pathology* **2012**, *21*, 361-364.

92. Von Rosenvinge, E. C.; O'May, G. A.; Macfarlane, S.; Macfarlane, G. T.; Shirtliff, M. E. Microbial Biofilms and Gastrointestinal Diseases. *Pathogens and Disease* **2013**, *67*, 25-38.

93. Van Oss, C. J. The Forces Involved in Bioadhesion to Flat Surfaces and Particles — Their Determination and Relative Roles. *Biofouling* **1991**, *4*, 25-35.

94. Hermansson, M. The Dlvo Theory in Microbial Adhesion. *Colloids and Surfaces B* **1999**, *14*, 105-119.

95. Lund, B.; Lindberg, F.; Marklund, B. I.; Normark, S. The Papg Protein Is the Alpha-D-Galactopyranosyl-(1---4)-Beta-D-Galactopyranose-Binding Adhesin of Uropathogenic *Escherichia Coli*. *Proceedings of the National Academy of Sciences of the United States of America* **1987**, *84*, 5898-5902.

96. Pratt, L. A.; Kolter, R. Genetic Analyses of Bacterial Biofilm Formation. *Current Opinion in Microbiology* **1999**, *2*, 598-603.

97. Van Houdt, R.; Michiels, C. W. Role of Bacterial Cell Surface Structures in *Escherichia Coli* Biofilm Formation. *Research in Microbiology* **2005**, *156*, 626-633.

98. Swartjes, J. J. T. M.; Veeregowda, D. H.; van der Mei, H. C.; Busscher, H. J.; Sharma, P. K. Normally Oriented Adhesion Versus Friction Forces in Bacterial Adhesion to Polymer-Brush Functionalized Surfaces under Fluid Flow. *Advanced Functional Materials* **2014**, *24*, 4435-4441.

99. Harden, V. P.; Harris, J. O. The Isoelectric Point of Bacterial Cells. *Journal of Bacteriology* **1953**, *65*, 198-202.

100. Van Loosdrecht, M. C.; Lyklema, J.; Norde, W.; Schraa, G.; Zehnder, A. J. Electrophoretic Mobility and Hydrophobicity as a Measured to Predict the Initial Steps of Bacterial Adhesion. *Applied and Environmental Microbiology* **1987**, *53*, 1898-1901.

101. Rose, S. F.; Okere, S.; Hanlon, G. W.; Lloyd, A. W.; Lewis, A. L. Bacterial Adhesion to Phosphorylcholine-Based Polymers with Varying Cationic Charge and the Effect of Heparin Pre-Adsorption. *Journal of Materials Science: Materials in Medicine* **2005**, *16*, 1003-1015.

102. Ong, Y.-L.; Razatos, A.; Georgiou, G.; Sharma, M. M. Adhesion Forces between *E. Coli* Bacteria and Biomaterial Surfaces. *Langmuir* **1999**, *15*, 2719-2725.

103. Tuson, H. H.; Weibel, D. B. Bacteria-Surface Interactions. *Soft Matter* **2013**, *9*, 4368-4380.

104. Park, K. D.; Kim, Y. S.; Han, D. K.; Kim, Y. H.; Lee, E. H. B.; Suh, H.; Choi, K. S. Bacterial Adhesion on Peg Modified Polyurethane Surfaces. *Biomaterials* **1998**, *19*, 851-859.

105. Roosjen, A.; de Vries, J.; van der Mei, H. C.; Norde, W.; Busscher, H. J. Stability and Effectiveness against Bacterial Adhesion of Poly(Ethylene Oxide) Coatings in Biological Fluids. *Journal of Biomedical Materials Research Part B: Applied Biomaterials* **2005**, *73*, 347-354.

106. Boks, N. P.; Kaper, H. J.; Norde, W.; Van Der Mei, H. C.; Busscher, H. J. Mobile and Immobile Adhesion of Staphylococcal Strains to Hydrophilic and Hydrophobic Surfaces. *Journal of Colloid and Interface Science* **2009**, *331*, 60-64.

107. Poncin-Epaillard, F.; Herry, J. M.; Marmey, P.; Legeay, G.; Debarnot, D.; Bellon-Fontaine, M. N. Elaboration of Highly Hydrophobic Polymeric Surface — a Potential Strategy to Reduce the Adhesion of Pathogenic Bacteria? *Materials Science and Engineering C* **2013**, *33*, 1152-1161.

108. Taylor, R. L.; Verran, J.; Lees, G. C.; Ward, A. J. P. The Influence of Substratum Topography on Bacterial Adhesion to Polymethyl Methacrylate. *Journal of Materials Science: Materials in Medicine* **1998**, *9*, 17-22.

109. Sousa, C.; Rodrigues, D.; Oliveira, R.; Song, W.; Mano, J. F.; Azeredo, J. Superhydrophobic Poly(L-Lactic Acid) Surface as Potential Bacterial Colonization Substrate. *AMB Express* **2011**, *1*, 1-9.

110. Etxeberria, M.; López-Jiménez, L.; Merlos, A.; Escuín, T.; Viñas, M. Bacterial Adhesion Efficiency on Implant Abutments: A Comparative Study. *International Microbiology* **2013**, *16*, 235-242.

111. Bruinsma, G. M.; Rustema-Abbing, M.; de Vries, J.; Busscher, H. J.; van der Linden, M. L.; Hooymans, J. M. M.; van der Mei, H. C. Multiple Surface Properties of Worn Rgp Lenses and Adhesion of *Pseudomonas Aeruginosa*. *Biomaterials* **2003**, *24*, 1663-1670.

112. Mitik-Dineva, N.; Wang, J.; Mocanasu, R. C.; Stoddart, P. R.; Crawford, R. J.; Ivanova, E. P. Impact of Nano-Topography on Bacterial Attachment. *Biotechnology Journal* **2008**, *3*, 536-544.

113. Yao, C.; Webster, T. J.; Hedrick, M. Decreased Bacteria Density on Nanostructured Polyurethane. *Journal of Biomedical Materials Research Part A* **2014**, *102*, 1823-1828.

114. Ivanova, E. P.; Truong, V. K.; Webb, H. K.; Baulin, V. A.; Wang, J. Y.; Mohammodi, N.; Wang, F.; Fluke, C.; Crawford, R. J. Differential Attraction and Repulsion of *Staphylococcus Aureus* and *Pseudomonas Aeruginosa* on Molecularly Smooth Titanium Films. *Scientific Reports* **2011**, *1*, 165.

115. Thomas, W.; Trintchina, E.; Forero, M.; Vogel, V.; Sokurenko, E. V. Bacterial Adhesion to Target Cells Enhanced by Shear Force. *Cell* **2002**, *109*, 913-923.

116. Thomas, W.; Forero, M.; Yakovenko, O.; Nilsson, L. M.; Vicini, P.; Sokurenko, E. V.; Vogel, V. Catch-Bond Model Derived from Allostery Explains Force-Activated Bacterial Adhesion. *Biophysical Journal* **2006**, *90*, 753-764.

117. Lecuyer, S.; Rusconi, R.; Shen, Y.; Forsyth, A.; Vlamakis, H.; Kolter, R.; Stone, H. A. Shear Stress Increases the Residence Time of Adhesion of *Pseudomonas Aeruginosa*. *Biophysical Journal* **2011**, *100*, 341-350.

118. Busscher, H. J.; Poortinga, A. T.; Bos, R. Lateral and Perpendicular Interaction Forces Involved in Mobile and Immobile Adhesion of Microorganisms on Model Solid Surfaces. *Curr Microbiol* **1998**, *37*, 319-323.

119. Fadeeva, E.; Truong, V. K.; Stiesch, M.; Chichkov, B. N.; Crawford, R. J.; Wang, J.; Ivanova, E. P. Bacterial Retention on Superhydrophobic Titanium Surfaces Fabricated by Femtosecond Laser Ablation. *Langmuir* **2011**, *27*, 3012-3019.

120. Sharma, S.; Conrad, J. C. Attachment from Flow of *Escherichia Coli* Bacteria onto Silanized Glass Substrates. *Langmuir* **2014**, *30*, 11147-11155.

121. Xu, H.; Murdaugh, A. E.; Chen, W.; Aidala, K. E.; Ferguson, M. A.; Spain, E. M.; Núñez, M. E. Characterizing Pilus-Mediated Adhesion of Biofilm-Forming *E. Coli* to Chemically Diverse Surfaces Using Atomic Force Microscopy. *Langmuir* **2013**, *29*, 3000-3011.

122. Baba, T.; Ara, T.; Hasegawa, M.; Takai, Y.; Okumura, Y.; Baba, M.; Datsenko, K. A.; Tomita, M.; Wanner, B. L.; Mori, H. Construction of *Escherichia Coli* K-12 in-Frame, Single-Gene Knockout Mutants: The Keio Collection. *Molecular Systems Biology* **2006**, *2*, 1-11.

123. Tang, S. Y.; Qian, S.; Akinterinwa, O.; Frei, C. S.; Gredell, J. A.; Cirino, P. C. Screening Forenhanced Triacetic Acid Lactone Production by Recombinant *Escherichia Coli* Expressing a Designer Triacetic Acid Lactone Reporter. *Journal of the American Chemical Society* **2013**, *135*, 10099-10103.

124. Tittsler, R. P.; Sandholzer, L. A. The Use of Semi-Solid Agar for the Detection of Bacterial Motility. *Journal of Bacteriology* **1936**, *31*, 575-580.

125. Tchesnokova, V.; Aprikian, P.; Kisiela, D.; Gowey, S.; Korotkova, N.; Thomas, W.; Sokurenko, E. Type 1 Fimbrial Adhesin Fimh Elicits an Immune Response That Enhances Cell Adhesion of Escherichia Coli. *Infection and Immunity* **2011**, *79*, 3895-3904.

126. Zhou, W.; Zhang, J.; Liu, Y.; Li, X.; Niu, X.; Song, Z.; Min, G.; Wan, Y.; Shi, L.; Feng, S. Characterization of Anti-Adhesive Self-Assembled Monolayer for Nanoimprint Lithography. *Applied Surface Science* **2008**, *255*, 2885-2889.

127. Van Oss, C. J. Acid—Base Interfacial Interactions in Aqueous Media. *Colloids and Surfaces A* **1993**, *78*, 1-49.

128. Chen, J.K.; Ko, F.H.; Hsieh, K.F.; Chou, C.T.; Chang, F.C. Effect of Fluoroalkyl Substituents on the Reactions of Alkylchlorosilanes with Mold Surfaces for Nanoimprint Lithography. *Journal of Vacuum Science and Technology B* **2004**, *22*, 3233-3241.

129. O'Neill, M. E. A Sphere in Contact with a Plane Wall in a Slow Linear Shear Flow. *Chemical Engineering Science* **1968**, *23*, 1293-1298.

130. Castillo, J. M.; Klos, M.; Jacobs, K.; Horsch, M.; Hasse, H. Characterization of Alkylsilane Self-Assembled Monolayers by Molecular Simulation. *Langmuir* **2015**, *31*, 2630-2638.

131. Harimawan, A.; Rajasekar, A.; Ting, Y.-P. Bacteria Attachment to Surfaces – Afm Force Spectroscopy and Physicochemical Analyses. *J. Colloid Interface Sci.* **2011**, *364*, 213-218.

132. Singh, A. V.; Vyas, V.; Patil, R.; Sharma, V.; Scopelliti, P. E.; Bongiorno, G.; Podestà, A.; Lenardi, C.; Gade, W. N.; Milani, P. Quantitative Characterization of the

Influence of the Nanoscale Morphology of Nanostructured Surfaces on Bacterial Adhesion and Biofilm Formation. *PLoS ONE* **2011**, *6*, e25029.

133. Hsu, L. C.; Fang, J.; Borca-Tasciuc, D. A.; Worobo, R. W.; Moraru, C. I. Effect of Micro- and Nanoscale Topography on the Adhesion of Bacterial Cells to Solid Surfaces. *Applied and Environmental Microbiology* **2013**, *79*, 2703-2712.

134. McAllister, E. W.; Carey, L. C.; Brady, P. G.; Heller, R.; Kovacs, S. G. The Role of Polymeric Surface Smoothness of Biliary Stents in Bacterial Adherence, Biofilm Deposition, and Stent Occlusion. *Gastrointest. Endosc.* **1993**, *39*, 422-425.

135. Nilsson, L.; Thomas, W.; Trintchina, E.; Vogel, V.; Sokurenko, E. Catch Bond-Mediated Adhesion without a Shear Threshold: Trimannose Versus Monomannose Interactions with the Fimh Adhesin of *Escherichia Coli*. *Journal of Biological Chemistry* **2006**, *281*, 16656-16663.

136. Xu, C.-P.; Boks, N. P.; de Vries, J.; Kaper, H. J.; Norde, W.; Busscher, H. J.; Van Der Mei, H. C. Staphylococcus Aureus-Fibronectin Interactions with and without Fibronectin-Binding Proteins and Their Role in Adhesion and Desorption. *Applied and Environmental Microbiology* **2008**, *74*, 7522-7528.

137. Whitehead, K. A.; Rogers, D.; Colligon, J.; Wright, C.; Verran, J. Use of the Atomic Force Microscope to Determine the Effect of Substratum Surface Topography on the Ease of Bacterial Removal. *Colloids and Surfaces B* **2006**, *51*, 44-53.

138. Kalasin, S.; Santore, M. M. Engineering Nanoscale Surface Features to Sustain Microparticle Rolling in Flow. *ACS Nano* **2015** *9*, 4706–4716.

139. Hubbe, M. A. Theory of Detachment of Colloidal Particles from Flat Surfaces Exposed to Flow. *Colloids and Surfaces* **1984**, *12*, 151-178.

140. Burdick, G. M.; Berman, N. S.; Beaudoin, S. P. Hydrodynamic Particle Removal from Surfaces. *Thin Solid Films* **2005**, *488*, 116-123.

141. Burdick, G. M.; Berman, N. S.; Beaudoin, S. P. Describing Hydrodynamic Particle Removal from Surfaces Using the Particle Reynolds Number. *Journal of Nanoparticle Research* **2001**, *3*, 455-467.

142. Kucheria, R.; Dasgupta, P.; Sacks, S. H.; Khan, M. S.; Sheerin, N. S. Urinary Tract Infections: New Insights into a Common Problem. *Postgraduate Medical Journal* **2005**, *81*, 83-86.

143. Wiles, T. J.; Kulesus, R. R.; Mulvey, M. A. Origins and Virulence Mechanisms of Uropathogenic *Escherichia Coli*. *Experimental and Molecular Pathology* **2008**, *85*, 11-19.

144. Feng, G.; Cheng, Y.; Wang, S.-Y.; Borca-Tasciuc, D. A.; Worobo, R. W.; Moraru, C. I. Bacterial Attachment and Biofilm Formation on Surfaces Are Reduced by Small-Diameter Nanoscale Pores: How Small Is Small Enough? *NPJ Biofilms and Microbiomes* **2015**, *1*, 15022.

145. Sokurenko, E. V.; Vogel, V.; Thomas, W. E. Catch-Bond Mechanism of Force-Enhanced Adhesion: Counterintuitive, Elusive, But ... Widespread? *Cell Host Microbe* **2008**, *4*, 314-323.

146. Berke, A. P.; Turner, L.; Berg, H. C.; Lauga, E. Hydrodynamic Attraction of Swimming Microorganisms by Surfaces. *Physical Review Letters* **2008**, *101*, 038102.

147. Kostoglou, M.; Karabelas, A. J. Effect of Roughness on Energy of Repulsion between Colloidal Surfaces. *Journal of Colloid and Interface Science* **1995**, *171*, 187-199.

148. Suresh, L.; Walz, J. Y. Effect of Surface Roughness on the Interaction Energy between a Colloidal Sphere and a Flat Plate. *Journal of Colloid and Interface Science* **1996**, *183*, 199-213.

149. Hoek, E. M. V.; Bhattacharjee, S.; Elimelech, M. Effect of Membrane Surface Roughness on Colloid−Membrane Dlvo Interactions. *Langmuir* **2003**, *19*, 4836-4847.

150. Kalasin, S.; Santore, M. M. Hydrodynamic Crossover in Dynamic Microparticle Adhesion on Surfaces of Controlled Nanoscale Heterogeneity. *Langmuir* **2008**, *24*, 4435-4438.

151. Anselme, K.; Davidson, P.; Popa, A. M.; Giazzon, M.; Liley, M.; Ploux, L. The Interaction of Cells and Bacteria with Surfaces Structured at the Nanometre Scale. *Acta Biomaterialia* **2010**, *6*, 3824-3846.

152. Katsikogianni, M.; Missirlis, Y. Concise Review of Mechanisms of Bacterial Adhesion to Biomaterials and of Techniques Used in Estimating Bacteria–Material Interactions. *Eur. Cell Mater* **2004**, *8*, 37-57.

153. Yang, S.; Wen, X.; Zhao, L.; Shi, Y.; Jin, H. Crude Oil Treatment Leads to Shift of Bacterial Communities in Soils from the Deep Active Layer and Upper Permafrost Along the China-Russia Crude Oil Pipeline Route. *PLoS ONE* **2014**, *9*, e96552.

154. Flemming, H.-C.; Meier, M.; Schild, T. Mini-Review: Microbial Problems in Paper Production. *Biofouling* **2013**, *29*, 683-696.

155. Derrien, M.; van Passel, M. W. J.; van de Bovenkamp, J. H. B.; Schipper, R. G.; de Vos, W. M.; Dekker, J. Mucin-Bacterial Interactions in the Human Oral Cavity and Digestive Tract. *Gut Microbes* **2010**, *1*, 254-268.

156. Yildiz, H. M.; Speciner, L.; Ozdemir, C.; Cohen, D. E.; Carrier, R. L. Food-Associated Stimuli Enhance Barrier Properties of Gastrointestinal Mucus. *Biomaterials* **2015**, *54*, 1-8.

157. Jabr, F. Microbial Mules. *Scientific American* **2012**, *306*, 20-20.

158. Martinez, V. A.; Schwarz-Linek, J.; Reufer, M.; Wilson, L. G.; Morozov, A. N.; Poon, W. C. K. Flagellated Bacterial Motility in Polymer Solutions. *Proceedings of the National Academy of Sciences* **2014**, *111*, 17771-17776.

159. Patteson, A. E.; Gopinath, A.; Goulian, M.; Arratia, P. E. Running and Tumbling with E. Coli in Polymeric Solutions. *Scientific Reports* **2015**, *5*, 15761.

160. Chen, G.; Walker, S. L. Role of Solution Chemistry and Ion Valence on the Adhesion Kinetics of Groundwater and Marine Bacteria. *Langmuir* **2007**, *23*, 7162-7169.

161. Ji, Y. W.; Hong, S. H.; Chung, D. Y.; Kim, E. K.; Lee, H. K. Comparison of Surface Roughness and Bacterial Adhesion between Cosmetic Contact Lenses and Conventional Contact Lenses *Journal of the Korean Ophthalmological Society* **2014** *55(5)*, 646-655.

162. Eisenberg, D. A.; Klink, I. M.; Phillips, R. J. Axisymmetric Sedimentation of Spherical Particles in a Viscoelastic Fluid: Sphere–Wall and Sphere–Sphere Interactions. *Journal of Rheology* **2013**, *57*, 857-880.

163. Ardekani, A. M.; Joseph, D. D.; Dunn-Rankin, D.; Rangel, R. H. Particle-Wall Collision in a Viscoelastic Fluid. *Journal of Fluid Mechanics* **2009**, *633*, 475-483.

164. D'Avino, G.; Cicale, G.; Hulsen, M. A.; Greco, F.; Maffettone, P. L. Effects of Confinement on the Motion of a Single Sphere in a Sheared Viscoelastic Liquid. *Journal of Non-Newtonian Fluid Mechanics* **2009**, *157*, 101-107.

165. Despeyroux, A.; Ambari, A. Slow Motion of a Sphere Towards a Plane through Confined Non-Newtonian Fluid. *Journal of Non-Newtonian Fluid Mechanics* **2012**, *167–168*, 38-45.

166. Li, G. J.; Karimi, A.; Ardekani, A. M. Effect of Solid Boundaries on Swimming Dynamics of Microorganisms in a Viscoelastic Fluid. *Rheologica acta* **2014**, *53*, 911-926.

167. Redman, J. A.; Walker, S. L.; Elimelech, M. Bacterial Adhesion and Transport in Porous Media: Role of the Secondary Energy Minimum. *Environmental Science and Technology* **2004**, *38*, 1777-1785.

168. Sharma, S.; Jaimes-Lizcano, Y. A.; McLay, R. B.; Cirino, P. C.; Conrad, J. C. Subnanometric Roughness Affects the Deposition and Mobile Adhesion of Escherichia Coli on Silanized Glass Surfaces. *Langmuir* **2016**, *32*, 5422-5433.

169. Bradford, S. A.; Torkzaban, S.; Walker, S. L. Coupling of Physical and Chemical Mechanisms of Colloid Straining in Saturated Porous Media. *Water Research* **2007**, *41*, 3012-3024.

170. Oliveira, P. D.; Michel, R. C.; McBride, A. J. A.; Moreira, A. S.; Lomba, R. F. T.; Vendruscolo, C. T. Concentration Regimes of Biopolymers Xanthan, Tara, and Clairana, Comparing Dynamic Light Scattering and Distribution of Relaxation Time. *PLoS ONE* **2013**, *8*, e62713.

171. Wyatt, N. B.; Liberatore, M. W. Rheology and Viscosity Scaling of the Polyelectrolyte Xanthan Gum. *Journal of Applied Polymer Science* **2009**, *114*, 4076-4084.

172. Yasuda, K.; Armstrong, R. C.; Cohen, R. E. Shear Flow Properties of Concentrated Solutions of Linear and Star Branched Polystyrenes. *Rheologica Acta* **1981**, *20*, 163-178.

173. Colby, R. H. Structure and Linear Viscoelasticity of Flexible Polymer Solutions: Comparison of Polyelectrolyte and Neutral Polymer Solutions. *Rheologica Acta* **2010**, *49*, 425-442.

174. Kaya, T.; Koser, H. Characterization of Hydrodynamic Surface Interactions of Escherichia Coli Cell Bodies in Shear Flow. *Physical Review Letters* **2009**, *103*, 138103.

175. Li, G.; Tam, L.-K.; Tang, J. X. Amplified Effect of Brownian Motion in Bacterial near-Surface Swimming. *Proceedings of the National Academy of Sciences* **2008**, *105*, 18355-18359.

176. Cisneros, L.; Dombrowski, C.; Goldstein, R. E.; Kessler, J. O. Reversal of Bacterial Locomotion at an Obstacle. *Physical Review E* **2006**, *73*, 030901.

177. Männik, J.; Driessen, R.; Galajda, P.; Keymer, J. E.; Dekker, C. Bacterial Growth and Motility in Sub-Micron Constrictions. *Proceedings of the National Academy of Sciences* **2009**, *106*, 14861-14866.

178. Barnhart, M. M.; Chapman, M. R. Curli Biogenesis and Function. *Annual review of microbiology* **2006**, *60*, 131-147.

179. Jann, K.; Jann, B. Polysaccharide Antigens of Escherichia Coli. *Review of Infectious Diseases* **1987**, *9*, S517-S526.

180. Davis, J. M. R.; Goldberg, J. B. Purification and Visualization of Lipopolysaccharide from Gram-Negative Bacteria by Hot Aqueous-Phenol Extraction. *Journal of Visualized Experiments : JoVE* **2012**, 3916.

181. Beveridge, T. Visualizing Bacterial Cell Walls and Biofilms. *Microbe Magazine*.

182. Jones, J. F.; Holtzer, G. L.; Snyder, C.; Yake, A. M.; Velegol, D. Charge Nonuniformity Light Scattering. *Colloids and Surfaces A: Physicochemical and Engineering Aspects* **2005**, *267*, 79-85.